

Impact Resonance Test Protocol for Bituminous Mixture Property Evaluation

by

Morteza REZAEIZADEH HEROZI

THESIS PRESENTED TO ÉCOLE DE TECHNOLOGIE SUPÉRIEURE
IN PARTIAL FULFILLMENT FOR A MASTER'S DEGREE
WITH THESIS IN CONSTRUCTION ENGINEERING
M.A.Sc.

MONTREAL, MAY 27, 2025

ÉCOLE DE TECHNOLOGIE SUPÉRIEURE
UNIVERSITÉ DU QUÉBEC



Morteza Rezaeizadeh Herozi, 2025



This [Creative Commons](https://creativecommons.org/licenses/by-nc-nd/4.0/) licence allows readers to download this work and share it with others as long as the author is credited. The content of this work can't be modified in any way or used commercially.

BOARD OF EXAMINERS (THESIS M.Sc.A)
THIS THESIS HAS BEEN EVALUATED
BY THE FOLLOWING BOARD OF EXAMINERS

Mr. Jean-Claude Carret, Thesis Supervisor
Department of Construction Engineering at École de technologie supérieure

Mr. Lucas Babadopulos, Thesis Co-supervisor
Departamento de Engenharia Estrutural e Construção Civil (DEECC) at Universidade Federal do Ceará (Brazil)

Mr. Kevin Bilodeau, Thesis Co-supervisor
BauVal Inc., Canada

Mr. Diego Ramirez Cardona, President of the Board of Examiners
Department of Construction Engineering at École de technologie supérieure

Mrs. Yasmina Mahmoudi, Member of the jury
École Nationale des Travaux Publics de l'État at Université de Lyon (France)

Mr. Pejoochan Tavassotti-Kheiry, Member of the jury
Department of Civil and Environmental Engineering at University of Waterloo (Canada)

THIS THESIS WAS PRESENTED AND DEFENDED
IN THE PRESENCE OF A BOARD OF EXAMINERS AND PUBLIC
ON APRIL 16, 2025
AT ÉCOLE DE TECHNOLOGIE SUPÉRIEURE

ACKNOWLEDGMENTS

I would like to convey my heartfelt thanks to my advisor, Professor Jean-Claude Carret, and my co-supervisors Lucas Babadopulos for their support, guidance, and invaluable insights throughout the research process and while writing this thesis. I extend my heartfelt thanks to Mr. Kevin Bilodeau at BauVal Inc. for his dual role as an industrial partner and co-supervisor. His encouragement and constructive feedback have been invaluable in improving the quality of my research. Their mentorship has played a vital role in shaping the direction of my work and advancing my academic endeavors.

I would also like to express my appreciation to the LCMB group for allowing me to participate in an engaging research project in pavement engineering and for the chance to work alongside diverse individuals, students, and organizations.

I am also thankful to technicians Sylvain Bibeau and Francis Bilodeau for their support and insightful suggestions during the lab tests, which were instrumental in guiding the direction of my project.

I would also like to express my sincere gratitude to Bauval Inc. for providing all the specimens for this study, and to Bitumar and les industries mcasphalt ltée for supplying the bitumen. Their support played a key role in enabling this research and ensuring its progress.

Protocole de test par résonance d'impact pour l'évaluation des propriétés des mélanges bitumineux

Morteza REZAEIZADEH HEROZI

RÉSUMÉ

Cette étude vise à évaluer le contrôle de qualité des enrobés bitumineux en examinant le module complexe et l'angle de phase à l'aide de l'essai de résonance par impact (IRT). Garantir la fiabilité du signal enregistré est essentiel pour calculer avec précision le module complexe et l'angle de phase à partir des résultats de l'IRT. De plus, le choix de la géométrie d'éprouvette la plus appropriée est fondamental pour obtenir des propriétés du mélange fiables. Afin de définir les conditions d'essai recommandées, l'étude s'est appuyée sur des méthodes expérimentales, notamment des essais sur des éprouvettes compactées par presse à cisaillement giratoire (PCG) en mode longitudinal pour évaluer la qualité et l'amplitude de la force appliquée. Les résultats ont mis en évidence l'intérêt d'une surface sciée pour éviter les impacts amortis. Une force supérieure à 60 N est également recommandée afin d'atteindre l'amplitude souhaitée et d'éviter les effets d'amortissement. Par ailleurs, l'utilisation d'un système de montage à base de colle améliore l'adhérence et la précision du signal. Pour identifier une géométrie d'éprouvette et des configurations d'essai adaptées aux essais en laboratoire, l'étude a combiné des simulations numériques et des validations expérimentales. Les simulations ont permis de déterminer les géométries et configurations idéales, qui ont ensuite été validées par des essais en laboratoire sur des échantillons fabriqués. L'étude a conclu que les éprouvettes de forme discoïdale sont les plus adaptées à l'IRT en laboratoire, car cette géométrie permet une meilleure distinction entre les fréquences de résonance flexurale et longitudinale, garantissant ainsi des mesures plus précises. L'étude a analysé l'influence de la teneur en vides d'air sur les propriétés du mélange en termes de fréquence de résonance, module complexe et angle de phase. Les résultats montrent que l'augmentation des vides d'air entraîne une diminution de la fréquence de résonance et du module complexe, tandis qu'aucune tendance claire n'a été observée pour l'angle de phase.

Mots-clés: Essai de résonance par impact, mélanges bitumineux, fréquences de résonance, teneur en vides d'air, configurations d'essai

Impact Resonance Test Protocol for Bituminous Mixture Property Evaluation

Morteza REZAEIZADEH HEROZI

ABSTRACT

This study aims to assess the quality control of bituminous mixtures by investigating the complex modulus and phase angle using the impact resonance test (IRT). Ensuring the accuracy of the recorded signal is crucial for reliably calculating the complex modulus and phase angle from IRT data. Additionally, selecting the most appropriate specimen geometry is key to obtaining accurate mixture properties. To establish the recommended test conditions, the study employed experimental methods, which involved testing shear gyratory compacted (SGC) specimens in the longitudinal mode to analyze force quality and amplitude. The investigation recommended a sawn surface condition to avoid damp impacts. A force greater than 60 N is also recommended to achieve the desired amplitude and avoid damp impacts. Additionally, using a glue-based mounting system improves adhesion and enhances signal accuracy. To recommend suitable specimen geometry and test configurations for laboratory use, the study used a combination of numerical methods and experimental validation methods. Numerical simulations were conducted to identify ideal specimen geometries and configurations, and these findings were subsequently validated through laboratory testing on fabricated samples. The investigation concluded that disc-shaped specimens are the most recommended for IRT in laboratory settings, as this geometry allows for well-separated flexural and longitudinal resonance frequencies, resulting in more accurate measurements. The study investigated the impact of air void content on mixture properties, including resonance frequency, complex modulus, and phase angle. The results revealed that as air void content increased, both resonance frequency and complex modulus declined, whereas no definite trend was observed for the phase angle.

Keywords: Impact resonance test, bituminous mixtures, resonance frequencies, air void content, test configurations

TABLE OF CONTENTS

	Page
INTRODUCTION	1
CHAPTER 1 LITERATURE REVIEW	3
1.1 Bituminous Mixtures	3
1.1.1 Composition.....	3
1.1.2 Domain of Behaviour.....	4
1.1.3 Linear Viscoelastic Behaviour.....	5
1.1.3.1 Time-Temperature Superposition Principle.....	6
1.1.3.2 Conventional Complex Modulus Tests.....	7
1.1.4 Quality Control	9
1.1.4.1 Bitumen Content	10
1.1.4.2 Gradation Specifications.....	10
1.1.4.3 Maximum Specific Gravity.....	11
1.1.4.4 Shear Gyrotory Compaction	11
1.2 Mechanical Wave Propagation	12
1.2.1 Ultrasonic Test	13
1.2.2 Impact Resonance Test	14
1.2.2.1 Labratory Procedure and Test Set Up.....	14
1.2.2.2 Frequency Response Function	15
1.2.2.3 Coherence Function	16
1.3 Determination of Bituminous Mixtures Properties.....	17
1.3.1 Analytical Methods.....	17
1.3.1.1 Dynamic Modulus Calculation	18
1.3.1.1.1 ASTM-C215 Method	18
1.3.1.1.2 ASTM-E1876 Method	19
1.3.1.1.3 Whitmoyer Method.....	20
1.3.1.1.4 Martinček Method.....	22
1.3.1.2 Damping Calculation	22
1.3.1.2.1 Half Power Bandwidth Method	23
1.3.1.2.2 Logarithmic Decrement Method.....	24
1.3.2 Numerical Methods.....	24
1.3.2.1 Modal Analysis	25
1.3.2.2 Modeling of Impact Resonance	25
1.3.2.3 Inverse Analysis Method for Material Property Calculation	27
1.4 Evaluation of Bituminous Mixtures Through Impact Resonance Test.....	28
1.4.1 Influence of Aspect Ratio and Air Void on Damping	28
1.4.2 Influence of Rejuvenators and Additives.....	29
1.4.3 Evaluation of Freeze-Thaw Damage	29
1.4.4 Determination of Linear Viscoelastic Properties	30
1.4.5 Comparison of LVE Properties from IRT and Conventional Tests.....	30
CHAPTER 2 PROBLEM DESCRIPTION AND OBJECTIVES	33

2.1	Problem Statement	33
2.2	Research Objectives	34
CHAPTER 3 METHODOLOGY		35
3.1	Overview of Research Project	35
3.2	Materials	37
3.2.1	Experimental Study	37
3.2.2	Numerical Study	39
3.3	Detailed Methodology	40
3.3.1	Investigation of Surface Conditions and Adhesive Types	40
3.3.1.1	Specimens	41
3.3.1.2	Experimental Study Approach	42
3.3.2	Investigation of Optimal Geometries and Test Configurations	45
3.3.2.1	Specimens	46
3.3.2.1.1	Specimens in the Numerical Study	47
3.3.2.1.2	Specimens in the Experimental Study	47
3.3.2.2	Numerical Study Approach	48
3.3.2.3	Experimental Study Approach	50
3.3.3	Analytical Investigation of Air Void Content on Mixture properties	52
3.3.3.1	Specimens	52
3.3.3.2	Experimental Study Approach	54
CHAPTER 4 RESULTS AND ANALYSIS		55
4.1	Analysis of Surface Conditions and Adhesive Types	55
4.1.1	Influence of Surface Conditions on Applied Impact	56
4.1.1.1	Defination of Δt	56
4.1.1.2	Relation of Surface Conditions and Δt	57
4.1.1.3	Identification of Outlier Impacts	59
4.1.1.4	Relation Between Δt and Force	62
4.1.2	Evaluation of Adhesive Types on Accelerometer Measurement	63
4.1.2.1	Defination of Maximum Peak-to-Peak Amplitude	63
4.1.2.2	Relation Between MPPA and Force	64
4.1.2.3	Assessment of Noise Level in MPPA	65
4.1.3	Summary	66
4.2	Influence of Geometries and Test Configuration on FRF Measurement	66
4.2.1	Range of Fundamental Resonance Frequency	66
4.2.2	Freaquency Response Fucnction Analysis	67
4.2.3	Validation of Resonance Frequency Results	72
4.2.4	Errors in Identifying the Fundamental Resonance Frequency	73
4.2.5	Summary	74
4.3	Influence of Air Void Content on Complex Modulus and Phase Angle	75
4.3.1	Relationship with Measured Frequency	76
4.3.2	Relationship with Complex Modulus Value	77
4.3.3	Relationship with Phase Angle	78
CONCLUSION AND RECOMENDATION		81

APPENDIX I	IMPACT RESONANCE TEST PROTOCOL.....	83
APPENDIX II	ESG-10 MATERIAL PROPERTIES	87
APPENDIX III	EG-10 MATERIAL PROPERTIES.....	91
APPENDIX IV	FRF AND CF FOR OBJECTIVE 2	93
APPENDIX V	FRF AND CF FOR OBJECTIVE 3	101
	LIST OF BIBLIOGRAPHICAL REFERENCES.....	119

LIST OF TABLES

		Page
Table 1.1	Gradation of bituminous mixtures in the LC method	11
Table 3.1	Proportions of the aggregates in the ESG-10 mixtures.....	37
Table 3.2	Properties of materials used in the numerical study of objective 2	40
Table 3.3	Specimens properties in objective 1	42
Table 3.4	Surface condition and adhesive mounting base types in objective 1	43
Table 3.5	Characteristics of specimens in the numerical study of objective 2	47
Table 3.6	Specimens properties in the experimental study in the objective 2	48
Table 3.7	Model Types and Mesh Size for Objective 2.....	49
Table 3.8	Summary of mode of testing in objective 2	51
Table 3.9	Specimens properties in the objective 3.....	53
Table 4.1	Summary of the color codes in the objective 1	55
Table 4.2	Summary of the outlier impacts for different surface conditions	61
Table 4.3	Modal analysis results.....	67
Table 4.4	IRT experimental results.....	70
Table 4.5	Overview of numerical and experimental results in objective 2.....	74
Table 4.6	Specimen properties from impact resonance test results	75

LIST OF FIGURES

	Page
Figure 1.1	Mechanical behavior variations of bituminous mixtures.....4
Figure 1.2	Example of master curve; a) complex modulus b) phase angle.....7
Figure 1.3	Mechanical waves; a) Body b) Surface c) Guided.....13
Figure 1.4	Schematic representation of the IRT.....15
Figure 1.5	Longitudinal frequency dispersion with poisson's ratio.....21
Figure 1.6	Damping ratio calculation via half-power bandwidth23
Figure 1.7	Mode of shape; a) Compression b) Flexural c) Torsional25
Figure 1.8	Method of inverse analysis for material property calculation27
Figure 1.9	Comparison of master curves from FRF and C-T testing.....31
Figure 3.1	Impact resonance test: a) Equipments, b) Hammer and acceleromete36
Figure 3.2	Gradations utilized for the ESG-10 mixtures.....38
Figure 3.3	Gradations of the EG-10 mixture.....38
Figure 3.4	Nomenclature of specimens in objective 141
Figure 3.5	Surface conditions and adhesive types used in objective 144
Figure 3.6	Sawing of SGC Specimens: a) Equipment, b) Sawn Surface44
Figure 3.7	Research plan for objective 2.....45
Figure 3.8	Nomenclature of specimens in objective 246
Figure 3.9	Numerical models for objective 2: a) 2D axisymmetric , b) 3D.....50
Figure 3.10	IRT in Objective 2: a) Longitudinal, b) Symmetric and antisymmetric ...51
Figure 3.11	Nomenclature of specimens in objective 353
Figure 4.1	Definition of Δt57
Figure 4.2	Δt vs. surface conditions for ESG-10; a) 23 °C, b) -20 °C58

Figure 4.3	Δt vs. surface conditions at 23 °C for EG-10	58
Figure 4.4	Distribution of Δt values across various specimens and conditions	60
Figure 4.5	Example of outlier impacts; a) Irregular impacts b) Damp impacts	60
Figure 4.6	Δt vs. force; ESG-10; a) 23 °C b) -20 °C, EG-10; c) 23 °C d) -20 °C	62
Figure 4.7	Defination of MPPA	63
Figure 4.8	Force vs. MPPA; a) ESG-10 b) EG-10	64
Figure 4.9	Noise level example using SVD of Hankel Matrix	65
Figure 4.10	Numerical FRF at 23 °C: a) SGC; b) Cylinder; c and d) Disc.....	68
Figure 4.11	Numerical FRF at -20 °C; a) SGC, b) Cylinder, c and d) Disc.....	69
Figure 4.12	Experimental FRF at 23 °C; a) SGC, b) Cylinder, c and d) Disc	71
Figure 4.13	Experimental FRF at -20 °C; a) SGC, b) Cylinder, c and d) Disc.....	72
Figure 4.14	FRF and CF for EG-10-G4-D-200G-05-T at 23 °C.....	73
Figure 4.15	Air void content vs. first resonance frequency; a) 23 °C, b) -20 °C.....	77
Figure 4.16	Air void content vs. complex modulus	78
Figure 4.17	Air void content vs. phase angle	79

LIST OF ABBREVIATIONS AND ACRONYMS

NDT	Non-Destructive Testing
IRT	Impact Resonance Test
QC	Quality Control
SGC	Shear Compacted Specimen
LVE	Linear viscoelastic
FEM	Finite Element Modeling
UT	Ultrasonic Testing
LC	Laboratoire des chaussées
SY	Symmetric
ASY	Antisymmetric
FRF	Frequency Response Function
FFT	Fast Fourier Transformations
CF	Coherence Function
RAP	Reclaimed asphalt pavement
BBR	Bending Beam Rheometer
CI	Confidence Interval
IQR	Interquartile range
SNR	Signal-to-Noise Ratio

LIST OF SYMBOLS

G_{mm}	Maximum Specific Gravity
V_{be}	Volume of Effective Asphalt Binder
V_{ba}	Volume of Absorbed Asphalt Binder
φ	Phase Angle
$ E^* $	Complex Modulus Value
E'	Storage Modulus
f_d	Damped Resonant Frequency
v_r	Longitudinal Wave Velocity
λ	Wavelength
f_{nr}	Undamped Resonant Frequency
L	Specimen Length
ρ	Density
v_0	Phase Velocity
A_N	Amplitude of Noise
A_S	Amplitude of Signal
$S_{xx}(f)$	Auto-Power Spectrum of the Loading Force
$S_{xy}(f)$	Cross-Power Spectrum
$S_{yy}(f)$	Auto Power Spectrum of the Acceleration Response
ω	Angular Frequency
u	Displacement Vector
∇	Gradient Operator

INTRODUCTION

Asphalt materials are essential in constructing flexible pavements, as they must withstand various challenges, including traffic loads, temperature fluctuations, and environmental factors. The performance of asphalt depends on its composition, properties, and the effectiveness of long-term maintenance strategies. Asphalt's durability is crucial for maintaining the reliability of infrastructure. Hence, quality control (QC) plays an important role in maintaining the durability and performance of bituminous mixture. Traditionally, QC focused on volumetric properties, such as aggregate gradation, asphalt binder content, and void ratios. However, the growing adoption of mechanistic design methods and performance-based specifications has shifted the focus toward testing characteristics directly linked to pavement distress, such as cracking resistance and moisture damage susceptibility (Aakif Ishaq & Giustozzi, 2022; Boz, Tavassoti-Kheiry, et al., 2017; Boz & Solaimanian, 2018). This shift has increased the popularity of NDT methods due to their speed, adaptability, and effectiveness when integrated with FEM simulations (DeCarlo et al., 2020; Rashetnia et al., 2022).

Non-Destructive Testing (NDT) methods have emerged as a practical alternative to conventional destructive testing. These methods assess asphalt properties without damaging the material, allowing for the reuse of samples in further analyses. The finite element method (FEM) further enhances this approach by expanding the scope of problem-solving through simulation. FEM allows researchers to reduce the number of experimental tests needed by predicting material behavior under various conditions, thus saving time and resources. This combination of numerical and experimental studies is increasingly favored for its efficiency and cost-effectiveness (J.-C. Carret, Di Benedetto, & Sauzéat, 2018a; Essid et al., 2022; Lu et al., 2021; Wei et al., 2022).

For viscoelastic materials like bituminous mixtures, the complex modulus is a key property of interest. This parameter characterizes the relationship between applied stress and resulting strain and includes the modulus (magnitude) and the phase angle, which represents the delay between stress and strain responses. Traditionally, the complex modulus is measured using sinusoidal loading tests, where cyclic loads are applied to capture stress-strain behavior. These quasi-static methods provide valuable insights into stiffness and damping properties under

slow, steady loading conditions (Ma et al., 2024; Meng et al., 2020; Nemati et al., 2020; Nemati & Dave, 2018).

Dynamic testing methods, such as vibration-based techniques, offer a faster and non-invasive alternative for material characterization. These methods involve applying short disturbances or continuous oscillations to the material and analyzing the resulting vibrations to reveal properties like internal structure, stiffness, and damping behavior. Among these methods, the impact resonance test (IRT) stands out for its efficiency and suitability for rapid evaluations, including field applications (Khademzadeh & Sarkar, 2024; Sadeghi et al., 2024).

The Impact Resonance Test (IRT) uses resonance frequency analysis to provide a quick and cost-effective method for evaluating the mechanical properties of asphalt. This approach simplifies setup and preparation, offers valuable insights into material behavior, and serves as an effective tool for quality control and performance evaluation (Brown et al., 1978; Orosa et al., 2022).

The use of FEM and IRT together provides an efficient and modern approach to testing bituminous mixtures. FEM simulations help predict the performance of these mixtures under different conditions, such as temperature changes and different test configurations, minimizing the need for multiple physical tests. This approach allows for faster and more cost-effective assessment of various bituminous mixtures.

CHAPTER 1

LITERATURE REVIEW

1.1 Bituminous Mixtures

Bituminous mixtures are formed by binding mineral aggregates with bitumen or, historically, tar. While tar was once the primary binder, bitumen has since become the more commonly used material. These mixtures are predominantly employed in road construction but also have applications in industries such as roofing, paint production, and waterproofing. A diverse range of bituminous materials exists, each with unique characteristics. Choosing the right material for a specific purpose requires careful consideration of technical, economic, and environmental aspects (Bustillo Revuelta, 2021).

1.1.1 Composition

Bituminous mixtures are primarily composed of mineral aggregates (approximately 95% of the material) combined with a bituminous binder (around 5%). Bitumen, a hydrocarbon-based substance, is derived as a byproduct during crude oil refining. It serves as a key binding agent in the construction of infrastructure like roads, highways, and airport pavements, ensuring the strength and longevity of paved surfaces. Additionally, bitumen is used in various industrial sectors due to its adhesive and waterproofing properties (Krishnan & Rajagopal, 2005). Bituminous mixtures are composite materials consisting of aggregates and bituminous binders. The aggregates form the structural base, while the binder acts as the adhesive that binds the components. The overall performance of the mixture depends on the interaction between these phases. The stability of the aggregate structure, which is crucial for preventing deformation, is influenced by factors such as the properties of the aggregates, the characteristics of the binder, and the mixing temperature. This stability arises from the interlocking of aggregate particles and the adhesive strength of the binder. The friction between particles, the contact conditions, and the overall stability of the aggregate framework are vital in determining the mixture's mechanical properties and durability (Li et al., 2020).

1.1.2 Domain of Behaviour

A bituminous mixture exhibits a complex, temperature-sensitive behavior where its response to loading is strongly influenced by temperature and loading path, as shown in Figure 1.1. The material's behavior can be categorized into four main regions based on strain amplitude (ϵ) and the number of applied cyclic loadings (N). In the linear elastic region, the mixture shows minimal permanent deformation with recovery after loading. As strain amplitude and cyclic loading increase, it enters the viscoelastic region, where energy dissipation and permanent deformation increase. With further loading, the mixture experiences plastic deformation, marked by irreversible changes in structure. Eventually, extensive loading cycles lead to the fatigue region, where the material's stiffness decreases, and cracks form due to accumulated damage. Each of these behaviors is affected by temperature, material composition, aging, and environmental conditions (Di Benedetto et al., 2007; Olard et al., 2003).

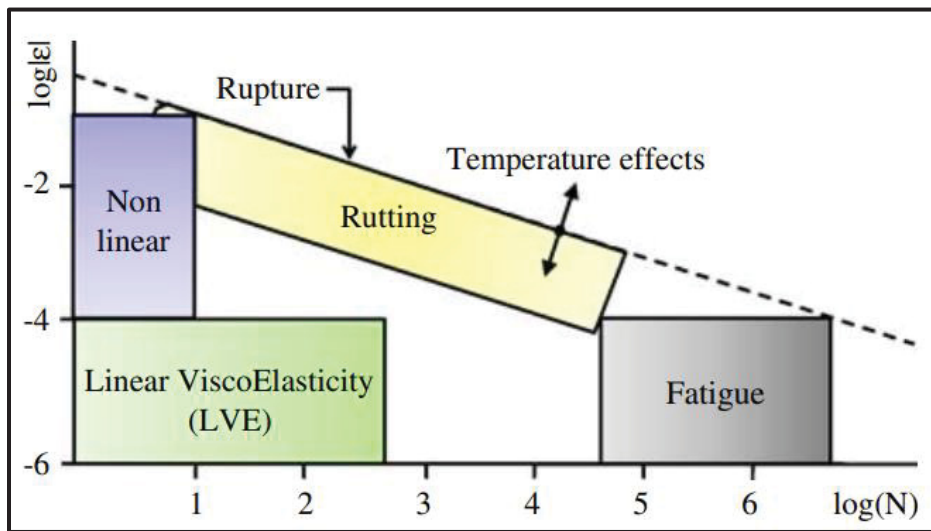


Figure 1.1 Mechanical behavior variations of bituminous mixtures

Taken from Pouget et al., (2010, p.5)

1.1.3 Linear Viscoelastic Behaviour

Linear viscoelastic (LVE) materials are characterized by mechanical behavior that depends on both time and frequency, distinguishing them from purely elastic or viscous materials. Their response to external forces varies based on the type of loading, requiring different analytical approaches. In the time domain, material properties are assessed by monitoring changes in deformation or stress over time under constant stress or strain conditions. In the frequency domain, cyclic loading is used to evaluate how the material stores and dissipates energy, providing insights into its dynamic properties. These methods together offer a comprehensive understanding of material performance under diverse conditions (Di Benedetto, Olard, et al., 2004).

In the time domain, creep and stress relaxation experiments are conducted to study material behavior. During a creep test, a constant load is applied, and the resulting gradual increase in strain is measured, defining the creep function. In a stress relaxation test, the material is held at a fixed strain while the stress is recorded over time, yielding the relaxation function. Due to the complexity of these relationships, mathematical tools like the Laplace-Carson transform are often used to simplify integral equations into algebraic forms. This simplification facilitates the application of the elastic-viscoelastic correspondence principle, which links viscoelastic behavior to classical elasticity. The reciprocal relationship between creep and relaxation functions highlights the connection between material stiffness and energy dissipation (Han et al., 2024).

In the frequency domain, cyclic loading is applied to characterize dynamic material properties, such as the complex modulus and complex Poisson's ratio. When a sinusoidal stress is applied, the resulting strain exhibits a phase difference, defining the complex modulus as the ratio of stress to strain in the frequency spectrum. This modulus consists of two components: the storage modulus, which represents energy storage, and the loss modulus, which quantifies energy dissipation. Similarly, Poisson's ratio in the frequency domain is expressed as a complex quantity, reflecting phase shifts between radial and axial strain. The relationships between the complex modulus, shear modulus, and Poisson's ratio resemble those in classical elasticity. Graphical techniques, such as Cole-Cole and Black diagrams, are often used to

illustrate frequency-dependent properties and assess material behavior under varying temperatures, ensuring consistency through the time-temperature superposition principle (Mazurek & Iwański, 2017; Y. Zhao et al., 2013).

1.1.3.1 Time-Temperature Superposition Principle

For materials exhibiting linear viscoelastic (LVE) behavior, such as bituminous mixtures, the complex modulus is influenced by both temperature and frequency. In the small strain domain where LVE behavior applies, the time-temperature superposition principle (TTSP) can be used, meaning the material behaves in a thermorheologically simple manner. Under these conditions, complex modulus values obtained at different temperatures and frequencies can correspond to one another, reflecting an equivalence between the effects of temperature and frequency. This concept is known as the TTSP. A key outcome of this principle is that a single curve can represent the variation of the complex modulus, either in magnitude or phase, across frequencies when referenced to a specific temperature (T_{ref}) (J.-C. Carret, Pedraza, et al., 2018). Master curves are constructed by horizontally shifting the data obtained at various temperatures along the frequency axis, as illustrated in Figure 1.2a for the complex modulus and Figure 1.2b for the phase angle. Each original frequency is adjusted by multiplying it with a shift factor (a_T), which depends only on the test temperature (T) and the reference temperature (T_{ref}). The adjusted values are known as reduced frequencies. Equation (1.1) defines the relationship between the complex modulus at the original conditions and at the reduced frequency and reference temperature.

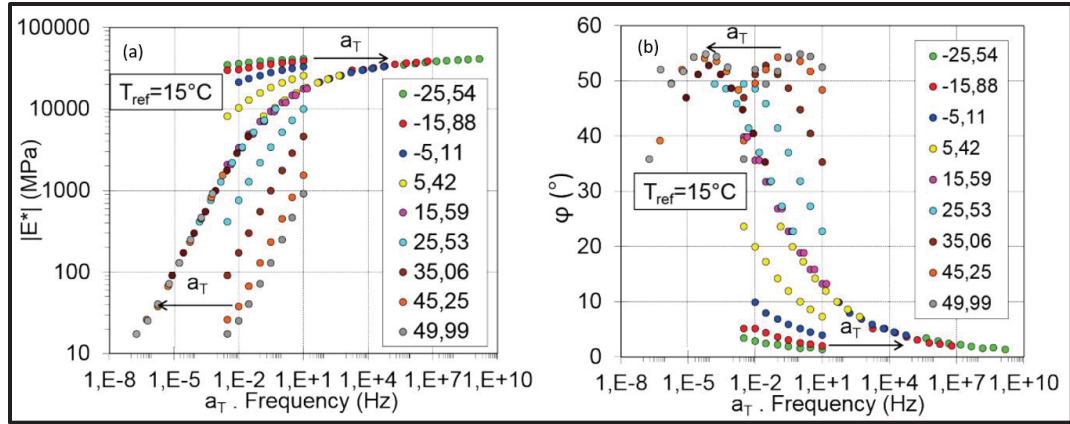


Figure 1.2 Example of master curve; a) complex modulus b) phase angle

Taken from J.-C. Carret, (2019, p. 8)

$$E^*(f, t) = E^*(f \cdot a_T(T), T_{ref}) \quad (1.1)$$

The shift factors are typically modeled as a function of temperature using the Williams-Landel-Ferry (WLF) equation (1.2) (J.-C. Carret, Pedraza, et al., 2018):

$$\log a_T = \frac{-C_1(T - T_{ref})}{C_2 + T - T_{ref}}$$

The WLF equation uses material constants C_1 and C_2 , which change with the reference temperature (T_{ref}), and is valid across the full temperature range tested. This makes it possible to create master curves for any selected reference temperature. The Time-Temperature Superposition Principle (TTSP) is especially useful as it provides the ability to estimate the complex modulus at frequencies and temperatures that are not experimentally achievable (Boussabnia et al., 2023; Di Benedetto et al., 2009).

1.1.3.2 Conventional Complex Modulus Tests

Various testing setups, both homogeneous and non-homogeneous, are utilized to assess the complex modulus and stiffness of bituminous mixtures (Di Benedetto, de La Roche, et al., 2004; Di Benedetto et al., 2001). The complex modulus captures the material's dynamic

response under loading, reflecting both its elastic and viscous characteristics (Phan et al., 2017).

In homogeneous tests, which rely on Saint Venant's principle, the material is assumed to experience a uniform force distribution across its cross-section. This uniformity enables the direct calculation of stress and strain from the applied load and boundary displacement measurements (Jiao et al., 2019). The elastic component of the complex modulus, derived from these tests, indicates the material's stiffness by measuring its resistance to deformation. For example, in a compression test, stiffness is calculated as the ratio of applied stress to resulting strain, with the elastic part of the complex modulus playing a significant role in this relationship (Di Benedetto, de La Roche, et al., 2004; Di Benedetto et al., 2001).

On the other hand, non-homogeneous tests require additional assumptions about the material's rheological behavior to infer internal stresses and strains from boundary data. For instance, in four-point bending tests, the material's resistance to bending is used to determine stiffness. The flexural modulus, closely related to the complex modulus, serves as a critical measure of bending stiffness. Here, stiffness is evaluated by measuring the deflection caused by an applied force, with the flexural modulus offering insights into the material's ability to withstand bending (Babadopulos et al., 2011).

In summary, stiffness is closely tied to the complex modulus across different testing approaches. In homogeneous tests, it is derived from the elastic portion of the complex modulus, whereas in non-homogeneous tests, it is often linked to the flexural modulus in bending situations. These metrics provide valuable insights into the material's resistance to deformation under varying loading conditions (De Oliveira et al., 2022; Di Benedetto et al., 2001). Common test procedures for evaluating the complex modulus and stiffness of bituminous mixtures are compression-tension tests, four-point bending tests, indirect tensile tests. Each of these methods provides critical information about the material's mechanical behavior under a variety of loading and stress states (J.-C. Carret, Di Benedetto, & Sauzéat, 2018b; Poulikakos et al., 2015).

Although conventional mechanical tests provide critical insights into the complex modulus and stiffness of bituminous materials, they have notable limitations. One major drawback is their

reliance on expensive and specialized equipment, such as compression-tension testing systems and four-point bending setups, which require precise calibration, skilled operators, and strictly controlled conditions to ensure accuracy. Additionally, these methods often involve destructive sample preparation, requiring cored or molded specimens, which can be both time-consuming and material-intensive. The high cost and complexity of such techniques make them less practical for routine quality control and large-scale pavement assessments (J.-C. Carret, Di Benedetto, & Sauzéat, 2018b). In contrast, non-destructive testing (NDT) methods have emerged as a promising alternative, allowing for the evaluation of complex modulus and stiffness without altering the material properties. Among these, techniques based on mechanical wave propagation have demonstrated significant potential (Goel & Das, 2008; Mounier et al., 2012).

1.1.4 Quality Control

Quality control for bituminous mixtures involves a series of essential tests to ensure the material meets performance and composition standards (Lachance-Tremblay et al., 2016). The process begins with determining the binder content using solvent extraction, as outlined in LC 26-100. This technique isolates the bitumen from the aggregates, providing critical data about the binder proportion in the mixture (Rezazad Gohari et al., 2023). Next, the particle size distribution of the aggregates is analyzed to confirm it aligns with the required specifications. Proper aggregate gradation is vital for ensuring the mixture's strength, stability, and resistance to deformation under traffic loads (Al-Khateeb et al., 2017). Following the gradation test, the density of the mixture is evaluated to assess its compactness and uniformity. Achieving the correct density is crucial for long-term durability and performance. Finally, compaction testing is conducted to replicate real-world construction conditions. This step evaluates how effectively the mixture can reach the desired density during placement, ensuring it will resist deformation and maintain its structural integrity over time. These procedures collectively ensure that the bituminous mixture performs optimally in terms of strength, stability, and resistance to common issues like rutting and cracking (Bérubé et al., 2023; Imaninasab et al., 2024). Additional test, such as assessing moisture susceptibility, may also be performed

depending on project requirements, further enhancing the reliability and longevity of the pavement (Arambula et al., 2007).

1.1.4.1 Bitumen Content

The bitumen content in bituminous mixtures can be assessed using two methods: the ignition oven method (LC 26-006) and solvent extraction (LC 26-100) (Basueny et al., 2014). The ignition oven method involves heating the mixture in an oven to burn off the bitumen, leaving behind the aggregate, which is then weighed to determine the bitumen content based on the loss in weight. While this method is quick, it may not be as accurate, particularly for mixtures with lower bitumen content. On the other hand, solvent extraction uses solvents like trichloroethylene or n-heptane to dissolve the bitumen, which is then recovered by evaporating the solvent, and the bitumen content is calculated from the weight. Although this technique is more precise, it is slower than the ignition oven method (Basueny et al., 2014). Both methods are commonly employed, with the choice depending on factors like the level of accuracy needed and the available equipment.

1.1.4.2 Gradation Specifications

The Laboratoire des chaussées (LC) mix design method utilizes a graphical approach to aggregate grading in bituminous mixtures, similar to the Superpave system and other established methods. It includes a restricted zone in the gradation curve, ranging from the 315 μm sieve to the 2.5 mm sieve, with key control points set at the 80 μm , 5 mm, and larger sieves. If the gradation curve exceeds this restricted zone, it can lead to difficulties during application and reduced resistance to rutting (Kandhal & Mallick, 2001). However, when aggregates possess high angularity, the restricted zone has less influence on the overall performance of bituminous mixtures. Additionally, gradations that closely follow the maximum density line often result in low voids in the mineral aggregate (VMA), limiting bitumen content and compromising durability. Such mixtures tend to deteriorate quickly and are highly sensitive to

variations in bitumen content. For optimal performance, the gradation should pass through the designated control points and ideally remain below the restricted zone (Al-Khateeb et al., 2017). The LC method also classifies bituminous mixtures based on the nominal maximum aggregate size, following the superpave system as outlined in Table 1.1.

Table 1.1 Gradation of bituminous mixtures in the LC method

Bituminous mixtures type	Nominal maximum size (mm)	Maximum size (mm)
ESG-5, EG-5	5	10
ESG-10, EG-10, EGA-10, etc.	10	14
ESG-14	14	20
GB-20	20	28

1.1.4.3 Maximum Specific Gravity

The maximum specific gravity (G_{mm}) of a bituminous mixture is used to determine the volumetric proportions of its components. It reflects the combined specific gravity of the aggregates and binder with air voids excluded. G_{mm} is crucial for ensuring the correct proportions of materials in the bituminous mixture design. The LC mix design method, based on volumetric principles, includes specifications for the V_{be} , which represents the volume of binder coating the aggregates without being absorbed. To calculate V_{be} , it is necessary to first determine the volume of binder absorbed by the aggregates (V_{ba}), using the G_{mm} value of the bituminous mixture (Bérubé et al., 2023).

1.1.4.4 Shear Gyratory Compaction

The compaction characteristics of an asphalt mixture are assessed using a Shear Gyratory Compactor (SGC), following the LC 26-003 standard, which aligns with ASTM D6925. During the test, the specimen is subjected to a steady pressure of 600 kPa for 200 gyrations, and the variation in air void content (V_a) is monitored. Before testing, the samples are conditioned by heating to 160 °C. The LC mix design criteria require that after 10 gyrations, the air void content must be above 11.0%; after 100 gyrations, it should fall within the range

of 4.0% to 7.0%; and after 200 gyrations, it must remain above 2.0%. To ensure accuracy, at least three SGC tests are performed for each mixture to verify adherence to these standards (Lachance-Tremblay et al., 2016).

1.2 Mechanical Wave Propagation

Mechanical waves in solids are classified into three main types: body waves, surface waves, and guided waves, each serving specific purposes in testing applications. Body waves move through the material's interior and consist of compressional waves (P-waves) and shear waves (S-waves), with their speed determined by the material's rigidity and mass density. Surface waves, like Rayleigh and Love waves, travel along the material's outer layer and are particularly effective for identifying defects close to the surface. Guided waves, such as Lamb waves, are suited for thin structures, where they interact with both surfaces of structure (Hohensinn, 2019; Tsangouri et al., 2019; Zhu et al., 2021). In impact resonance testing (IRT), body waves are predominant, as the resonant frequencies are influenced by the material's internal vibrations, which are shaped by its elastic characteristics and structural dimensions. On the other hand, ultrasonic testing (UT) can employ body waves, surface waves, or guided waves, depending on the material's thickness and the defect's position. The geometry of the specimen, boundary conditions, and experimental setup significantly affect wave propagation, impacting both resonance measurements and the detection of flaws using ultrasonic methods (Hohensinn, 2019; Karoliny Lemos Bezerra et al., 2023; G. Zhao et al., 2019). Figure 1.3 shows the different types of mechanical waves.

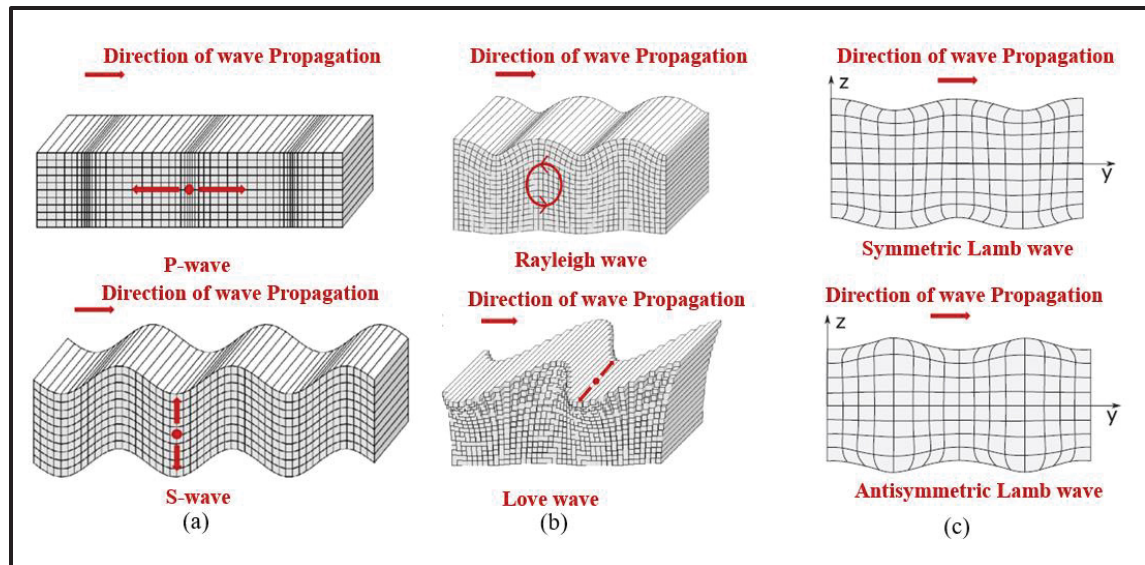


Figure 1.3 Mechanical waves; a) Body b) Surface c) Guided

Taken from Hohensinn, (2019, p. 39)

1.2.1 Ultrasonic Test

Ultrasonic testing (UT) is a versatile and widely used non-destructive testing (NDT) method that employs high-frequency sound waves to evaluate the internal integrity of materials. By sending ultrasonic waves into a material using a transducer, the technique detects flaws such as cracks, voids, or inclusions. When the sound waves encounter a boundary or defect, they are reflected back to the transducer, which also acts as a receiver. The time taken for the waves to return is measured, allowing technicians to determine the location, size, and nature of the flaw. UT is highly sensitive and can detect very small defects, making it a valuable tool for ensuring the safety and reliability of critical components in industries such as aerospace, automotive, oil and gas, and construction (Kou et al., 2021).

One of the key advantages of ultrasonic testing is its ability to inspect thick materials and detect flaws deep within a structure without causing any damage. It is particularly useful for inspecting welds, measuring material thickness, and assessing the integrity of components like pipelines, pressure vessels, and aircraft parts. However, UT does have some limitations. The surface of the material being tested must be smooth and clean to ensure proper coupling of the transducer, and the technique requires skilled operators to accurately interpret the results.

Additionally, materials with coarse grains or complex geometries can pose challenges for ultrasonic inspection (Wolf et al., 2015).

In the context of bituminous mixtures, UT detect internal flaws like voids, cracks, and delaminations, which are critical for assessing the structural integrity of bituminous layers. UT is also used to measure layer thickness, evaluate density and homogeneity, and detect moisture damage or poor bonding between layers (Birgisson et al., 2003; Tigdemir et al., 2004).

1.2.2 Impact Resonance Test

Impact resonance testing (IRT) is a non-destructive dynamic method that measures resonant vibration frequencies. Since all physical systems with mass and stiffness naturally exhibit vibrations when subjected to external forces, these oscillations are key to understanding the behavior of such systems. Vibration analysis plays a significant role in engineering design across various fields, such as civil, aerospace, mechanical, and materials engineering, where it is essential for improving performance and ensuring structural safety. One specific IRT method is based on the ASTM C215 standard, which uses impact and vibration principles to reliably determine the properties of linear elastic isotropic materials (Brown et al., 1978; Orosa et al., 2022).

1.2.2.1 Laboratory Procedure and Test Set Up

Impact resonance test is designed to assess the amplitude (resonant frequency) and the rate of vibration decay (damping), which are then linked to the material's properties. A specimen with unconstrained boundaries is lightly impacted with a rigid tool at a selected point, triggering mechanical vibrations. An accelerometer, connected to a data acquisition system and positioned appropriately for the test mode, measures the resulting vibration waveform from the impact. The recorded vibrations, presented as a transient signal in the time domain, are then converted into electrical signals by the data acquisition system (Boz, Tavassoti-Kheiry, et al., 2017). Figure 1.4 shown the schematic representation of the IRT.

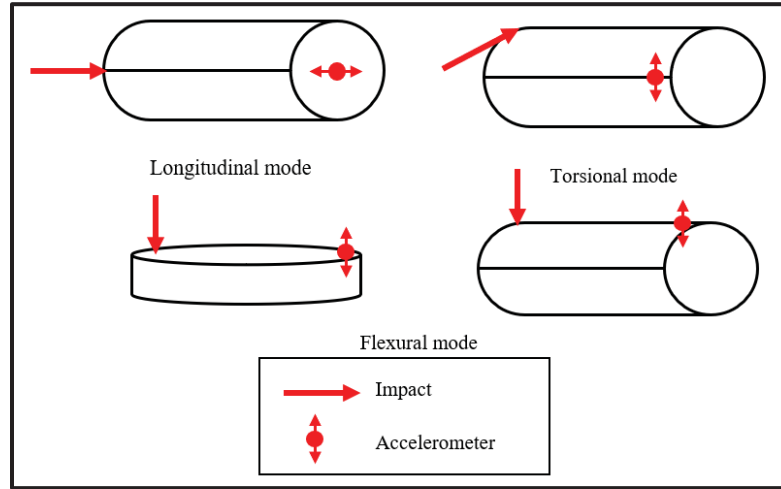


Figure 1.4 Schematic representation of the IRT

Adapted from J. Carret et al., (2020, p. 5)

1.2.2.2 Frequency Response Function

The recorded signals through the impact resonance test are in time domain to convert them in the frequency domain fast fourier transformations (FFT) must be used. The Frequency response functions (FRF) can be determined using equation (1.3) (J. Carret et al., 2020). Frequency response functions represent the relationship between output signals (such as acceleration or displacement) and input signals (like force) within the frequency domain.

These functions are depicted as complex numbers, encompassing both amplitude and phase; however, this analysis emphasizes amplitude for material characterization. A notable benefit of FRFs is that their amplitude is independent of the input, which allows for direct comparisons of material responses across different temperatures to identify variations in properties.

$$FRF(f) = \frac{\overline{S_{xy}(f)}}{\overline{S_{xx}(f)}} \quad (1.3)$$

The Frequency Response Function (FRF), is defined using the cross-power spectrum $S_{xy}(f)$ and the input auto power spectrum $S_{xx}(f)$ as following equations (1.4) and (1.5):

$$S_{xy}(f) = X^*(f) \cdot Y(f) \quad (1.4)$$

$$S_{xx}(f) = X^*(f) \cdot X(f) \quad (1.5)$$

In this context, X denotes the input in the frequency domain, X^* is its complex part, and Y represents the output. While FRFs are expressed as complex numbers that include both amplitude and phase, this analysis prioritizes amplitude for material characterization, making the phase information irrelevant for this thesis.

A key advantage of utilizing FRFs is that their amplitude does not depend on the input, facilitating a direct evaluation of material responses. This characteristic allows for easy comparisons at various temperatures, simplifying the process of identifying changes in material properties.

1.2.2.3 Coherence Function

The coherence function (CF) is an essential metric that assesses the correlation between input and output signals at each frequency. A coherence value of one signifies that the output is entirely dictated by the input, whereas lower values indicate the presence of noise interference. This function is computed using the cross-power spectrum, the input auto power spectrum, and the output auto power spectrum. The coherence function can be determined using equation (1.6).

$$CF(f) = \frac{\overline{S_{xy}^2}}{\overline{S_{xx}} \overline{S_{yy}}} \quad (1.6)$$

In this context, $CF(f)$ indicates the coherence function, while $S_{xy}(f)$ and $S_{xx}(f)$ correspond to the cross-power spectrum and the input auto power spectrum, respectively, as outlined in equations (1.2) and (1.3). Additionally, S_{yy} denotes the output auto power spectrum, which can be calculated using equation (1.7).

$$S_{yy}(f) = Y^*(f) \cdot Y(f) \quad (1.7)$$

In this case, Y refers to the output in the frequency domain, and Y^* represents its complex part. The IRT can be conducted in three vibration modes: longitudinal, flexural, and torsional. (J. Carret et al., 2020).

1.3 Determination of Bituminous Mixtures Properties

The resonance frequency of bituminous materials is strongly linked to their mechanical properties, including stiffness and dynamic modulus. These materials display both elastic and viscous characteristics, with their resonance behavior being affected by factors such as temperature, loading conditions, and composition (Boz & Solaimanian, 2018; J.-C. Carret, Di Benedetto, & Sauzéat, 2018b). As temperatures decrease, bituminous materials become more rigid, causing an increase in resonance frequencies. On the other hand, at elevated temperatures, their viscosity rises, leading to a reduction in resonance frequencies (Boz & Solaimanian, 2018; J.-C. Carret, Di Benedetto, & Sauzeat, 2018).

1.3.1 Analytical Methods

Analytical methods are utilized to evaluate the dynamic behavior of a bituminous mixture by initially subjecting the specimen to dynamic excitation via an impact resonance test. This excitation generates a time-domain response, which is recorded to observe how the mixture behaves under dynamic loading conditions. The time-domain signal is subsequently processed using Fast Fourier Transform (FFT), converting it into the frequency domain and revealing the frequency components of the specimen's response. Peaks in the frequency spectrum correspond to the natural frequencies, offering insight into the material's resonant characteristics. These identified natural frequencies allow for the calculation of the dynamic modulus of the mixture, which measures the stiffness of the material under dynamic forces. Additionally, damping characteristics are extracted from the time-domain data, providing information on the material's energy dissipation during vibration (J.-C. Carret, Di Benedetto,

& Sauzéat, 2018b; Gudmarsson et al., 2014). This analytical method offers a detailed understanding of the dynamic performance of the bituminous mixture, enabling predictions of its behavior in real-world scenarios and under various environmental conditions, which is vital for informing the design and maintenance of durable pavements.

1.3.1.1 Dynamic Modulus Calculation

The dynamic modulus is a fundamental parameter for assessing the viscoelastic behavior of bituminous mixtures under repeated loading. It quantifies the material's stiffness and deformation resistance by correlating the applied cyclic stress with the resulting strain. Given that bituminous mixtures exhibit both elastic and viscous characteristics, the dynamic modulus is a complex value comprising a storage modulus, which reflects the recoverable elastic response, and a loss modulus, which represents energy dissipation (Gudmarsson et al., 2015a). In this dissertation, the methods for determining the dynamic modulus using the first resonance frequency are explained.

1.3.1.1.1 ASTM-C215 Method

ASTM C215-02 outlines an approach for calculating the dynamic modulus of elasticity by assessing the fundamental longitudinal, transverse or torsional resonance frequencies of materials. This method is particularly suitable for elastic materials like concrete, for which the standard was specifically designed, as it does not account for damping. The dynamic modulus can be determined by applying equation (1.8) for the fundamental longitudinal frequency and equation (1.9) for the fundamental transverse frequency.

$$E = DM(n')^2 \quad (1.8)$$

Where D is $5.093 (L/d^2)$ in $N.s^2(kg.m^2)$; L and d are the length diameter of specimen, respectively, M is the mass in kg and n' is the fundamental longitudinal frequency in Hz.

$$E = CMn^2 \quad (1.9)$$

Where C is $1.6067 (L^3T/d^4 \text{ in } N.s^2(kg.m^2))$; L and d are the length diameter of specimen in m, respectively, T is correction factor, M is the mass in kg and n is the fundamental transverse frequency in Hz.

ASTM C215-02 is highly effective for identifying shifts in the dynamic modulus of elasticity resulting from exposure to weathering or other deteriorating conditions, as well as observing how the dynamic elastic modulus evolves as concrete cures. The dynamic modulus measured using this approach is typically greater than the static modulus determined by ASTM C469/C469M, with the extent of the difference influenced by the concrete's strength. Additionally, outcomes can vary depending on factors such as the specimen's moisture levels, production methods, dimensions, geometry, and the type of vibration applied. For precise and valid comparisons, it is essential to evaluate specimens with consistent characteristics and testing conditions.

1.3.1.1.2 ASTM-E1876 Method

ASTM E1876 is a method for determining the dynamic elastic modulus and shear modulus of various materials, such as ceramics, metals, and composites. This method uses the resonance frequencies of a specimen, particularly slender bars with circular cross-sections, and analyzes these frequencies to derive their elastic characteristics. The dynamic elastic modulus can be calculated using equation (1.10), which utilizes the fundamental longitudinal resonant frequency.

$$E = 16 m f_1^2 \frac{L}{\pi D^2 K} \quad (1.10)$$

Where, m represents the mass of the sample, f_1 is the fundamental longitudinal frequency, L is the length of the sample, D is the diameter of the sample, K is a correction factor for the fundamental longitudinal mode.

1.3.1.1.3 Whitmoyer Method

Since the impact resonance test (IRT) involves high strain rates and brief impact durations, the dynamic elastic modulus can be derived using one-dimensional stress wave propagation theory specifically for the longitudinal mode of vibration (Boz & Solaimanian, 2018; Whitmoyer & Kim, 1994). Research indicates that most investigations aimed at determining the dynamic modulus of asphalt concrete from the IR test have utilized this theory. The IR test has demonstrated considerable accuracy, often aligning well with moduli obtained through conventional dynamic modulus tests. This section outlines the process for calculating the dynamic complex modulus of asphalt concrete using one-dimensional stress wave propagation theory.

Once the longitudinal damped resonant frequency (f_d) and damping ratio (ξ) are established from the IRT, the undamped longitudinal resonant frequency (f_{nr}) is calculated using equation (1.11).

$$f_{nr} = \frac{f_d}{\sqrt{1-\xi^2}} \quad (1.11)$$

The wavelength (λ) is determined using equation (1.12), with $n = 1$ and L as the specimen length.

$$\lambda = \frac{2L}{n} \quad (1.12)$$

The longitudinal wave velocity (v_r) is then calculated with equation (1.13). For specimens with similar length and diameter, dispersion occurs, and as can be seen from Figure 1.5 Bancroft's study provides correction factors based on the aspect ratio and Poisson's ratio.

$$v_r = \lambda f_{nr} \quad (1.13)$$

The wave velocity v_r is refined to the phase velocity v_0 for an infinitely long rod, based on the ratio of diameter to wavelength at a particular Poisson's ratio.

The elastic modulus of asphalt specimens can ultimately be calculated using equation (1.14), where ρ represents density.

$$E' = v_0^2 \rho \quad (1.14)$$

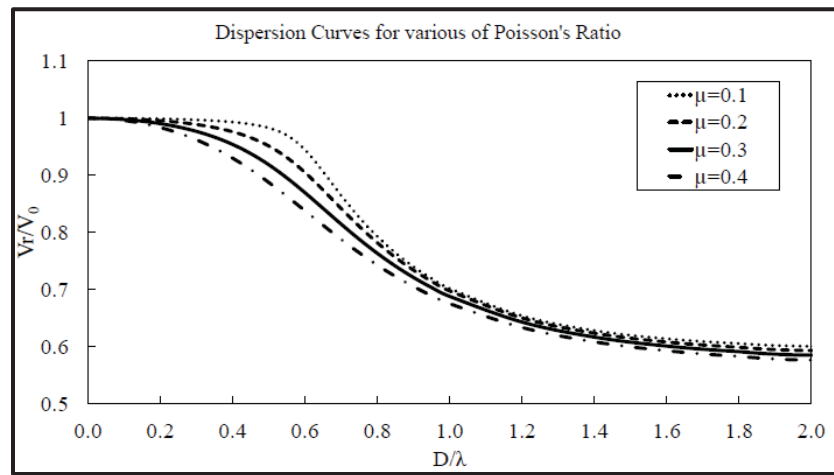


Figure 1.5 Longitudinal frequency dispersion with poisson's ratio

Taken from Boz, (2016, p. 37)

Given the viscoelastic nature of bituminous mixtures, the magnitude of complex modulus of asphalt specimens can be calculated using the equation (1.15).

$$|E^*| = \frac{E'}{\cos \varphi} \quad (1.15)$$

Where φ represents the phase angle, which can be calculated using equation (1.16).

$$\varphi = \tan^{-1} 2\xi \quad (1.16)$$

1.3.1.1.4 Martinček Method

This method is specifically used to calculate the elastic modulus of disc-shaped geometries, which requires testing in both symmetric and antisymmetric modes. The analytical equation (Equation 1.17) proposed by (Martinček, 1965) is applicable only to the symmetric mode for determining the elastic modulus. The antisymmetric mode is necessary for determining μ . Additionally, the damping ratio is calculated using the half-bandwidth method.

$$E' = \frac{48 \pi^2 f_{nrs} R^4 \rho (1-\nu^2)}{\mu^2 h^2} \quad (1.17)$$

Here, E' is the elastic modulus, f_{nrs} and f_{nra} are the first natural resonance frequencies in the symmetric and antisymmetric flexural modes, respectively. The specimen's radius and thickness are R and h , density is defined by ρ , and Poisson's ratio (ν) and factor μ are determined from h/R and $\frac{f_{nrs}}{f_{nra}}$.

1.3.1.2 Damping Calculation

Damping (ξ) refers to the gradual reduction in vibration amplitude due to energy being lost as a result of resistive forces within the system. This decrease is commonly measured by the damping ratio, which is particularly significant for bituminous mixture since it is associated with the phase angle, a key measure of the material's viscoelastic characteristics. The damping ratio can be determined by analyzing either the system's time domain or frequency domain response (Boz & Solaimanian, 2018). In this dissertation, the half power bandwidth method and logarithmic decrement method are explained.

1.3.1.2.1 Half Power Bandwidth Method

The half power bandwidth method is the most widely used technique for calculating the damping ratio from impact resonance tests in asphalt concrete applications. This method relies on frequency domain data to assess the level of damping. Time domain data is converted into frequency domain data through fast Fourier transform (FFT) analysis. After this transformation, the damping ratio is determined by taking the width of the resonance peak at the half power bandwidth points and dividing it by twice the resonant frequency, as shown in equation (1.18). The half power bandwidth points correspond to an amplitude of 0.707 times the maximum amplitude on a linear scale, or an amplitude that is 3 dB lower than the maximum amplitude on a logarithmic scale (Boz & Solaimanian, 2018).

$$\xi = \frac{f_2 - f_1}{2f_d} \quad (1.18)$$

where f_2 and f_1 are the half-power points corresponding to an amplitude that is 3 dB lower than the maximum amplitude f_d as shown in Figure 1.6.

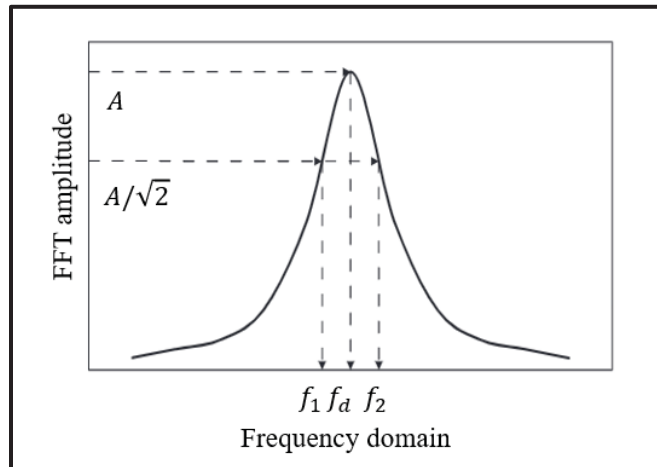


Figure 1.6 Damping ratio calculation via half-power bandwidth

Taken from Boz & Solaimanian, (2018, p. 4)

1.3.1.2.2 Logarithmic Decrement Method

The properties of damping can be analyzed from vibration data using techniques like the logarithmic decrement or exponential decay rate. The logarithmic decrement method is described through the equation (1.19).

$$\xi = \frac{1}{\sqrt{1 + \left(\frac{2\pi}{\delta}\right)^2}} \quad (1.19)$$

where ξ represents the damping ratio, δ and is the logarithmic decrement, which is calculated from the ratio of successive peaks in the vibration signal. This equation provides a direct relationship between the logarithmic decrement and the damping ratio, enabling the estimation of damping characteristics from measured vibration data (Tweten et al., 2014).

1.3.2 Numerical Methods

Numerical methods offer an effective research strategy by facilitating simulations that reduce dependence on extensive physical testing. Consequently, researchers employ computational models to examine different scenarios, optimize experimental designs, and refine testing methods before conducting experimental studies (Essid et al., 2022). This approach speeds up the research process, conserves materials, and lowers associated costs. As a result, numerical methods have become essential in research, especially in inverse analysis. These techniques help determine material properties, adjust model parameters, and enhance the understanding of experimental results. Specifically, inverse analysis employs numerical simulations and optimization techniques to estimate material properties from experimental data (J. Carret et al., 2020). For the aspect of impact resonance test numerical methods can be use to determine the range of resonance frequency using modal analysis and modeling the impact resonance test set ups.

1.3.2.1 Modal Analysis

Modal analysis is a technique utilized to investigate the dynamic behavior of structures and mechanical systems by determining their natural frequencies and mode shapes. Natural frequencies are specific frequencies at which a system oscillates in the absence of external forces, each linked to a unique mode shape. These natural frequencies can correspond to different types of modes, including compression, flexural, and torsional modes. Mode shapes represent the deformed configurations of a structure at these natural frequencies, illustrating how the structure vibrates under excitation. Figure 1.7 shows the three first different modes of vibration. This analysis is critical for understanding the vibrational characteristics of various systems, ensuring structural integrity and performance under dynamic conditions (Krack, 2015; Saxena & Patel, 2023).

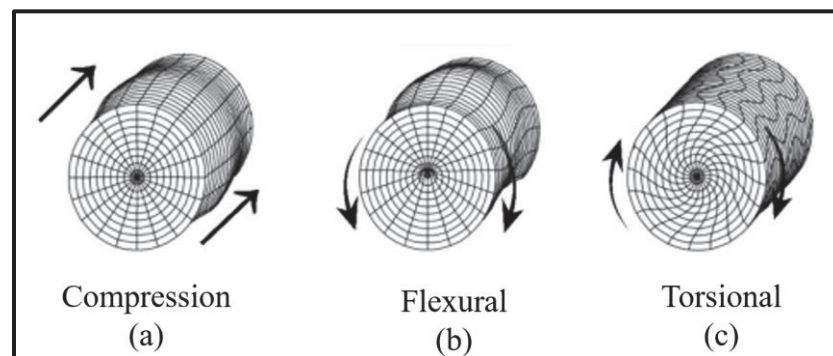


Figure 1.7 Mode of shape; a) Compression b) Flexural c) Torsional

Taken from Yassine & Mustapha, (2024, p.7)

1.3.2.2 Modeling of Impact Resonance

To model the Impact Resonance Test (IRT) accurately, a frequency-domain approach is essential, as it directly aligns with the test's primary output: the frequency response function (FRF). To achieve this, the software computed the FRFs for each specimen under a unit load applied at the impact points used in laboratory testing, with free boundary conditions. This was done by solving the 2D or 3D equations of motion across a frequency range from 100 Hz to

20,000 Hz, with increments of 10 Hz. The 3D form of the equation of motion is provided in equation (1.20). The FRF characterizes a material's response across various frequencies, highlighting resonance peaks that reveal important modal characteristics. Modeling within the frequency domain improves the simulation's alignment with experimental results, making it easier to identify key resonance frequencies that are crucial for evaluating materials like asphalt. This approach is particularly useful, as frequency response data provide valuable insights into the material's structural quality and durability (J.-C. Carret, Di Benedetto, & Sauzeat, 2018; Gudmarsson et al., 2015b).

$$\rho\omega^2u - \nabla \cdot \sigma = F_p e^{i\phi} \quad (1.20)$$

In this context, ω denotes the angular frequency, ρ is the material density, and u represents the displacement vector. The gradient operator is indicated by ∇ and i is the imaginary unit, defined by $i^2 = -1$. The Cauchy stress vector is given as σ . A unit load is specified as F_p , while the phase of the cyclic load is denoted by ϕ .

In this model, the material can be represented as viscoelastic, with its modulus being dependent on temperature but independent of frequency. This behavior can be implemented in the computational software using equation (1.21).

$$E^*(T) = |E_T^*| \cdot e^{(i\phi)} = |E_T^*| \cdot \cos(\phi_T) + i \cdot |E_T^*| \cdot \sin(\phi_T) \quad (1.21)$$

Where E_T^* represents the stiffness of the material at a given temperature. The term $|E_T^*|$ denotes the modulus magnitude, which indicates the material's rigidity. The ϕ_T denotes the phase angle, describing the phase difference between applied stress and the resulting strain, which helps differentiate between the material's elastic (recoverable) and viscous (irrecoverable) responses. Specifically, the real part, $\cos(\phi_T)$, represents the elastic behavior, while the imaginary part, $\sin(\phi_T)$, reflects the viscous behavior. The imaginary unit (i) distinguishes these two components, with the real part linked to the material's energy storage

capability and the imaginary part connected to energy dissipation due to viscous mechanisms. This mathematical model captures the dynamic behavior of the material, illustrating how it stores and dissipates energy during cyclic loading.

1.3.2.3 Inverse Analysis Method for Material Property Calculation

Back analysis techniques are widely employed in evaluating bituminous mixtures to determine material properties (J. Carret et al., 2020; J.-C. Carret, Di Benedetto, & Sauzeat, 2018). The proposed hybrid back analysis method centers on identifying the fundamental resonance frequency at different temperatures and vibration modes. The process begins by extracting the primary resonance frequency for each mode (longitudinal, flexural, and torsional) using finite element modeling (FEM). The frequency bandwidth is also determined through the half-power bandwidth technique. The frequencies from the longitudinal and flexural modes are input into the 2S2P1D model to compute the complex modulus and Poisson's ratio, while the torsional mode frequency is used to derive the complex shear modulus (Boz & Solaimanian, 2018; Olard & Di Benedetto, 2003). The phase angle is calculated using an equation introduced by Clough and Penzien (J.-C. Carret, Di Benedetto, & Sauzeat, 2018). Figure 1.8 shows the inverse analysis method that can be employed to calculate material properties using the first resonance frequency.

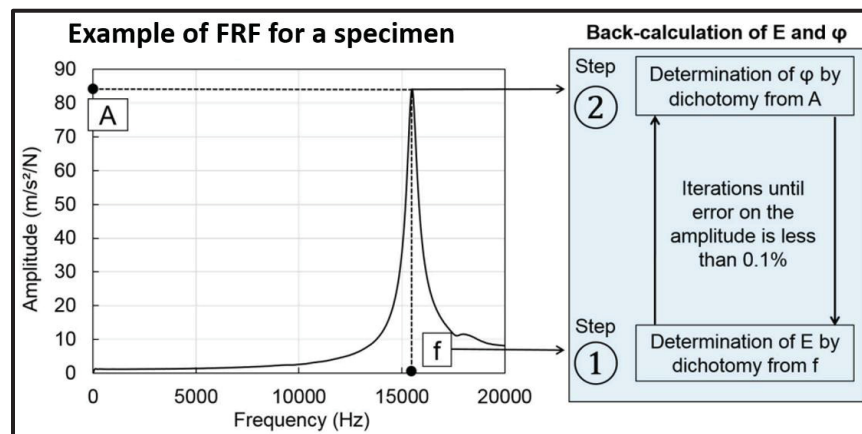


Figure 1.8 Method of inverse analysis for material property calculation

Taken from J.-C. Carret, Di Benedetto, & Sauzéat, (2018, p. 10)

1.4 Evaluation of Bituminous Mixtures Through Impact Resonance Test

Impact resonance test (IRT) is an effective tool for analyzing bituminous mixtures by examining how factors like specimen size and air void content affect resonance frequencies. Initially, it can assess the influence of these basic variables on resonance behavior, providing insights into the material's mechanical properties. Expanding the research could enable IRT to evaluate the performance of bituminous mixtures under varying specimen geometries, temperature changes, and compaction conditions. (Boz & Solaimanian, 2018; Karoliny Lemos Bezerra et al., 2023). This approach would enable a deeper understanding of the performance and quality control of bituminous materials, offering a non-destructive and efficient method for evaluating their suitability in engineering applications.

1.4.1 Influence of Aspect Ratio and Air Void on Damping

The characteristics of asphalt, particularly its stiffness, are related to the resonance frequencies measured through the Impact Resonance Test (IRT). Lower air void content and reduced temperatures are associated with higher frequencies and reduced damping, indicating greater material stiffness (Boz & Solaimanian, 2018; Karoliny Lemos Bezerra et al., 2023). Specimen dimensions are another critical factor, with height exerting a more pronounced influence on the results than diameter. The height-to-diameter ratio, or aspect ratio, defines the point at which frequency remains unchanged. Larger diameter specimens tend to have smaller threshold aspect ratios. Evaluations conducted on specimens with different air void levels, sizes, and aspect ratios across a temperature range of 3–35 °C demonstrate that the wave path, influenced by the specimen's height, is a dominant factor in both longitudinal and torsional modes. These results emphasize the combined effect of asphalt properties and specimen geometry on the accuracy of IRT findings (Boz & Solaimanian, 2014).

1.4.2 Influence of Rejuvenators and Additives

The impact resonance test (IRT) emerges as a promising technique for evaluating the low-temperature behavior of asphalt binders and mixtures, particularly those incorporating reclaimed asphalt pavement (RAP) and rejuvenators (Boz & Solaimanian, 2018; Karoliny Lemos Bezerra et al., 2023). This method effectively captures essential properties, such as the mix modulus and phase angle, and exhibits a strong relationship with traditional rheological tests, including the bending beam rheometer (BBR). Such correlations demonstrate its ability to reliably characterize binder stiffness and relaxation behavior. A notable advantage of IRT is its ability to bypass the binder extraction and recovery process, making it a more efficient option for optimizing rejuvenator content and assessing binder performance. By providing accurate insights into the effects of rejuvenators on reducing stiffness and improving flexibility in RAP mixes, IRT offers a streamlined and practical solution for material evaluation. Its use supports environmentally responsible practices by enabling the reuse of RAP materials while ensuring pavement durability and performance at low temperatures (Boz & Solaimanian, 2018).

1.4.3 Evaluation of Freeze-Thaw Damage

Non-destructive testing (NDT) has become a valuable tool for evaluating freeze-thaw damage in bituminous mixtures, with key parameters like natural frequency, damping ratio, and Rayleigh wave velocity serving as crucial indicators of material deterioration during freeze-thaw cycles. These properties, including dynamic modulus, damping ratio, and Rayleigh wave velocity, are highly sensitive to freeze-thaw damage, as they change frequently with the material's expansion and contraction. In particular, impact resonance testing (IRT) has proven to be a fast and effective method for detecting these real-time changes without inflicting any damage on the pavement (Yadav et al., 2021; M. Zhang et al., 2019). Specimen thickness and impact position were found to significantly influence the sensitivity and repeatability of dynamic modulus measurements, with thicker specimens and those impacted at the edge being more effective in detecting freeze-thaw degradation (L. Zhang et al., 2016).

1.4.4 Determination of Linear Viscoelastic Properties

Complex modulus and stiffness can be assessed using the impact resonance test. The complex modulus reflects a material's capacity to withstand deformation under dynamic loading, providing critical insights into its viscoelastic behavior. Stiffness, derived from the complex modulus, is an important parameter in pavement engineering, as it directly impacts the structural performance and durability of roadways. In mechanistic-empirical (M-E) pavement design methodologies, accurate stiffness data is essential for predicting pavement responses to traffic loads and environmental conditions, such as fatigue cracking and rutting. This information enables engineers to optimize pavement designs and enhance the lifespan of infrastructure (J.-C. Carret, Di Benedetto, & Sauzéat, 2018b).

1.4.5 Comparison of LVE Properties from IRT and Conventional Tests

The complex modulus values obtained from Impact Resonance Tests (IRT) and conventional methods, such as compression-tension (C-T) tests, can be compared through the use of a master curve. This curve, created by applying time-temperature superposition principle (TTSP) to C-T test data, depicts the complex modulus as a function of reduced frequency at a reference temperature (J.-C. Carret, Pedraza, et al., 2018; Gudmarsson et al., 2015b). IRT measures the dynamic modulus at the specimen's fundamental resonance frequency, which can be mapped onto the master curve either directly, if the test temperature aligns with the reference temperature, or indirectly, by utilizing shift factors such as those from the Williams-Landel-Ferry (WLF) (J. Carret et al., 2020). When both tests are performed within the linear viscoelastic range, the dynamic modulus obtained from IRT is expected to correlate with the complex modulus at the corresponding frequency. Furthermore, IRT can estimate the phase angle through damping calculations using methods like the half-bandwidth technique (Boz & Solaimanian, 2018). As a result, the complex modulus values derived from IRT and conventional tests are comparable.

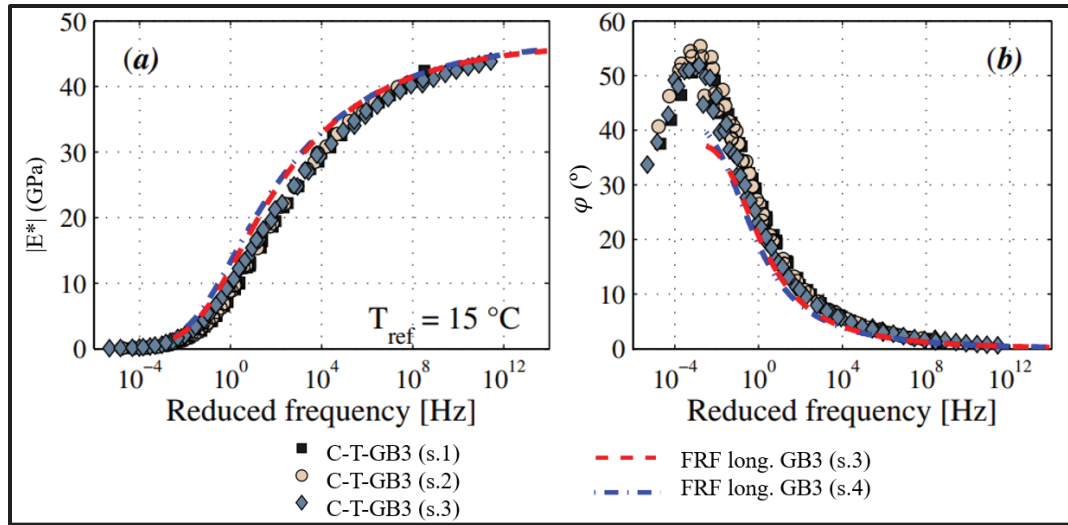


Figure 1.9 Comparison of master curves from FRF and C-T testing

Taken from Gudmarsson et al., (2015a, p. 8)

As an example, Figure 1.9 shows the master curves of the complex modulus and phase angle for the bituminous mixture GB3, obtained through both frequency response function (FRF) optimization of the longitudinal vibration mode and compression-tension (C-T) testing. The FRF-derived curves are presented for two specimens (GB3 s.3 and s.4), while the C-T data cover three individual specimens (s.1, s.2, s.3). The close agreement between the FRF curves, despite differences in specimen dimensions, highlights the reliability of the testing method. Additionally, the C-T tests produced consistent and repeatable complex modulus values across specimens. Notably, the FRF method, which operates under low strain, yielded higher complex modulus values at lower frequencies compared to the C-T testing, but this difference narrowed as frequency increased, indicating reduced strain-level sensitivity at higher stiffness levels (Gudmarsson et al., 2015a).

CHAPTER 2

PROBLEM DESCRIPTION AND OBJECTIVES

2.1 Problem Statement

Quality control (QC) of bituminous mixtures is essential for ensuring the long-term performance of pavements. Conventional QC primarily involves volumetric assessments, including aggregate gradation, bitumen content, and air void content. However, with the advancement of mechanistic-based design and control methodologies, there is an increasing shift toward performance-based specifications. One such parameter is the complex modulus, which characterizes the viscoelastic behavior of bituminous mixtures. It quantifies the ratio of stress to strain magnitudes, representing the material's stiffness, while also accounting for the phase lag between stress and strain responses, described by the phase angle.

Traditional approaches for determining the complex modulus of bituminous mixtures include compression-tension tests, four-point bending tests, and indirect tensile tests. While these methods are widely utilized for evaluating material properties such as stiffness, viscoelastic behavior, and durability, they come with certain drawbacks, including high costs, time-consuming procedures, and the need for destructive testing.

As an alternative, non-destructive testing (NDT) techniques provide a more efficient, rapid, and non-invasive means of material characterization while preserving specimen integrity. Among these methods, the impact resonance test (IRT) has gained significant interest within the research and engineering communities due to its ability to assess material behavior by analyzing resonance frequencies, which are directly linked to mechanical properties at a given temperature.

However, despite the advantages of IRT, many existing studies have primarily concentrated on specific specimen geometries or fixed test configurations, often overlooking a thorough assessment of test setup parameters. Crucial aspects such as surface preparation, adhesive type, and impact conditions are frequently disregarded, even though they can have a substantial impact on test accuracy and reproducibility. This gap in research limits the ability to evaluate

how variations in the test setup affect the reliability of IRT results and the selection of an optimal specimen geometry for accurate modulus determination.

To enhance the effectiveness and applicability of IRT, a more comprehensive investigation into these overlooked factors is necessary. Refining the test setup and identifying the most suitable specimen geometries will contribute to improving result consistency, optimizing testing procedures, and expanding the use of IRT for bituminous mixture characterization.

2.2 Research Objectives

The primary aim of this dissertation is to explore the potential of impact resonance test (IRT) for quality control of bituminous materials by assessing its effectiveness in evaluating key material properties, such as complex modulus and phase angle. The research focuses on confirming the feasibility of IRT and establishing its reliability for quality control, providing essential data and insights for future use. Although the long-term objective is to fully incorporate IRT into routine quality control practices for more efficient, non-destructive testing of bituminous mixtures, this study serves as an initial step toward achieving that goal. To accomplish this, the following specific objectives will be explored:

1. Investigate the influence of the test setup, including the surface conditions of the specimens and the type of adhesive mounting base, on the quality of IRT recorded signals.
2. Recommend the optimal geometries and test configurations for bituminous mixtures for measuring the fundamental resonance frequency through a combination of numerical analysis and IRT experimentation.
3. Evaluate the relationship between the air void content and the properties of bituminous mixtures for the recommended test setup and geometry.

CHAPTER 3

METHODOLOGY

3.1 Overview of Research Project

The research project is divided into two approaches: experimental and numerical studies. Both methods were applied at 23 °C and -20 °C. In the experimental study, to test the specimens at -20 °C, the specimens were placed in a climatic chamber for almost a day and then tested the next day within one minute of removal. The selection of 23 °C was made because it matched the ambient temperature, avoiding the need to stabilize specimen temperatures with a thermal chamber. Conversely, -20 °C was selected as materials exhibit more elastic behavior at lower temperatures, making it easier to measure the fundamental resonance frequency.

Three geometries were examined: shear gyratory compacted (SGC) specimens with a height-to-diameter (H/D) named aspect ratio between 0.74 and 0.86, cylindrical specimens with an H/D of 1.51, and disc-shaped specimens with an H/D ranging from 0.30 to 0.40. In both experimental and numerical studies of the impact resonance test (IRT), the longitudinal vibration mode was investigated for SGC and cylindrical specimens, while both symmetric and antisymmetric vibration modes were assessed for disc specimens.

In the experimental study, which was part of all three research objectives, an impact hammer equipped with a load cell (PCB model 086E80) was used to manually apply loads to the specimens. The resulting vibrations were recorded using an accelerometer (PCB model M353B15). The accelerometer screwed in to a mounting base and attached to the specimens using adhesive. The impact hammer and accelerometer were connected to a signal conditioner (PCB model 482C), which transmitted the signals to a data acquisition device (NI DAQ USB-6341). The signals were recorded on a computer using a custom Python-based application. Figure 3.1 shows the devices that were used in experimental study.

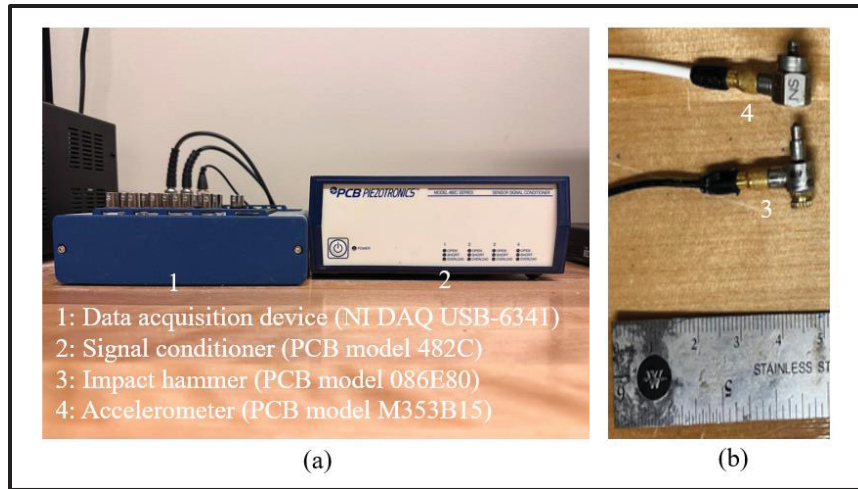


Figure 3.1 Impact resonance test: a) Equipments, b) Hammer and accelerometer

Each test was conducted with a sampling rate of 250,000 samples per second over a duration of 0.009 seconds. No signal post-processing techniques, such as windowing or zero-padding, were applied. To ensure repeatability, each specimen subjected to five impacts. The recorded time-domain signals were converted to the frequency domain using fast fourier transform (FFT). Frequency response functions (FRFs) were calculated according to equation (1.3), including an averaged FRF. To evaluate test reliability, the coherence function (CF) was computed following equation (1.6). CF values range from 0 to 1, where values above 0.9 indicate strong correlation, suggesting minimal noise and high measurement accuracy, whereas values below 0.8 suggest increased noise, non-linearity, or potential issues with the measurement system (J. Carret et al., 2020; J.-C. Carret, Di Benedetto, & Sauzéat, 2018b; J.-C. Carret, Pedraza, et al., 2018; Gudmarsson et al., 2012).

For the numerical study, finite element simulations were conducted using advanced computational modeling software. A three-dimensional (3D) model was used for modal analysis to determine the first resonance frequency range and for simulating the IRT in the antisymmetric mode (for disc specimens only). For all other IRT simulations, a two-dimensional (2D) axisymmetric model was employed. Mesh sizes and types were selected based on prior research that included mesh convergence analyses (J. Carret et al., 2020; J.-C. Carret, Di Benedetto, & Sauzéat, 2018b).

3.2 Materials

3.2.1 Experimental Study

Two types of bituminous mixtures were examined in the experimental studies of this dissertation. The first group mixture was ESG-10, a conventional surface HMA in Québec, with a nominal maximum aggregate size of 10 mm. Three different gradations (G1, G2, and G3) were evaluated by varying the proportions of crushed sand (CS) and manufactured crushed sand (MCS). Both CS and MCS have a maximum sieve size of 5 mm, with a notable difference in the sieve sizes of 630 μm and smaller. Approximately 12% of crushed sand passes through the 80 μm sieve, while only 4% of manufactured crushed sand passes. The cumulative proportions of these two aggregates were kept constant at 56% across the three gradations. These three gradations were developed to produce mixtures: one that met the LC method standards (from gradation 1), one that fell below the requirements (from gradation 2), and one that exceeded them (from gradation 3). Table 3.1 outlines the proportions of the different aggregates in G1, G2, and G3, while Figure 3.2 illustrates the three gradations. In this study, the binder used was PG64H-28, with a content of 5.44%.

Table 3.1 Proportions of the aggregates in the ESG-10 mixtures

Gradation	Percentage of each aggregate type					
	Crushed sand (CS) (0-5 mm)	Manufactured crushed sand (MCS) (0-5 mm)	Crushed stone (2,5-10 mm)	Crushed stone (5-10 mm)	Steel slag (5-10 mm)	Filler (0-80 μm)
G1	42%	14%	10%	10,50%	22,50%	1%
G2	26%	30%	10%	10,50%	22,50%	1%
G3	52%	4%	10%	10,50%	22,50%	1%

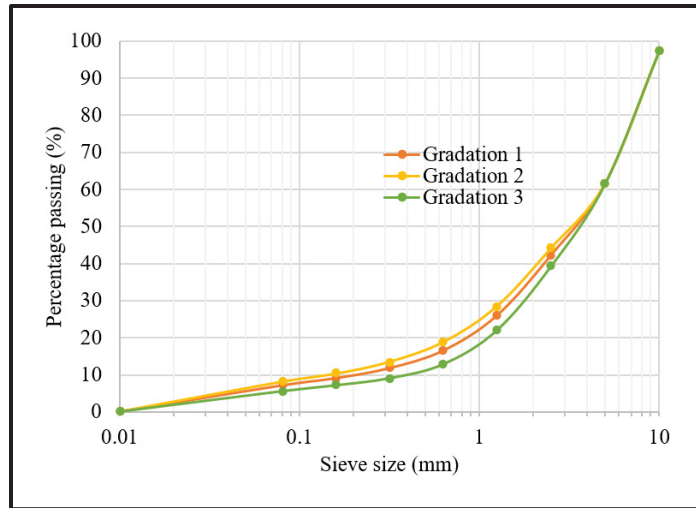


Figure 3.2 Gradations utilized for the ESG-10 mixtures

The second group was EG-10, which is a commonly used surface HMA in Québec, also featuring a nominal maximum aggregate size of 10 mm. The binder for this mixture was also PG64E-28. Notably, due to the manufacturing process, the EG-10 mixtures were produced with four slightly different binder contents and gradations. The binder content range utilized in this mixture was 5.18 ± 0.13 . Figure 3.3 presents the average gradation (G4) of the design mixtures.

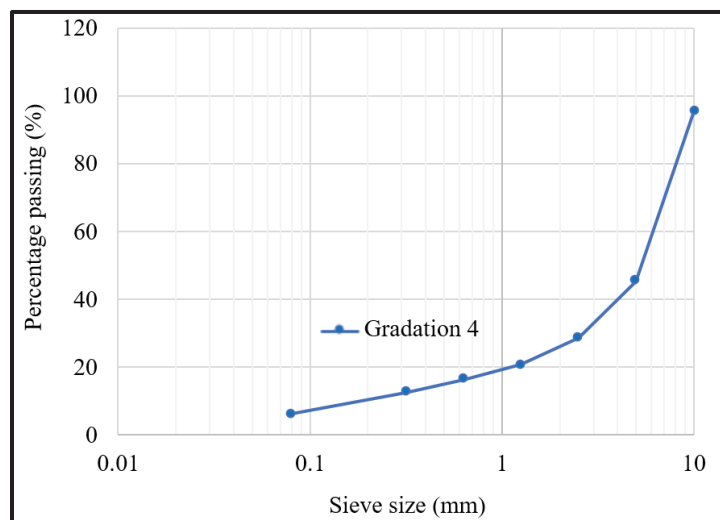


Figure 3.3 Gradations of the EG-10 mixture

It is important to note that BauVal Inc. supplied all the materials for this study. Some specimens were produced at an asphalt plant (EG-10), while others were fabricated in the laboratory (ESG-10 with three gradations). The material properties of these mixtures can be found in Appendix II and III for ESG-10 and EG-10, respectively.

3.2.2 Numerical Study

The complex modulus depends on both temperature and frequency (J.-C. Carret, Pedraza, et al., 2018); however, the aim of this study is to investigate the properties of the bituminous mixture within the range of fundamental resonance frequencies obtained through modal analysis. Therefore, in modeling the impact resonance test, the material properties were treated as temperature-dependent only. Using modulus values specifically at the resonance frequency provided a more straightforward representation of the material's response, avoiding the need to incorporate the full frequency-dependent viscoelastic behavior. This approach also aligns with how experimental results are interpreted, where the modulus is estimated from the resonance peak rather than across a broad frequency range.

In the numerical study (Objective 2), the material properties were thus assumed to exhibit viscoelastic behavior dependent on temperature but independent of frequency. Table 3.2 summarizes the material characteristics used in the numerical models. These values were selected based on dynamic modulus measurements of similar materials, provided by the specimen supplier through cyclic compression-tension tests. Due to the significant difference in loading frequencies between the two tests (approximately 5–10 kHz for IRT versus 0.01–10 Hz for cyclic tests), the dynamic modulus values used as inputs for the IRT numerical model correspond to much lower testing temperatures in the cyclic tests. Additionally, several studies in the literature have shown that the dynamic modulus values of similar asphalt materials determined using IRT at room temperature are close to 20,000 MPa (Boz & Solaimanian, 2018; Karoliny Lemos Bezerra et al., 2023). However, these values serve only as approximate representations of the actual properties of the specimens used in the experimental campaign. Additionally, equation (1.21) defines the formula for incorporating the material behavior in the computational software, where the complex modulus depends only on temperature and not on

frequency. While more advanced frequency-dependent models could provide additional insights, this simplified method was sufficient and fully justified within the scope of a study focused on resonance behavior alone.

Table 3.2 Properties of materials used in the numerical study of objective 2

Materials Properties	Density (kg/m^3)	ν	-20 °C		23 °C	
			$ E_T^* $ (MPa)	$\varphi_T(^{\circ})$	$ E_T^* $ (MPa)	$\varphi_T(^{\circ})$
			30,000	1	20,000	15

3.3 Detailed Methodology

3.3.1 Investigation of Surface Conditions and Adhesive Types

In an impact resonance test, a well-executed single impact with adequate amplitude is essential for effectively exciting a structure's natural frequencies while ensuring accurate data interpretation. A well-controlled impact properly engages the intended resonance modes, minimizing the risk of incomplete or misleading results. Additionally, a sufficiently strong impact improves the signal-to-noise ratio (SNR), making the response more distinguishable from background interference and enhancing the clarity of frequency-domain transformations. Since time-domain data is typically converted into the frequency domain using techniques like the fast fourier transform (FFT), a well-defined impact produces a sharp and distinct frequency spectrum, facilitating the accurate identification of natural frequencies and damping properties (J.-C. Carret, Pedraza, et al., 2018). By accurately managing the variables that affect impact and amplitude, the test ensures the generation of consistent, reproducible, and precise data, which is important for evaluating the dynamic properties of materials.

3.3.1.1 Specimens

The ESG-10 mixture was compacted with two different numbers of gyrations: 80 and 200. For each mixture, one specimen was compacted with 200 gyrations, while three specimens were compacted with 80 gyrations. On the other hand, all EG-10 specimens were compacted with 200 gyrations. Figure 3.4 shows the nomenclature for the specimens in Objective 1, and Table 3.3 summarizes their properties. As illustrated in Figure 3.4, the nomenclature for the specimens is divided into five parts: the first part indicates the mixture type, which can be ESG-10 or EG-10. The second part refers to the gradation, which ranges from G1 to G4, with G1 to G3 corresponding to ESG-10 and G4 being exclusive to EG-10. The third part represents the geometry of the specimens, which are all shear gyratory compacted (SGC) specimens for both mixtures. The fourth part pertains to the gyration rate. The fifth part represents the specimen ID, with ESG-10 specimens compacted with 80 gyrations numbered from 01 to 03, while EG-10 specimens, all compacted with 200 gyrations, are numbered from 01 to 08. Additionally, as shown in Table 3.3, there are two surface conditions: the original surface, which refers to the shear gyratory compacted specimens after compaction without any surface preparation, and the sawn surface condition, which refers to specimens which the surface smoothed using a saw machine.

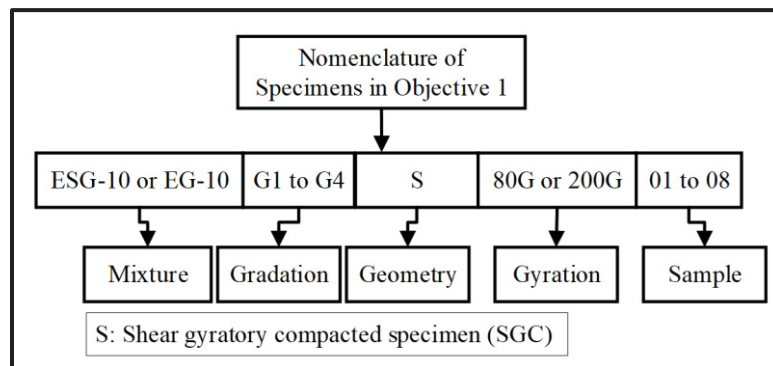


Figure 3.4 Nomenclature of specimens in objective 1

Table 3.3 Specimens properties in objective 1

Mixture	Specime's ID	Original surface		Sawn surface	
		H/D (mm)	Mass of specimen in air (g)	H/D (mm)	Mass of specimen in air (g)
	ESG-10-G3-S-80G-02	128/151	5129	122/151	4984
	ESG-10-G3-S-80G-03	128/151	5127	122/151	4882
EG-10	EG-10-G4-S-200G-01	120/151	5119	116/150	4996
	EG-10-G4-S-200G-02	122/149	5112	116/150	4959
	EG-10-G4-S-200G-03	120/149	5117	115/150	4949
	EG-10-G4-S-200G-04	120/150	5115	115/150	4967
	EG-10-G4-S-200G-05	121/150	5074	115/150	4929
	EG-10-G4-S-200G-06	121/150	5136	116/150	4980
	EG-10-G4-S-200G-07	121/150	5121	116/149	4986
	EG-10-G4-S-200G-08	122/150	5119	117/150	4965

3.3.1.2 Experimental Study Approach

Objective 1 aimed to evaluate the factors affecting the quality of time-domain measurement. Two key factors were analyzed: (1) the surface condition of shear gyratory compacted (SGC) specimens at the hammer impact location and (2) the type of adhesive mounting base used to attach the accelerometer to the specimen surface. To examine these factors, the study was conducted in two phases. Phase 1 involved testing ESG-10 and EG-10 SGC specimens at 23 °C in their original post-compaction surface condition (Figure 3.5a). Two different adhesive mounting bases were used: wax for ESG-10 (Figure 3.5b) and paraffin for EG-10 (Figure 3.5c). Since the results at 23 °C showed minimal differences, only ESG-10 specimens were further tested at -20 °C. Hence, the ESG-10 specimens were placed in a climatic chamber for 24 hours. At -20 °C, a thin ice film might form on the surface of the specimens, preventing the wax from attaching effectively to the mounting base. Therefore, to ensure a stable attachment during testing, a rubber band was used to reinforce the waxed mounting base (Figure 3.5d). Phase 2

involved modifying the surface of both ESG-10 and EG-10 specimens by sawing both sides in the laboratory (Figure 3.6). Water was used during the sawing process to cool the material and reduce dust. Afterward, the specimens were allowed to dry naturally to ensure accurate testing conditions, as excess moisture could influence the resonance frequencies. This drying process helped minimize any potential impact on the material's behavior during the test. Additionally, a thin aluminum sticker was applied to the impact area of EG-10 specimens to assess the effect of surface smoothness on hammer force measurements in the time domain (Figure 3.5e). At 23 °C, the mounting base for ESG-10 was glued, while paraffin was used for EG-10. The specimens were then conditioned in a climatic chamber at -20 °C for 24 hours before testing. For ESG-10 specimens, the mounting base was glued previously at 23 °C. For EG-10, the paraffin behaved similarly to wax at -20 °C, so a rubber band was used to ensure a stable connection between the accelerometer and the specimen.

Table 3.4 presents the investigated surface conditions and adhesive mounting base types for objective 1. As shown in Tables 3.4, the specimen surface conditions are categorized into "original," which refers to the surface after compaction without any preparation, and "sawn" which refers to the surface smoothed using a saw machine. The specimens were initially tested using IRT with the original surface, and then the surface was smoothed with a saw machine, as shown in Figure 3.6a.

Table 3.4 Surface condition and adhesive mounting base types in objective 1

Geometry	Vibration modes	Research phase	Temperature	Surface Conditions	Mixture	Adhesive mounting base types
SGC (S)	Longitudinal	1	23 °C	Original	ESG-10	Wax
					EG-10	Paraffin
			-20 °C	Original	ESG-10	Wax+ rubber band
		2	23 °C	Sawn	ESG-10	Glue
				Sawn+ aluminum sticker	EG-10	Paraffin
			-20 °C	Sawn	ESG-10	Glue
				Sawn+ aluminum sticker	EG-10	Paraffin+ rubber band

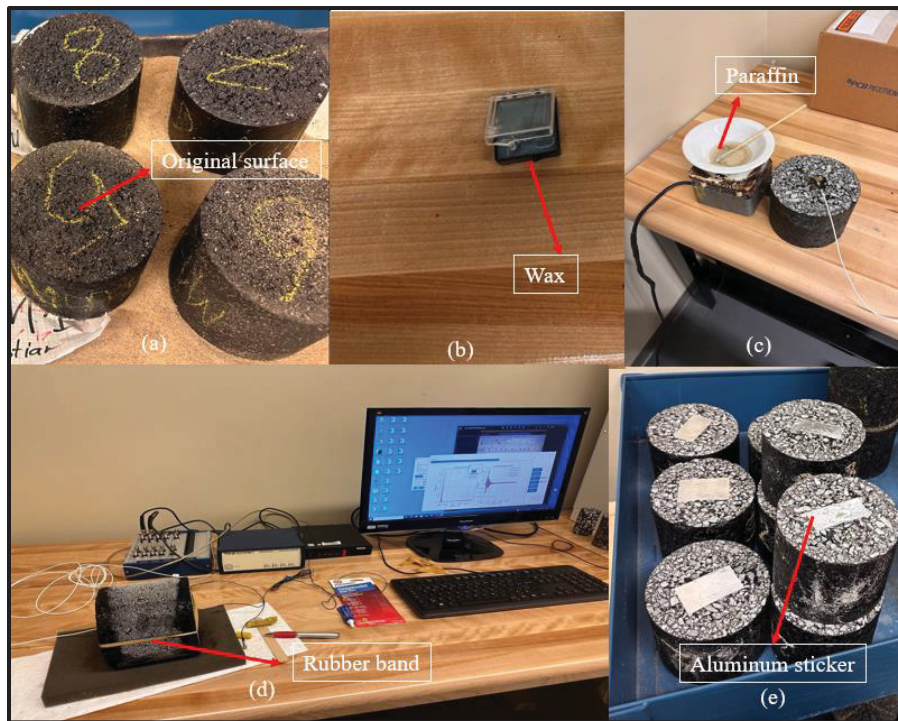


Figure 3.5 Surface conditions and adhesive types used in objective 1

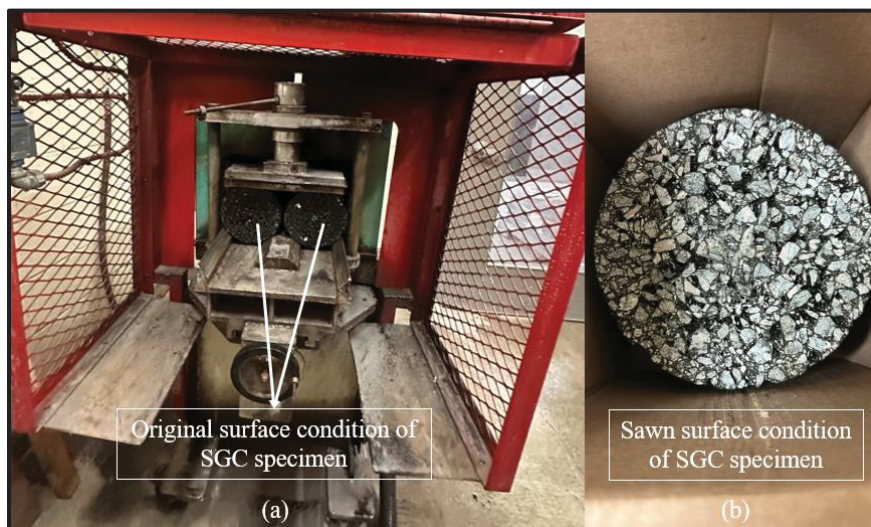


Figure 3.6 Sawing of SGC Specimens: a) Equipment, b) Sawn Surface

3.3.2 Investigation of Optimal Geometries and Test Configurations

The investigation of optimal geometries and test configurations for FRF measurement is crucial for accurate resonance frequency determination. The geometry of the specimen, especially the height-to-diameter (H/D), known as the aspect ratio, influences the natural frequencies and mode shapes by affecting the distribution of stiffness and mass. Once the ideal geometry is established, the choice of test configuration (whether longitudinal, symmetric, or antisymmetric) plays a significant role in how energy is applied to the specimen and which vibrational modes are excited. These configurations directly impact the excitation of modes and the precision of resonance frequency measurements (J. Carret et al., 2020). Overall, selecting both the geometry and test configuration carefully ensures reliable and precise resonance frequency measurements, which are important for evaluating the dynamic behavior of materials. Therefore, this aspect is addressed through the research methodology outlined in objective 2, as illustrated in Figure 3.7.

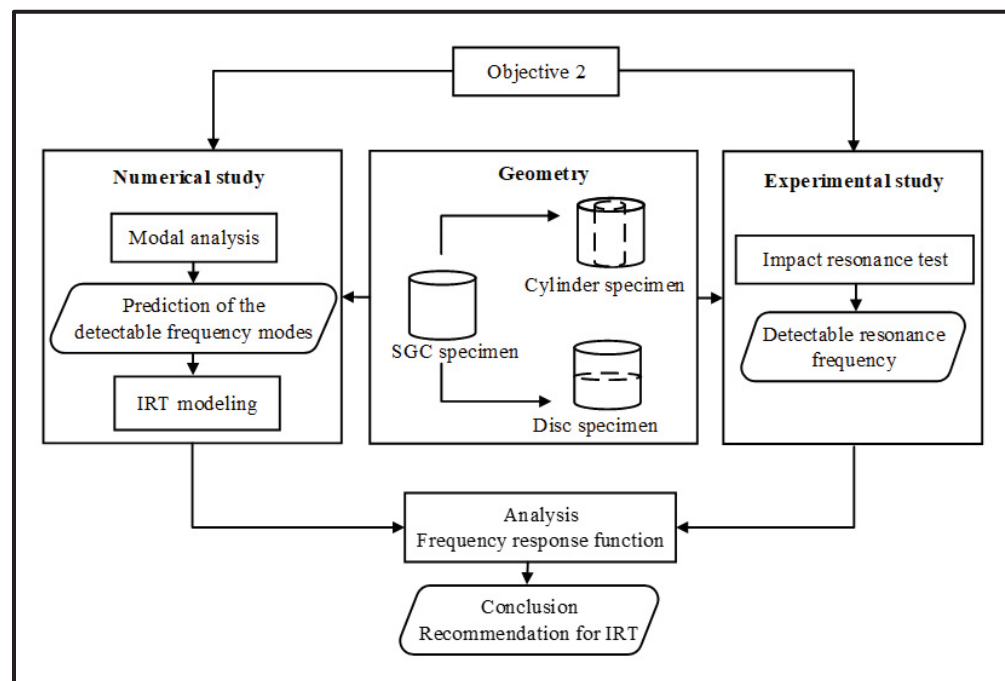


Figure 3.7 Research plan for objective 2

3.3.2.1 Specimens

The nomenclature for the specimens used in this study is illustrated in Figure 3.8. As shown in the Figure 3.8, in the numerical study, the specimen nomenclature consists of two components: the first denotes the geometry type, while the second specifies the specimen number. In contrast, the nomenclature for experimental specimens is structured into five components for all specimens, except for disc specimens, which include a sixth component. The first component represents the mixture type, designated as EG-10 for all specimens. The second indicates the gradation, which was G4 for all cases. The third specifies the geometry type, which included SGC, cylinder, or disc geometries. The fourth component corresponds to the gyration, consistently labeled as 200 G. The fifth component identifies the specimen ID, with specimens 03, 04, 05, and 08 being randomly selected from Objective 1. For disc specimens, the sixth component also indicates whether the specimen was related to the top or bottom of the SGC specimen.

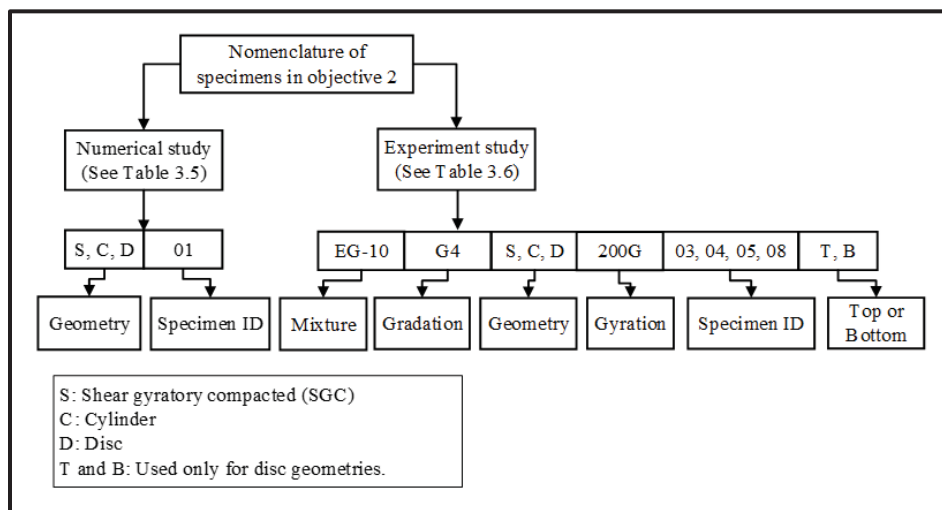


Figure 3.8 Nomenclature of specimens in objective 2

3.3.2.1.1 Specimens in the Numerical Study

In the numerical study of objective 2, the reference geometry was a cylinder with a height of 120 mm and a diameter of 150 mm, which corresponds to the geometry of SGC specimens. The second geometry considered was cylinders with the same height as the SGC specimens but with diameters of 60 mm and 75 mm, representing specimens that could be cored from an SGC specimen in the laboratory. The third geometry consisted of discs with the same diameter as the SGC specimens, but with heights of 60 mm and 40 mm, which could be obtained by sawing an SGC specimen in the laboratory. Tables 3.5 provide detailed characteristics of each specimen.

Table 3.5 Characteristics of specimens in the numerical study of objective 2

Geometry	Specimen ID	H/D (mm)
SGC (S)	S-01	120/15
Cylinder (C)	C-01	120/60
	C-02	120/75
Disc (D)	D-01	60/150
	D-02	40/150

3.3.2.1.2 Specimens in the Experimental Study

For the experimental study of Objective 2, four SGC specimens were randomly selected from those investigated in Objective 1. These specimens had sawn surfaces, and glue was used as the adhesive mounting base to enhance adhesion between the specimens and the accelerometer, thereby improving the quality of the measured signal. After testing the SGC specimens at 23 °C and -20 °C, two were cored to create cylindrical specimens (water was used during core drilling to cool the material and reduce dust, afterward, the specimens were dried naturally to prevent moisture-related effects on resonance frequency and material behavior), while the other two were cut with a saw to produce disc-shaped specimens. Table 3.6 presents the detailed characteristics of each specimen.

Bottom of Form

Table 3.6 Specimens properties in the experimental study in the objective 2

Mixture Types	Specime's ID	Sawn surface	
		H/D (mm)	Mass of specimen in air (g)
EG-10	EG-10-G4-S-200G-03	115/150	4949
	EG-10-G4-S-200G-04	115/149	4967
	EG-10-G4-S-200G-05	115/150	4929
	EG-10-G4-S-200G-08	117/150	4965
	EG-10-G4-C-200G-03	115/76	1289
	EG-10-G4-C-200G -04	115/76	1283
	EG-10-G4-D-200G-05-T	56/150	2395
	EG-10-G4-D-200G-05-B	56/150	2377
	EG-10-G4-D-200G-08-T	58/150	2473
	EG-10-G4-D-200G-08-B	55/150	2359

3.3.2.2 Numerical Study Approach

Objective 2 was aimed to identify the most suitable geometries for accurately measuring and differentiating the first flexural and longitudinal resonance frequencies. To achieve this, the study was divided into two phases: the first focused on numerical analysis, and the second on experimental validation. The goal was to assess the impact of different geometries on IRT experiments for quality control and to establish best testing practices. In the first phase, a numerical study was conducted. Initially, a modal analysis was performed on the geometries presented in Table 3.5 to estimate the frequency range that should be excited in experimental tests to detect fundamental resonance frequencies. Following this, numerical simulations of IRT were carried out for both longitudinal and flexural vibration modes to determine the resonance frequencies associated with each mode. These simulations were performed using two sets of material properties: one representing conditions at 23 °C and the other at low temperatures, as outlined in the Materials section (Table 3.2).

In the numerical study, finite element simulations were conducted using advanced computational modeling software. Table 3.7 provides a summary of the model types used and their corresponding maximum mesh sizes for each calculation. The selection of mesh size and type was based on prior research, which can be found in previous studies where numerical modeling of IRT was employed to compute FRFs (J.-C. Carret, Pedraza, et al., 2018; Gudmarsson et al., 2014). Due to the test configuration of the longitudinal mode for SGC and cylinder geometry, 2D models were used instead of 3D models to reduce computation time, cutting the IRT simulation duration from approximately 45 minutes to less than 30 seconds. Figure 3.9 presents examples of the 3D and 2D axisymmetric models employed in objective 2.

Table 3.7 Model Types and Mesh Size for Objective 2

Numerical study	Modal analysis			IRT modeling			
	S	C	D	S	C	D	
Geometry	S	C	D	S	C	D	
Modes	-	-	-	Longitudinal	Longitudinal	Symmetric (SY)	Antisymmetric (AS)
Model type	3D			2D axisymmetric	2D axisymmetric	2D axisymmetric	3D
Maximum mesh size (mm)	8	8	5	8	8	5	15

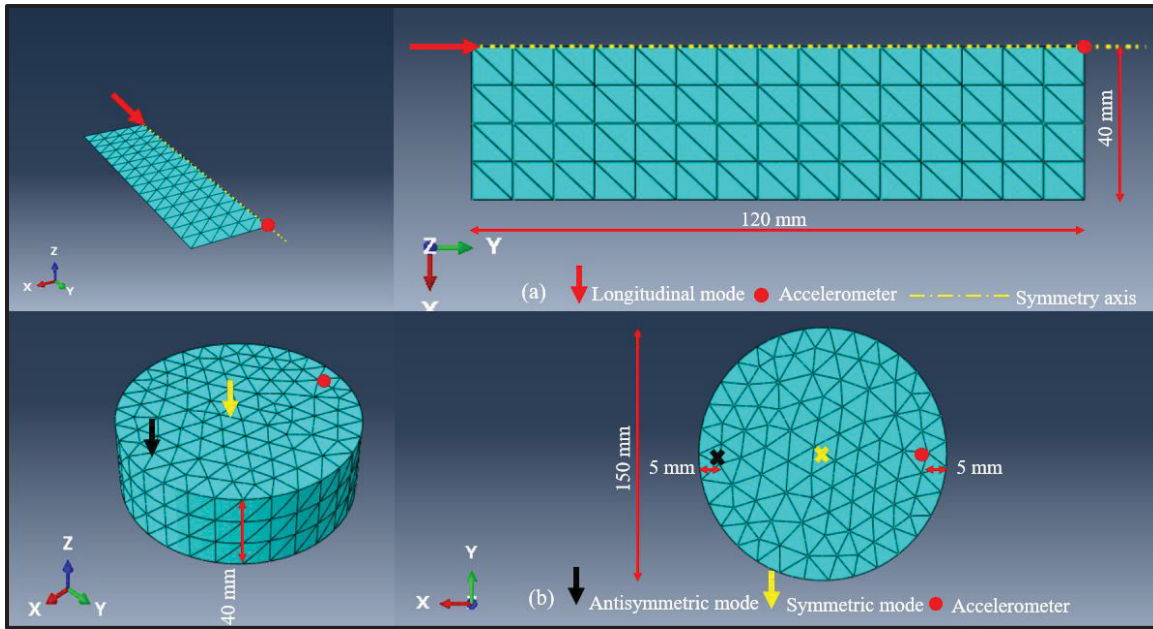


Figure 3.9 Numerical models for objective 2: a) 2D axisymmetric , b) 3D

3.3.2.3 Experimental Study Approach

The second phase involved experimental verification, where specimens were fabricated and tested at both 23 °C and -20 °C. IRT was employed to validate the numerical findings by confirming whether the predicted frequency range was adequate in experiments and verifying the relationship between vibration modes and the observed resonance frequencies. The outcomes of this phase were essential for refining the testing methodology and recommending best practices for quality control using IRT. In the experimental study section, the accelerometer was screwed to a mounting base, which was glued to the specimens before testing in accordance with the recommendation from objective 1. This method was chosen to improve adhesion between the accelerometer and the specimens, ensuring higher signal quality. SGC and cylindrical specimens were tested in longitudinal mode, while disc-shaped specimens were tested in both antisymmetric and symmetric modes. Table 3.8 summarizes the testing modes, and Figure 3.10 shows the IRT configuration used in objective 2.

Table 3.8 Summary of mode of testing in objective 2

Geometry	Specimen ID	Vibration modes			
		Flexural or Antisymmetric (Hz)		Longitudinal or Symmetric (Hz)	
		23 °C	-20 °C	23 °C	-20 °C
SGC (S)	EG-10-G4-S-200G-03	-	-	X	X
	EG-10-G4-S-200G-04	-	-	X	X
	EG-10-G4-S-200G-05	-	-	X	X
	EG-10-G4-S-200G-08	-	-	X	X
Cylinder (C)	EG-10-G4-C-200G-03	-	-	X	X
	EG-10-G4-C-200G -04	-	-	X	X
Disc (D)	EG-10-G4-D-200G-05-T	X	X	X	X
	EG-10-G4-D-200G-05-B	X	X	X	X
	EG-10-G4-D-200G-08-T	X	X	X	X
	EG-10-G4-D-200G-08-B	X	X	X	X

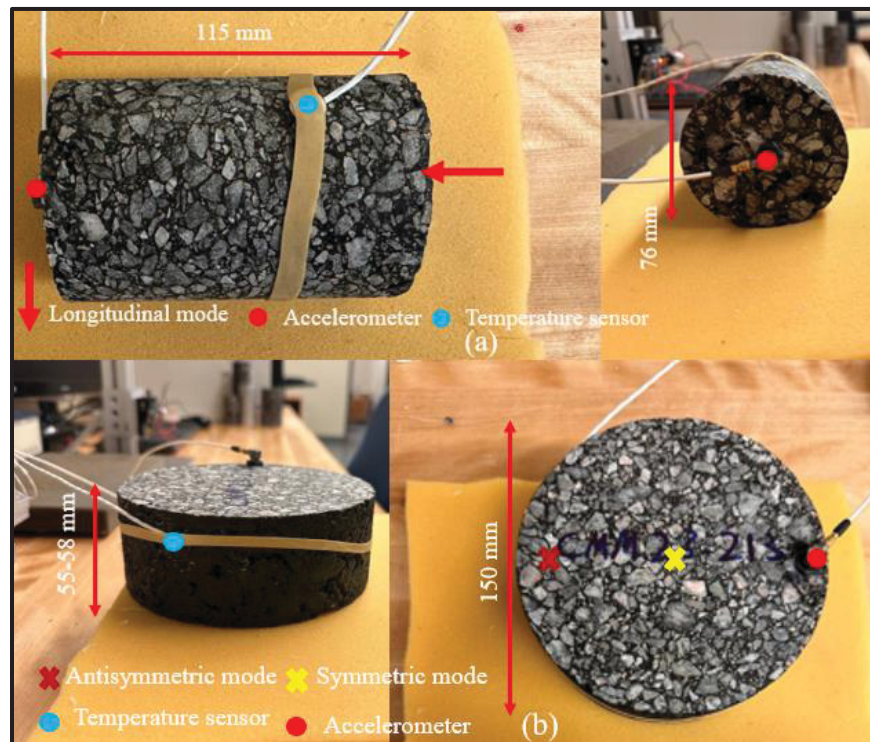


Figure 3.10 IRT in Objective 2: a) Longitudinal, b) Symmetric and antisymmetric

3.3.3 Analytical Investigation of Air Void Content on Mixture properties

The study of air void content in bituminous mixtures is important because it significantly affects the material's mechanical properties and overall performance. Quality control (QC) has traditionally focused on volumetric properties due to their simplicity and relevance to compactability and durability. However, examining the relationship between air void content and advanced mechanical properties like complex modulus and phase angle provides a more comprehensive understanding of how the material behaves under various loading conditions. By exploring this connection, researchers can improve mixture designs, enhance long-term performance predictions, and refine QC practices.

3.3.3.1 Specimens

The specimens in objective 3 are SGC specimens of the ESG-10 mixture, which were previously investigated in objective 1. These specimens were cut in half in the laboratory using a saw machine to create disc-shaped geometries, allowing for an extended study of geometry in objective 2.

It is worth noting that during the preparation of disc shaped specimens from the SGC specimens, the ESG-10-G3-S-80G-03 specimen was destroyed; therefore, the investigation in Objective 3 includes 22 disc geometries. Figure 3.11 presents the nomenclature of the specimens in objective 3, while Table 3.9 summarizes their properties. As illustrated in Figure 3.11, the specimen nomenclature aligns with objective 1. However, the geometry is classified as a disc because the SGC specimens were cut in half. An additional designation was added at the end to indicate whether the disc originated from the top (T) or bottom (B) section of the SGC specimens. Air void content (V_a) was calculated using Equation (3.1). Table 2 presents the bulk specific gravity (G_{mb}), which was derived from the specimens' dry mass and apparent volume. The maximum specific gravity (G_{mm}) for the ESG-10 mixtures was measured as 2.526 for group G1, 2.524 for G2, and 2.521 for G3.

$$V_a(\%) = \frac{G_{mm} - G_{mb}}{G_{mm}} * 100 \quad (3.1)$$

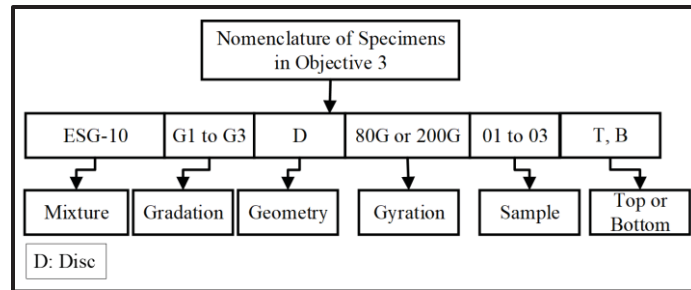


Figure 3.11 Nomenclature of specimens in objective 3

Table 3.9 Specimens properties in the objective 3

Samples number	Specime's ID	Sawn surface			
		H/D (mm)	Mass of specimen in air (g)	G_{mb}	V_a
1	ESG-10-G1-D-200G-T	55/148	2361	2.470	2.2
2	ESG-10-G1-D-200G-B	56/150	2437	2.454	2.9
3	ESG-10-G1-D-80G-01-T	58/149	2449	2.402	4.9
4	ESG-10-G1-D-80G-01-B	57/150	2450	2.427	3.9
5	ESG-10-G1-D-80G-02-T	57/150	2367	2.373	6.1
6	ESG-10-G1-D-80G-02-B	58/150	2458	2.412	4.5
7	ESG-10-G1-D-80G-03-T	58/149	2459	2.454	2.9
8	ESG-10-G1-D-80G-03-B	55/150	2352	2.406	4.7
9	ESG-10-G2-D-80G-01-T	55/150	2409	2.483	1.6
10	ESG-10-G2-D-80G-01-B	57/150	2448	2.448	3.0
11	ESG-10-G2-D-80G-02-T	56/150	2432	2.453	2.8
12	ESG-10-G2-D-80G-02-B	54/150	2373	2.485	1.5
13	ESG-10-G2-D-80G-03-T	55/150	2415	2.488	1.4
14	ESG-10-G2-D-80G-03-B	54/150	2386	2.474	2.0
15	ESG-10-G2-D-200G-T	54/150	2379	2.492	1.2
16	ESG-10-G2-D-200G-B	55/148	2445	2.496	1.1
17	ESG-10-G3-D-200G-T	56/150	2417	2.446	3.0

Table 3.9 Specimens properties in the objective 3 (continued)

Samples number	Specime's ID	Sawn surface			
		H/D (mm)	Mass of specimen in air (g)	G_{mb}	V_a
18	ESG-10-G3-D-200G-B	56/148	2410	2.481	1.6
19	ESG-10-G3-D-80G-01-T	61/150	2437	2.257	10.5
20	ESG-10-G3-D-80G-01-B	59/150	2409	2.302	8.7
21	ESG-10-G3-D-80G-02-T	59/151	2412	2.281	9.5
22	ESG-10-G3-D-80G-02-B	60/151	2429	2.236	11.3

3.3.3.2 Experimental Study Approach

Objective 3 aimed to examine the relationship between air void content, resonance frequency, complex modulus, and phase angle, considering the recommended test setup (sawn surface and glue as the mounting base adhesive, as established in objective 1) and the recommended geometry (disc-shaped specimens to better distinguish flexural or antisymmetric modes from longitudinal or symmetric modes, as determined in objective 2). To achieve this, SGC specimens of ESG-10 were cut in half using a saw machine in the laboratory to produce disc-shaped geometries. These specimens were first tested in both antisymmetric and symmetric modes at 23 °C. The specimens were then placed in a climatic chamber at -20 °C for one day and tested the following day. The mixture properties, including the complex modulus and phase angle, were evaluated using specific analytical methods. Damping and phase angle were determined using the half-bandwidth method, while the complex modulus was calculated with the Martinček method, selected due to the disc-shaped geometry of the specimens, as described in the literature of this dissertation. Finally, the correlation between these properties and the air void content of the specimens was analyzed.

CHAPTER 4

RESULTS AND ANALYSIS

The results of this dissertation are divided into three sections in accordance to the three specific objectives were defined for this dissertation.

4.1 Analysis of Surface Conditions and Adhesive Types

The aim of this part is to recommend the appropriate surface condition and adhesive mounting base to ensure that the test results are accurate and suitable for interpretation. Table 4.1 The color codes that are used in this objective.

Table 4.1 Summary of the color codes in the objective 1















Color codes	Description	Section
	Original (ESG-10, 23 °C)	4.1.1.2 Δt vs. Surface Conditions
	Original (ESG-10, -20 °C)	
	Sawn (ESG-10, 23 °C)	
	Sawn (ESG-10, -20 °C)	
	Original (EG-10, 23 °C)	
	Sawn (EG-10, 23 °C)	
	Sawn (EG-10, -20 °C)	4.1.1.4 Δt vs. Force
	Irregular impacts	
	Damp impacts	
	Acceptable impacts	

Table 4.1 Summary of the color codes in the objective 1 (continued)

Color codes	Description	Section
	Original+ wax (ESG-10, 23 °C and -20 °C)	4.1.2.2 Force vs. MPPA
	Sawn+ Glue (ESG-10, 23 °C and -20 °C)	
	Original+ Paraffin (EG-10, 23 °C)	4.1.2.2 Force vs. MPPA
	Sawn+ Aluminum sticker+ Paraffin+ (Rubber band) (EG-10, 23 °C and -20 °C)	

4.1.1 Influence of Surface Conditions on Applied Impact

The surface conditions of a specimen significantly influence the applied impact, and this can be evaluated using the factor Δt . Whether the surface is sawn or remains in its original condition, these variations can affect the consistency and reliability of measurements. A well-prepared surface generally results in more stable impact responses, while differences in texture may alter energy transfer and force propagation. Recognizing these influences is crucial for ensuring accurate and repeatable outcomes in the impact resonance test.

4.1.1.1 Defination of Δt

Δt represents the time span at 0.707 of the peak force for each individual impact, providing a measure of the duration of the impact event. It is calculated by identifying the time points when the applied force reaches 70.7% of its maximum value, reflecting how the energy is dissipated and how the force propagates through the specimen. This parameter is crucial as it reveals the specimen's response to impact, with a larger Δt indicating a longer duration and greater energy absorption, while a smaller Δt suggests quicker energy transmission. The surface condition of the specimen, such as sawn versus original texture, directly affects the Δt value, influencing the overall impact behavior. Figure 4.1 shows the defination of Δt .

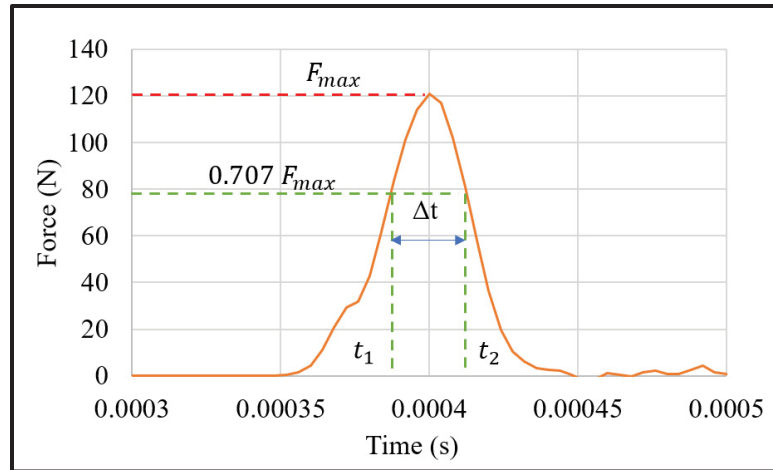


Figure 4.1 Definition of Δt

4.1.1.2 Relation of Surface Conditions and Δt

For each specimen, five impacts were conducted. Initially, the Δt values for each individual impact were calculated, and the averages of the five impacts were presented in Figure 4.2. Additionally, the relative standard deviation (RSD) was calculated to demonstrate the variability of impacts for a specific specimen, comparing the original surface to the sawn surface. As shown in the results in Figure 4.2a, at 23 °C, the average Δt for the original surface is higher than the sawn surface. Moreover, the variability of Δt is higher for all specimens except ESG-10-G1-S-80-02. Conversely, at -20 °C, the results confirm that sawn surfaces exhibit lower Δt values for all specimens, with the variability following a similar trend to that at 23 °C. However, in addition to ESG-10-G1-S-80-02, the specimens ESG-10-G1-S-200G and ESG-10-G3-S-200G also show higher variability in the sawn condition compared to the original condition. The results at -20 °C indicate that the Δt values for sawn surfaces are below 40 μs , while at 23 °C, they are below 50 μs for all specimens. For the original surface at 23 °C, four specimens have values exceeding 70 μs , with the highest being ESG-10-G2-S-80-02 at 107 μs . At -20 °C, seven specimens exhibit values exceeding 70 μs , with the highest being ESG-10-G3-S-80-01 at 166 μs .

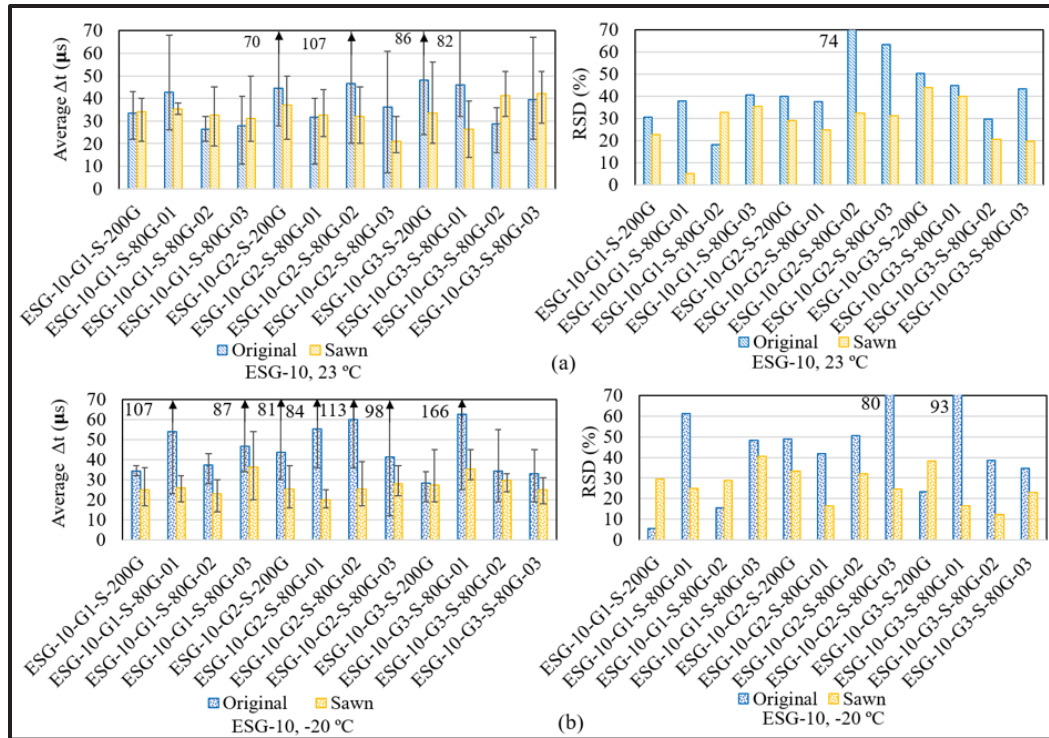


Figure 4.2 Δt vs. surface conditions for ESG-10; a) 23 °C, b) -20 °C

Figure 4.3 shows the results for the EG-10 mixture at 23 °C under the conditions of the original surface and the sawn surface with an aluminum sticker. The results indicate that all Δt values for the sawn surface with the aluminum sticker are below 40 μs , whereas for the original surface condition, the highest value of 111 μs was measured for EG-10-S200G-06.

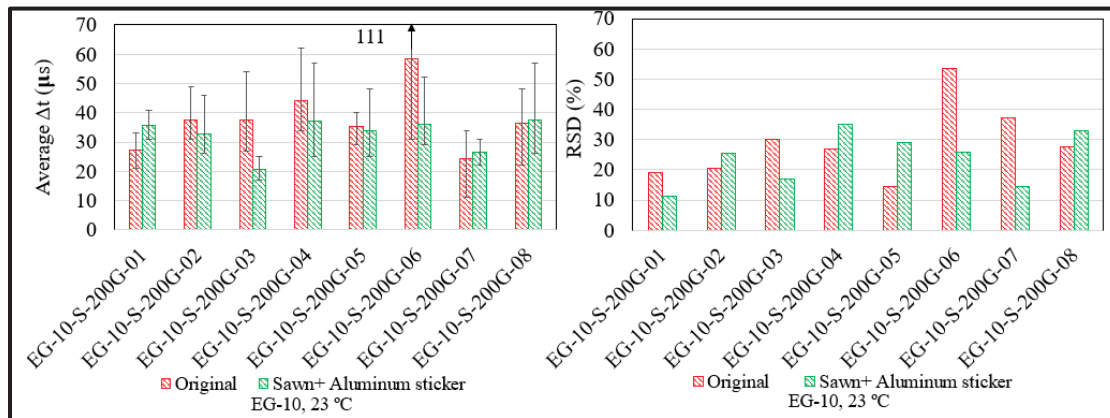


Figure 4.3 Δt vs. surface conditions at 23 °C for EG-10

4.1.1.3 Identification of Outlier Impacts

The 95% confidence interval (CI) is a statistical approach for estimating the likely range of the mean, while the interquartile range (IQR) defines the spread of the middle 50% of a dataset and helps identify its upper boundary (Tosin & Balbinot, 2022; G. Zhang, 2014). Figure 4.4 shows the distribution of Δt values across various specimens and conditions, along with statistical characteristics derived from the data. The blue curve represents a Gaussian (normal) distribution fitted to the data, with a mean (μ) of 35 μs , which is the overall average of all the Δt values across specimens and conditions. This curve illustrates the theoretical distribution of Δt values assuming normality. The green box at the top of the figure indicates the 95% confidence interval (CI) for the mean, ranging from 33.45 μs to 37.18 μs , suggesting that the true mean Δt value is likely to fall within this range with 95% confidence. The red line marks the interquartile range (IQR) upper bound at 72 μs , identifying values above this threshold as statistical outliers. The results show that the original ESG-10 specimens at 23 °C have a wider spread, with several values exceeding the IQR upper bound, indicating higher variability. In contrast, the other specimen types, particularly the sawn ESG-10 specimens, display tighter distributions, with most Δt values falling below 40 μs . Overall, the figure reveals that sawn surfaces, particularly those with aluminum stickers, exhibit more consistent Δt values, while original surfaces at 23 °C show greater variability, with some specimens having significantly higher Δt values. Therefore, Δt values over 72 μs are considered outliers, reflecting damp impacts.

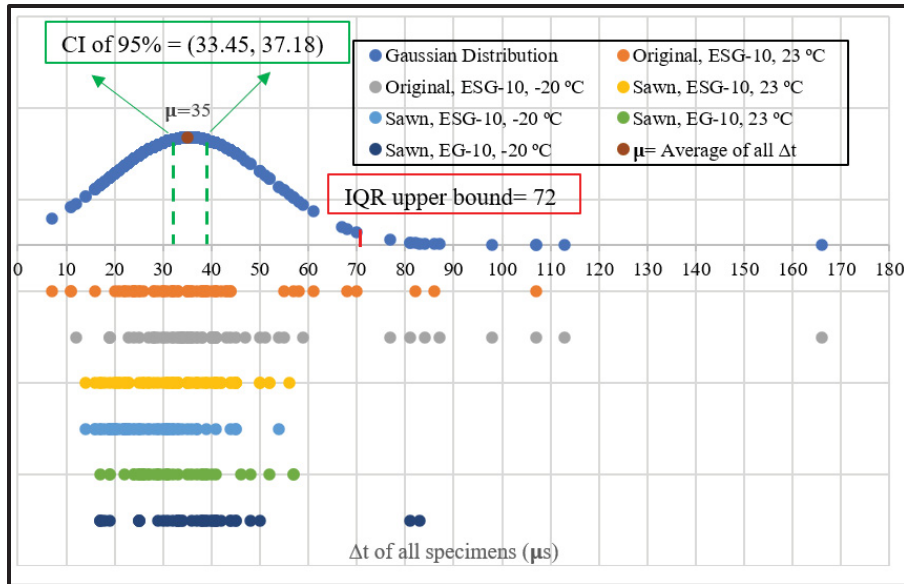


Figure 4.4 Distribution of Δt values across various specimens and conditions

Although damp impacts have been identified, another type of outlier impact occurs when examining the impacts individually. Figure 4.5 illustrates an example of these outlier impacts. As shown in Figure 4.5b, the shape of the acceptable impacts follows a Gaussian curve, which is expected. However, Figure 4.5b is classified as an outlier due to a Δt value exceeding 72 μs . In contrast, the irregular shape in Figure 4.5a deviates from this pattern and is considered unacceptable.

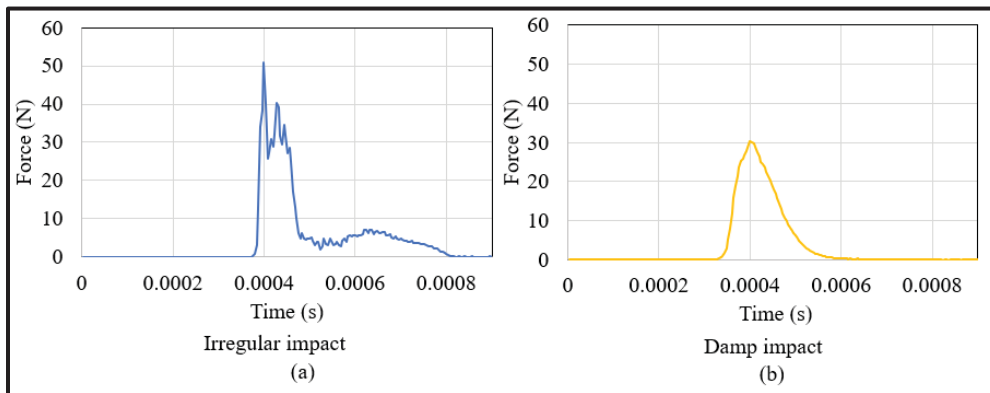


Figure 4.5 Example of outlier impacts; a) Irregular impacts b) Damp impacts

Table 4.2 shows the occurrence of damp and irregular impacts across ESG-10 and EG-10 mixtures. For ESG-10 specimens, at 23 °C, the original surface has 3% damp impacts and 27% irregular impacts, with a total of 30% damp and irregular impacts. At -20 °C, the original ESG-10 surface shows a higher number of damp (8%) and irregular (32%) impacts, resulting in a total of 40%. The sawn ESG-10 specimens at 23 °C show no damp impacts and only 7% irregular impacts, while at -20 °C, no damp or irregular impacts are observed. For EG-10 specimens, the original surface at 23 °C has 2% damp impacts and 35% irregular impacts, totaling 37%. The sawn EG-10 specimens with aluminum stickers at 23 °C show no damp or irregular impacts, and at -20 °C, they exhibit 5% damp impacts and 0% irregular impacts, resulting in a total of 5%. The data shows that surface condition affects the occurrence of damp and irregular impacts. Sawn surfaces, especially those with aluminum stickers, exhibit fewer damp and irregular impacts than original surfaces.

Table 4.2 Summary of the outlier impacts for different surface conditions

Mixtures	Surface condition	Temperature	Damp /total	Damp impacts (%)	Irregular /total	Irregular impact (%)	Total of damped and irregular impacts	Damp and irregular impacts (%)
ESG-10	Original	23 °C	2/60	3	16/60	27	18	30
		-20 °C	5/60	8	19/60	32	24	40
	Sawn	23 °C	0/60	0	4/60	7	4	7
		-20 °C	0/60	0	0/60	0	0	0
EG-10	Original	23 °C	1/40	2	14/40	35	15	37
		-20 °C	-	-	-	-	-	-
	Sawn+ Aluminum sticker	23 °C	0/40	0	0/40	0	0	0
		-20 °C	2/40	5	0/40	0	2	5

4.1.1.4 Relation Between Δt and Force

Since the impacts are applied manually, irregular impacts primarily result from the possibility of hitting with the side of the hammer. Figure 4.6 presents the results for groups with damp impacts, as detailed in Table 4.2. As shown in Figure 4.6, damp impacts occur only in the original surface condition and on the sawn surface with an aluminum sticker (at -20 °C). Furthermore, the results indicate that even on the original surface, no damp impacts occur when the applied force exceeds 60 N.

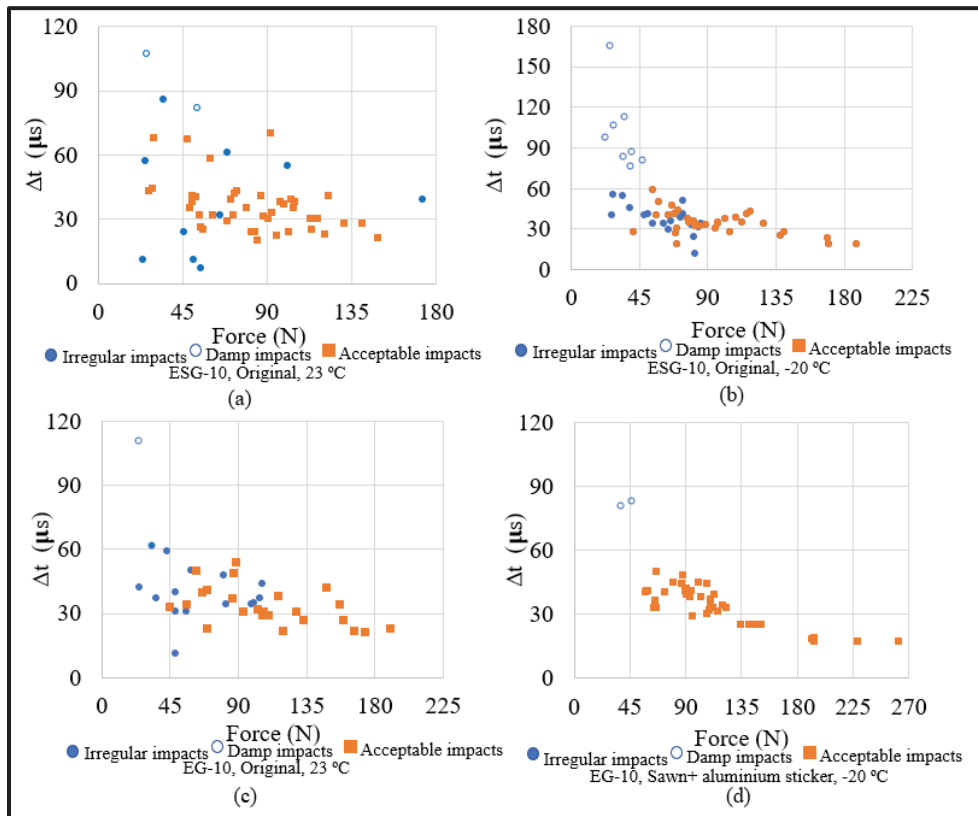


Figure 4.6 Δt vs. force; ESG-10; a) 23 °C b) -20 °C, EG-10; c) 23 °C d) -20 °C

4.1.2 Evaluation of Adhesive Types on Accelerometer Measurement

This section investigates the influence of adhesive choice on the accuracy and reliability of the accelerometer's recorded amplitude during impact resonance tests. The adhesive type can affect the transfer of force and the absorption of energy between the specimen and the measurement system. The goal of this analysis is to determine which adhesive offers the most consistent and precise measurements, ensuring that the accelerometer readings accurately capture the specimen's response to the applied impact, thereby improving adhesion and signal accuracy.

4.1.2.1 Defination of Maximum Peak-to-Peak Amplitude

As shown in Figure 4.7, the maximum peak-to-peak amplitude (MPPA) represents the largest difference between the highest and lowest points of the amplitude waveform recorded during an impact resonance test. This value indicates the full range of amplitude variation that the specimen undergoes, offering a crucial measurement of the specimen's response to the applied impact.

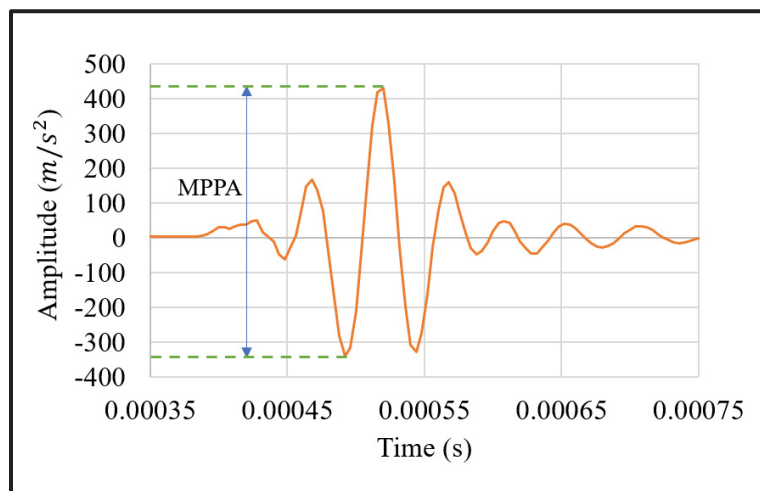


Figure 4.7 Defination of MPPA

4.1.2.2 Relation Between MPPA and Force

Figure 4.8 shows the relationship between maximum peak-to-peak amplitude and applied force. At 23 °C, MPPA increases with force, and this trend is affected by the choice of adhesive mounting base. While wax, paraffin, and glue have minimal impact on the results, glue is preferred as it ensures stable connection and positioning of the accelerometer during tests at different temperatures. At -20 °C, wax and paraffin require a rubber band to secure the mounting base due to the slippery surface. Furthermore, paraffin is not suitable as it fails to show the upward trend in MPPA.

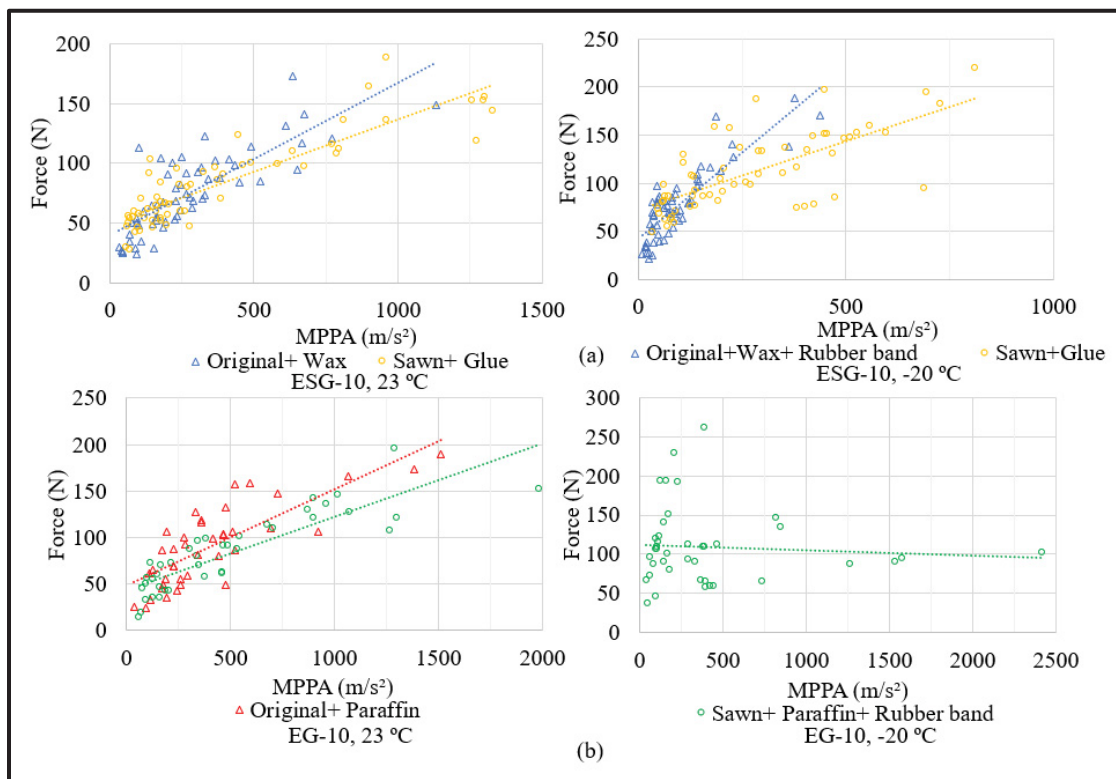


Figure 4.8 Force vs. MPPA; a) ESG-10 b) EG-10

4.1.2.3 Assessment of Noise Level in MPPA

The singular value decomposition (SVD) of the Hankel matrix method can be used to assess noise levels in signal amplitude (Boz, Bekiroglu, et al., 2017). Therefore, this method was applied to evaluate the quality of the measured signal at the maximum peak-to-peak amplitude. The results indicated that system noise was minimal, confirming that the recorded amplitudes were predominantly clean signals. Figure 4.9 illustrates an example of singular value decomposition (SVD) applied to the Hankel matrix for evaluating noise levels. As shown in Figure 4.9b, the green point indicates the necessary singular values required to capture 90% of the signal's energy, as discussed in the literature (Boz, Bekiroglu, et al., 2017). The remaining singular values can be considered noise and set to zero. The Hankel matrix is then reconstructed using only the necessary singular values, represented by the green signal in Figure 4.6a. Consequently, the noise level at MPPA is determined by the difference between the noisy signal and the clean signal at the MPPA point.

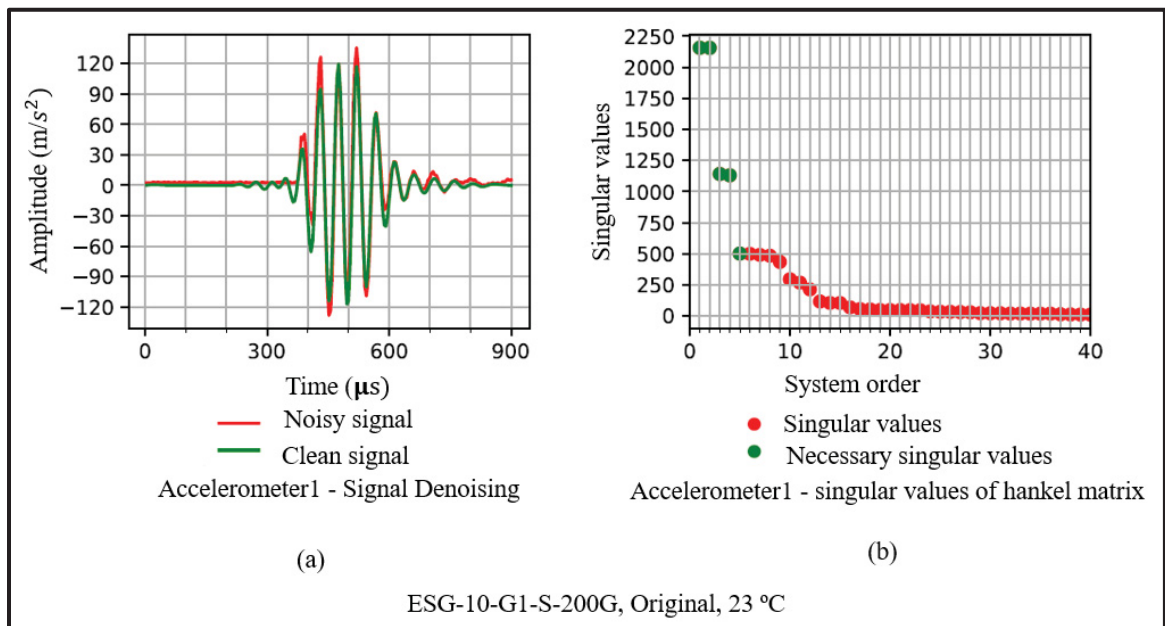


Figure 4.9 Noise level example using SVD of Hankel Matrix

4.1.3 Summary

The findings indicate that sawn surfaces are more suitable for the impacts, as the impact results on the sawn surface show less damp impacts and fewer irregular impacts compared to the original surface. Furthermore, glue is recommended as the adhesive for mounting the specimen due to its superior adhesion properties. The glue-based mounting system enhances the stability of the specimen during testing, improving signal accuracy.

4.2 Influence of Geometries and Test Configuration on FRF Measurement

The aim of this section is to recommend the best test configuration and geometry, using numerical and experimental studies to measure and distinguish the first (or fundamental) flexural and longitudinal resonance frequencies.

4.2.1 Range of Fundamental Resonance Frequency

To reach this objective, a modal analysis was first performed to identify the expected range of the first resonance frequencies. Table 4.3 summarizes the results from modal analysis for the SGC, cylinder, and disc geometries. This analysis reveals that the first flexural and longitudinal resonance frequencies are clearly distinguishable across all geometries at both temperature settings. This distinction is particularly relevant at 23 °C, where damping effects are more pronounced. Among the geometries, the cylinder with an aspect ratio of 2.00 showed the largest frequency gap between the first flexural and longitudinal modes, while the disc with an aspect ratio of 0.27 had the smallest. The frequency separation identified in modal analysis indicates that the flexural and longitudinal resonance peaks from IRT experiments should appear distinctly, helping to minimize the risk of data misinterpretation.

Table 4.3 Modal analysis results

Geometry	Specimen ID	Aspect ratio (AR) (-)	Mode of vibration				$ \Delta f $ (Hz)	
			Flexural (Hz)		Longitudinal (Hz)			
			23 °C	-20 °C	23 °C	-20 °C	23 °C	-20 °C
SGC (S)	S-01	0.80	6983	8552	10088	12355	3105	3803
Cylinder (C)	C-01	2.00	7200	8814	11605	14213	4405	5399
	C-02	1.60	7995	9791	11486	14068	3491	4277
Disc (D)	D-01	0.40	5326	9998	8163	6522	2837	3476
	D-02	0.27	4173	5111	6593	8074	2242	2963

4.2.2 Frequency Response Function Analysis

Figures 4.10 and 4.11 illustrate the outcomes of the numerical simulations for the IRT, representing temperatures of 23 °C and -20 °C, respectively. At 23 °C (Figure 4.10a), no distinct resonance peak was observed for the SGC specimen, which may result from its geometry (aspect ratio= 0.80) and the material's high damping at this temperature. In contrast, at -20 °C (Figure 4.11a), three resonance peaks emerged, likely due to increased material stiffness at lower temperatures. This shift raised the first flexural resonance frequency from 6983 Hz at 23 °C to 8552 Hz at -20 °C, while the first longitudinal resonance frequency increased from 10088 Hz to 12355 Hz.

The cylinder specimen, with an aspect ratio of 1.60, displayed a prominent resonance peak at both temperatures. At 23 °C, its first flexural resonance frequency was 7995 Hz, and the first longitudinal resonance frequency was 11486 Hz, resulting in a frequency gap ($|\Delta f|$) of 3491 Hz. At -20 °C, these frequencies rose to 9791 Hz for the flexural mode and 14068 Hz for the longitudinal mode, expanding $|\Delta f|$ to 4277 Hz.

For the disc specimens, with aspect ratios of 0.40 and 0.27, both fundamental longitudinal and flexural modes were identified. In simulations where the disc was subjected to symmetric loading (SY mode), the fundamental longitudinal mode was dominant, while antisymmetric loading (AS mode) primarily excited the fundamental flexural mode. For the disc with an

aspect ratio of 0.40, the first flexural resonance frequency at 23 °C was 5326 Hz, and the first longitudinal resonance frequency was 8163 Hz. At -20 °C, these frequencies increased to 6522 Hz and 9998 Hz, respectively. For the disc with an aspect ratio of 0.27, the first flexural resonance frequency rose from 4173 Hz at 23 °C to 5111 Hz at -20 °C, while the first longitudinal resonance frequency increased from 6593 Hz to 8074 Hz.

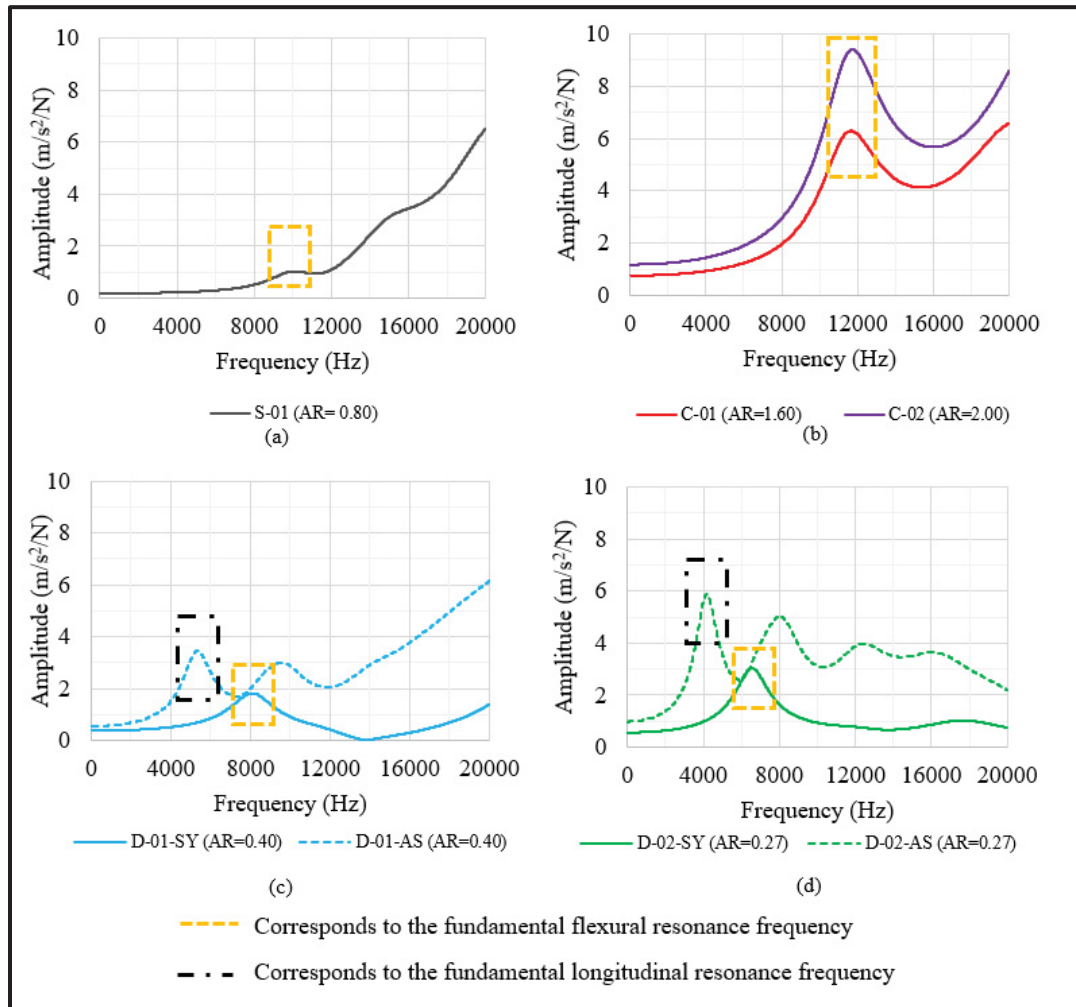


Figure 4.10 Numerical FRF at 23 °C: a) SGC; b) Cylinder; c and d) Disc

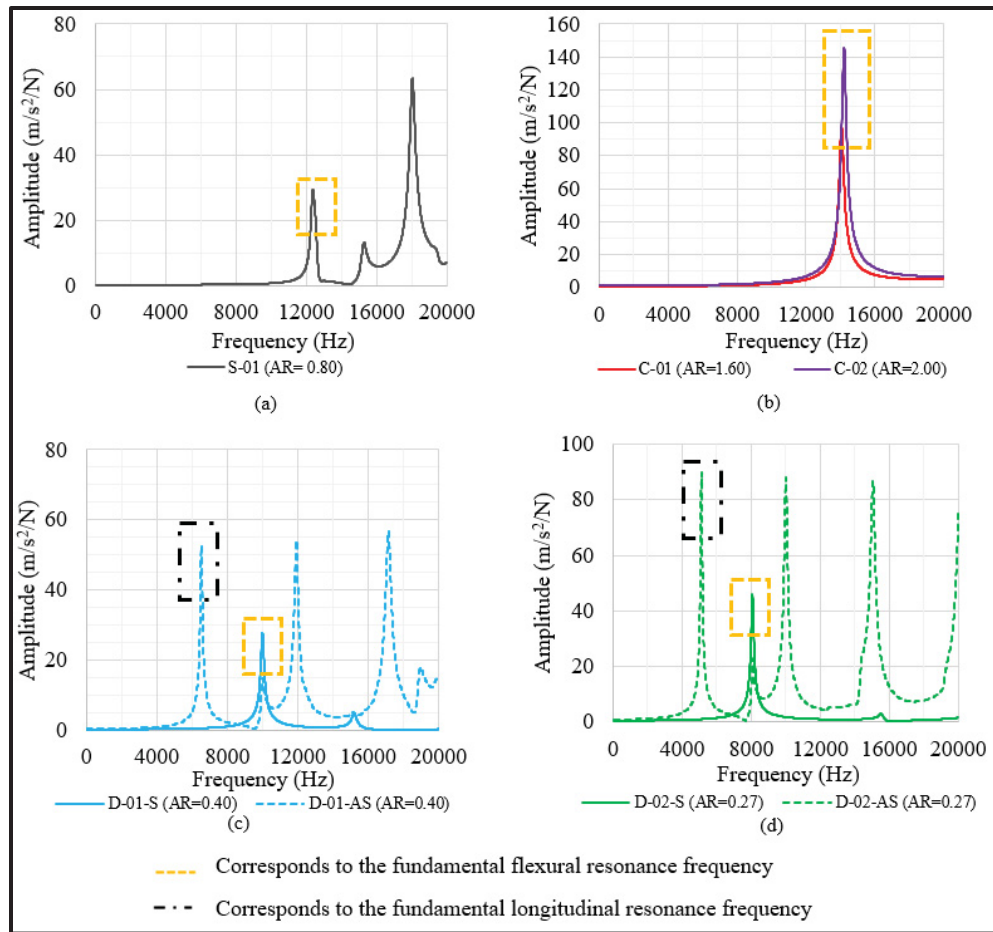


Figure 4.11 Numerical FRF at -20 °C; a) SGC, b) Cylinder, c and d) Disc

The numerical study suggests that at 23 °C, the flexural resonance frequency was not observed in the SGC and cylinder specimens tested in longitudinal mode; however, the longitudinal resonance frequency was successfully detected. In the SGC specimen, this absence may stem from the material's high damping properties, whereas the cylinder exhibited a distinct, isolated peak. For the disc geometry, tested in symmetric mode (aligning with the longitudinal mode), a single isolated peak was identified. In antisymmetric mode (associated with the flexural mode), two main peaks appeared, with the first peak indicating the flexural mode and the second representing the longitudinal mode.

Therefore, at 23 °C, the cylinder and disc geometries are preferred for more accurate measurements. At -20 °C, however, the fundamental resonance frequency was measurable

across all geometries. Multiple peaks were found in both SGC specimens and disc geometries, but since this study prioritizes the fundamental resonance frequency, all geometries are viable. Discs may be preferable due to their well-separated peaks, reducing potential risk of misinterpretation between antisymmetric (flexural) and symmetric (longitudinal) modes.

On the other hand, the experimental IRT findings are summarized in Table 4.4 for both temperature conditions. Figures 4.12 and 4.13 display the FRF outcomes for each specimen at 23 °C and -20 °C, respectively. As shown in Table 4.4, there are no considerable differences in geometry or material properties between the top and bottom sections of the disc specimens, and the Table also presents their fundamental resonance frequencies. Across all specimens and temperatures, coherence values around the first detected frequency ranged between 0.86 and 1. At 23 °C, only the EG-10-G4-S-200G-03 specimen recorded a distinct peak, whereas at -20 °C, three closely spaced peaks were observed for SGC specimens. Consequently, as supported by simulation results, SGC specimens are not ideal for IRT at 23 °C, and at lower temperatures, caution is advised when measuring resonance frequency with SGC specimens.

For the cylinder specimens, detecting the longitudinal resonance peak at 23 °C proved challenging, though a single, distinct peak was recorded at -20 °C. Therefore, cylinder specimens are better suited for testing at lower temperatures. Disc specimens displayed well-separated symmetric and antisymmetric peaks at both temperatures, making them the preferred choice for quality control applications. Additionally, preparing disc specimens is simpler than cylinder specimens, as surface preparation is not required.

Table 4.4 IRT experimental results

Geometry	Specimen ID	Vibration modes			
		Flexural or Antisymmetric (Hz)		Longitudinal or Symmetric (Hz)	
		23 °C	-20 °C	23 °C	-20 °C
SGC (S)	EG-10-G4-S-200G-03	-	-	11304	13378
	EG-10-G4-S-200G-04	-	-	-	13483
	EG-10-G4-S-200G-05	-	-	-	13382
	EG-10-G4-S-200G-08	-	-	-	13280
Cylinder (C)	EG-10-G4-C-200G-03	-	-	12884	17289
	EG-10-G4-C-200G -04	-	-	12992	17277

Table 4.4 IRT experimental results (continued)

Geometry	Specimen ID	Vibration modes			
		Flexural or Antisymmetric (Hz)		Longitudinal or Symmetric (Hz)	
		23 °C	-20 °C	23 °C	-20 °C
Disc (D)	EG-10-G4-D-200G-05-T	4887	7075	7674	10499
	EG-10-G4-D-200G-05-B	5003	7017	7613	10443
	EG-10-G4-D-200G-08-T	5046	7143	7624	10544
	EG-10-G4-D-200G-08-B	4886	6952	7519	10324

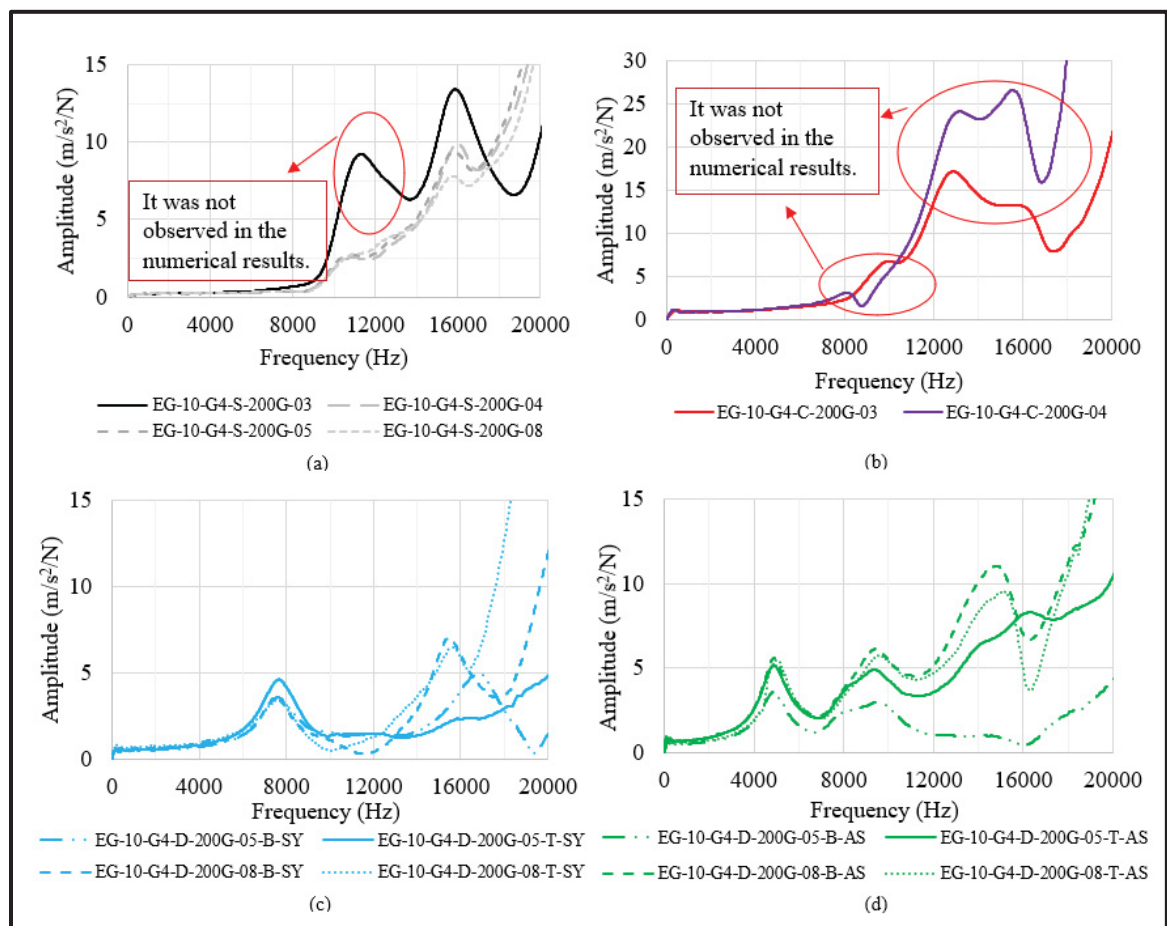


Figure 4.12 Experimental FRF at 23 °C; a) SGC, b) Cylinder, c and d) Disc

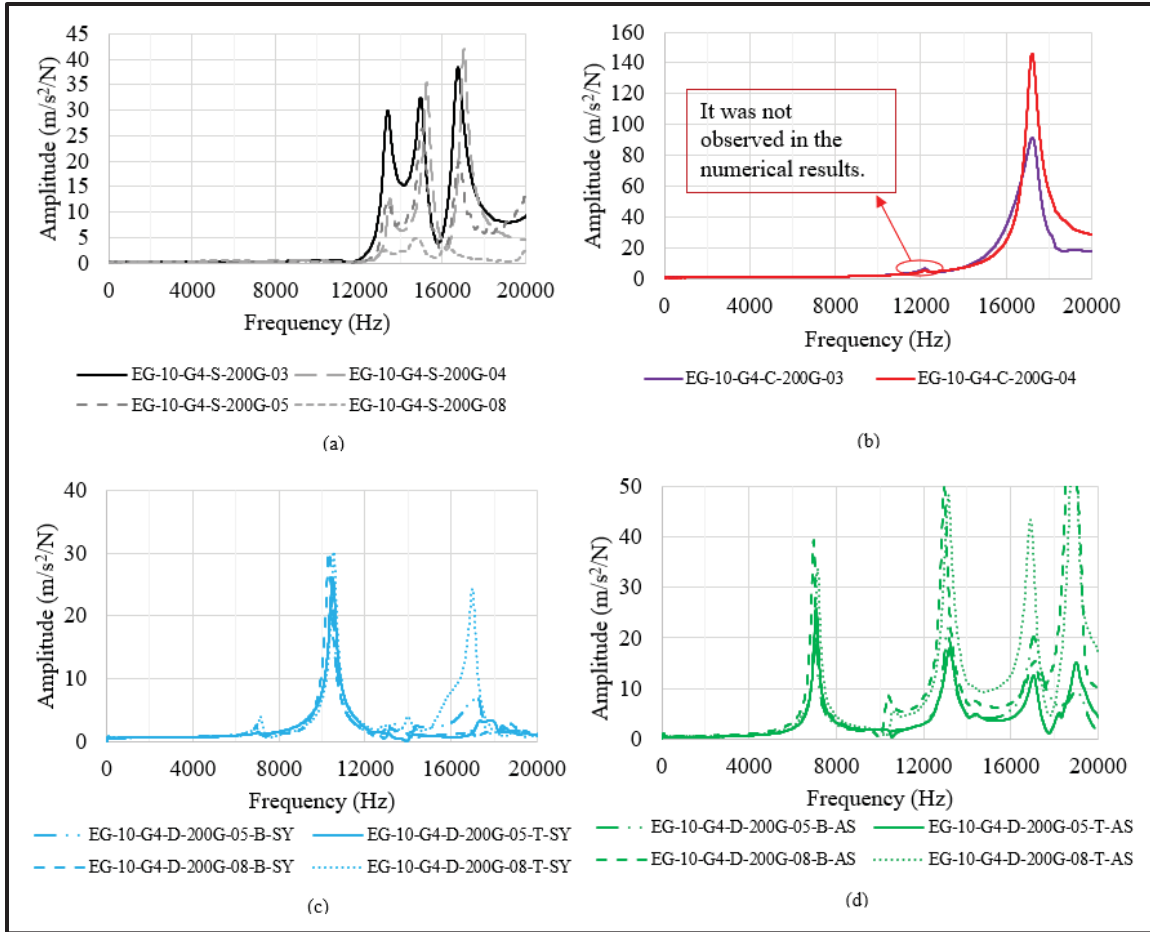


Figure 4.13 Experimental FRF at -20 °C; a) SGC, b) Cylinder, c and d) Disc

4.2.3 Validation of Resonance Frequency Results

To validate the quality of the fundamental resonance frequency, the coherence function around that frequency was checked to ensure it exceeded 0.8 and was close to 1, confirming that the correct frequency was identified as the fundamental resonance frequency (J. Carret et al., 2020; J.-C. Carret, Di Benedetto, & Sauzeat, 2018).

Figure 4.14 presents an example of the frequency response function (FRF) and coherence function at 23°C for EG-10-G4-D-200G-05-T, while the remaining FRFs and coherence functions are provided in Appendices IV and V for Objectives 2 and 3, respectively. It is worth noting that the frequency ranges in Appendices IV and V, like in Figure 4.14, were selected to

only show the measured fundamental resonance frequency. As can be seen from Figure 4.14, the coherence function around the fundamental resonance frequency for both symmetric and antisymmetric modes is close to 1. Therefore, the identified resonance frequency is considered appropriate.

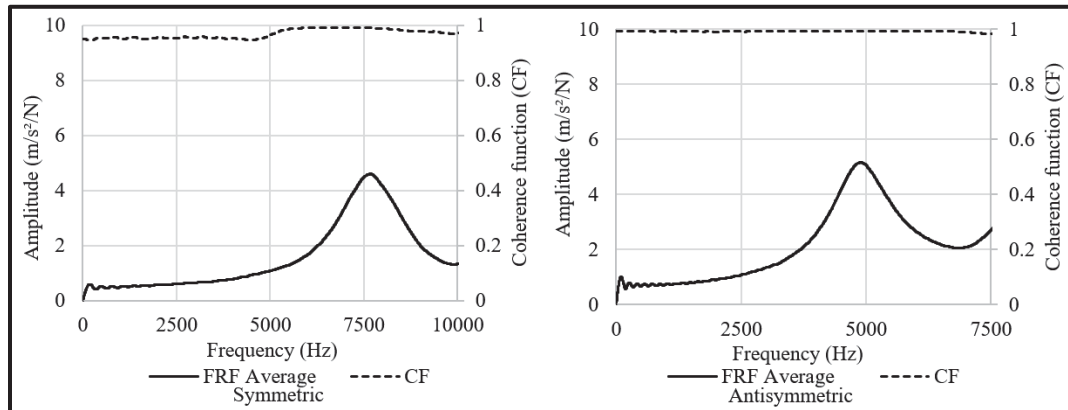


Figure 4.14 FRF and CF for EG-10-G4-D-200G-05-T at 23 °C

4.2.4 Errors in Identifying the Fundamental Resonance Frequency

Table 4.5 provides an evaluation of the risk of incorrectly identifying the fundamental frequency across different specimen types. The number of peaks in Table 4.5 was counted up to 20,000 Hz, and the risk of misinterpretation was ranked as low, moderate, or high.

For SGC specimens, experimental findings indicate a low risk at 23 °C due to two spaced peaks, which make accurate identification challenging. At -20 °C, the experimental tests reveal a high risk, as three peaks appear, further complicating the identification process. However, numerical simulations indicate only a moderate risk at 23 °C and a low risk at -20 °C, where peak separation is clearer under controlled conditions.

For cylinder specimens, Table 4.5 notes a high risk of misidentification in experimental results at 23 °C, where three closely spaced peaks were found. At -20 °C, however, a single distinct peak was observed, leading to a low risk assessment in both experimental and numerical tests. As for disc specimens, both symmetric (S) and antisymmetric (AS) modes exhibit a low risk of misidentification at both temperatures in numerical simulations. At 23 °C, each mode

displays one peak, resulting in a low risk assessment. Experimental results for the symmetric mode also show one peak, confirming a low risk, while the antisymmetric mode presents three distinct peaks. Since this study focuses on detecting the fundamental resonance frequency, the clear separation of these peaks still results in a low risk. At -20 °C, both modes continue to show a low risk, with one peak for the symmetric mode and four for the antisymmetric mode. In summary, the risk assessment across all geometries highlights how closely spaced peaks can complicate fundamental frequency identification. When multiple peaks are present, accurate identification depends on the first peak being distinctly isolated, as demonstrated in the disc specimen analysis.

Table 4.5 Overview of numerical and experimental results in objective 2

Type of study	Geometry	Number of possible peaks		Risk of misinterpretation	
		23 °C	-20 °C	23 °C	-20 °C
Numerical	SGC	2	3	Moderate	High
	Cylinder	1	1	Low	Low
	Disc (S)	1	1	Low	Low
	Disc (AS)	2	3	Low	Low
Experimental	SGC	2	3	Low	High
	Cylinder	2	1	High	Low
	Disc (S)	1	1	Low	Low
	Disc (AS)	3	4	Low	Low

4.2.5 Summary

The findings show that both cylinders and discs are suitable for IRT experiments at -20 °C, but disc specimens are the most suitable geometry for experiments at 23 °C. Moreover, creating discs from SGC specimens is easier than preparing cylinders from cores. Therefore, disc specimens are recommended as the optimal choice for IRT testing.

4.3 Influence of Air Void Content on Complex Modulus and Phase Angle

Table 4.6 presents the properties of disc specimens with different air void contents, measured through impact resonance test (IRT) analysis of the FRF at 23°C and -20°C. In some cases of IRT conducted in the symmetric mode at 23°C, a distinct resonance peak could not be identified in the experimental FRF. As a result, the corresponding values in Table 4.6 are marked with a hyphen, and these specimens were excluded from further analysis in both symmetric and antisymmetric modes to maintain consistency in the test data. This issue likely arises from interference with other vibration modes or excessive damping in the specimens at elevated temperatures. The table includes values for resonant frequencies in both symmetric (SY) and antisymmetric (ASY) modes, phase angle (ϕ), and complex modulus ($|E|$). These properties were calculated using the half-bandwidth method.

Table 4.6 Specimen properties from impact resonance test results

Samples number	V_a (%)	23 °C				-20 °C			
		Frequency (Hz)		ϕ (°)	$ E^* $ (MPa)	Frequency (Hz)		ϕ (°)	$ E^* $ (MPa)
		SY	ASY	SY	SY	SY	ASY	SY	SY
1	2.2	7640	4734	15.6	20,000	10515	7033	1.2	35,000
2	2.9	7282	4794	12.8	18,000	10763	7157	1.7	37,000
3	4.9	7063	4735	8.8	15,000	10446	7000	1.6	32,000
4	3.9	-	4853	-	-	10539	7061	1.6	34,000
5	6.1	7270	4662	12	17,000	10405	6906	3.0	33,000
6	4.5	7242	4545	13.3	17,000	10511	7050	1.8	33,000
7	2.9	8057	5168	10.3	20,000	10548	7078	1.0	33,000
8	4.7	8137	5125	9.2	22,000	10511	7054	1.1	36,000
9	1.6	7667	4745	21.7	22,000	10377	6931	1.9	36,000
10	3.0	-	4792	-	-	10574	7068	1.9	35,000
11	2.8	7216	4445	17.6	18,000	10549	7048	1.4	36,000
12	1.5	6958	4517	11.7	17,000	10447	6950	1.9	38,000
13	1.4	-	4927	-	-	10599	7098	1.4	39,000
14	2.0	7589	4770	14.5	21,000	10546	7032	1.7	39,000
15	1.2	8437	5594	9.9	25,000	10643	7131	1.5	40,000

Table 4.6 Specimen properties from impact resonance test results (continued)

Samples number	V_a (%)	23 °C				-20 °C			
		Frequency (Hz)		ϕ (°)	$ E^* $ (MPa)	Frequency (Hz)		ϕ (°)	$ E^* $ (MPa)
		SY	ASY	SY	SY	SY	ASY	SY	SY
16	1.1	8721	5641	9.9	26,000	11016	7351	1.1	41,000
17	3.0	-	5256	-	-	10734	7170	0.9	38,000
18	1.6	7516	5255	9.9	18,000	10577	7107	0.9	35,000
19	10.5	7033	4311	8.6	13,000	10005	6684	2.3	25,000
20	8.7	6710	4263	14.6	13,000	9863	6721	1.9	27,000
21	9.5	6269	4072	17.9	12,000	9567	6428	2.1	26,000
22	11.3	6339	4204	15.9	11,000	9670	6524	2.2	25,000

4.3.1 Relationship with Measured Frequency

At 23 °C, as shown in Figure 4.15a, the relationship between air void content and resonant frequency varies between the symmetric and antisymmetric modes, with only a limited correlation overall. In the symmetric mode, the low R^2 of 0.5216 indicates a weak connection between air void content and frequency, suggesting that other factors likely play a role at this temperature, reducing the model's predictive value. In contrast, the antisymmetric mode shows a slightly weaker relationship, with a moderate R^2 of 0.5138, indicating that frequency decreases with increased air void content, though this trend should be interpreted cautiously. These observations highlight the potential influence of different vibration modes on the relationship between air void content and frequency at this temperature, emphasizing the need for further investigation into other contributing factors.

While at -20 °C, as illustrated in Figure 4.15b, the relationship between air void content and resonant frequency becomes much clearer for both modes. In the symmetric mode, the high R^2 of 0.7609 reflects a strong negative correlation, showing that air void content is a key factor in determining frequency at this lower temperature. The higher R^2 value implies a stable and reliable trend, where frequency declines as air void content rises. For the antisymmetric mode, the R^2 of 0.7516 still indicates a significant correlation, although it is slightly weaker than in the symmetric mode. The stronger correlations at -20 °C suggest that lower temperatures may help stabilize the impact of air voids on frequency, possibly due to reduced molecular motion

in the mixture. Consequently, the results at -20 °C provide a more dependable foundation for predicting how frequency varies with air void content within the studied range.

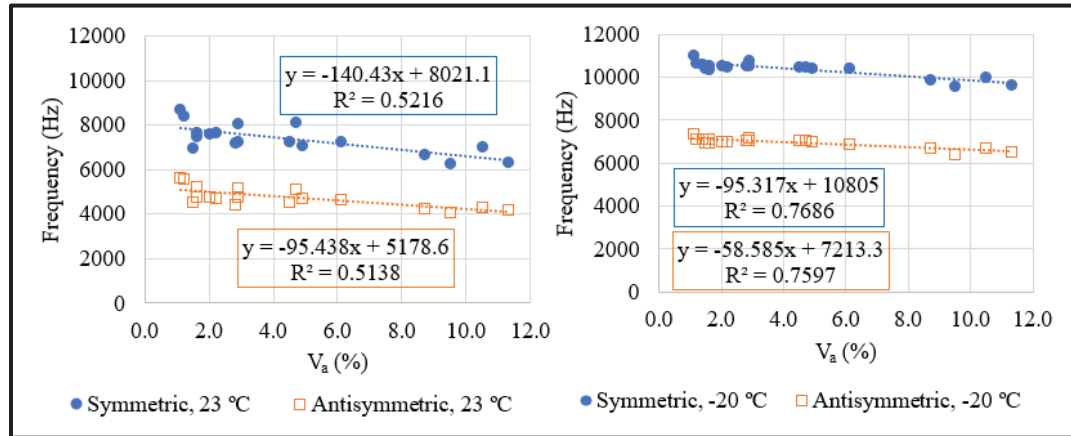


Figure 4.15 Air void content vs. first resonance frequency; a) 23 °C, b) -20 °C

4.3.2 Relationship with Complex Modulus Value

Figure 4.16 illustrates the relationship between air void content and the complex modulus ($|E^*|$) for the symmetric configuration at 23 °C and -20 °C. At 23 °C, the complex modulus decreases moderately as air void content increases, with an R^2 value of 0.6944, indicating a moderate inverse correlation. At -20 °C, the complex modulus values are higher, reflecting greater stiffness due to the lower temperature. The impact of air void content is more pronounced at this temperature, as evidenced by a stronger correlation ($R^2 = 0.8812$), showing a clearer decline in modulus with increasing air voids. These findings suggest that at lower temperatures, air void content has a more significant effect on material stiffness, likely due to increased brittleness and a reduced capacity to redistribute stresses around voids at lower temperatures.

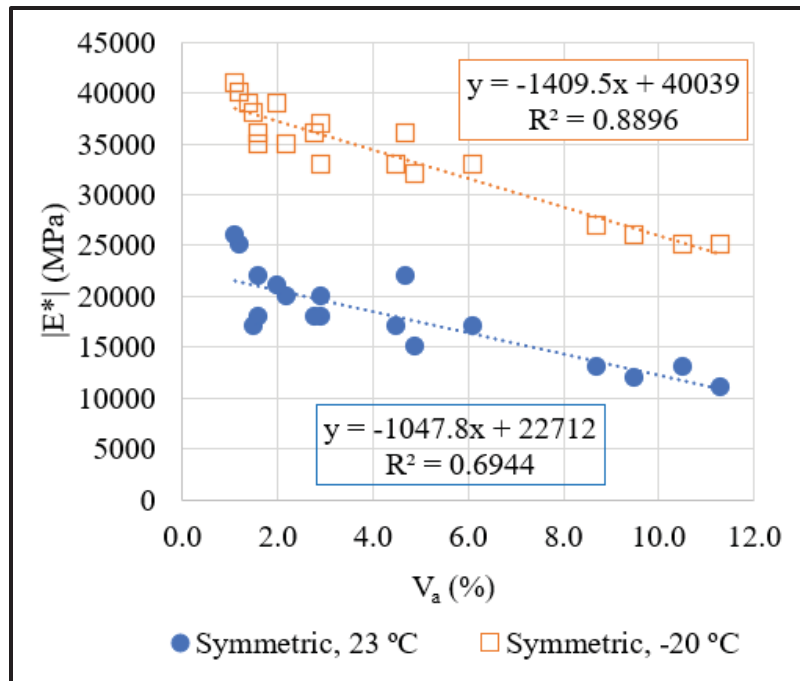


Figure 4.16 Air void content vs. complex modulus

4.3.3 Relationship with Phase Angle

The relationship between air void content and phase angle is presented in Figure 4.17. At 23 °C, the phase angle values of the bituminous mixtures show a scattered distribution, ranging from 4° to 22°, which reflects a tendency toward more viscoelastic behavior. In contrast, at -20 °C, the phase angle values remain consistently low (below 3.5°), indicating a predominantly elastic response. At both temperatures, the phase angle appears largely unaffected by variations in air void content. This stability is likely due to the consistent use of the same binder type and dosage across all specimens, as the binder primarily governs the viscous characteristics of bituminous mixtures.

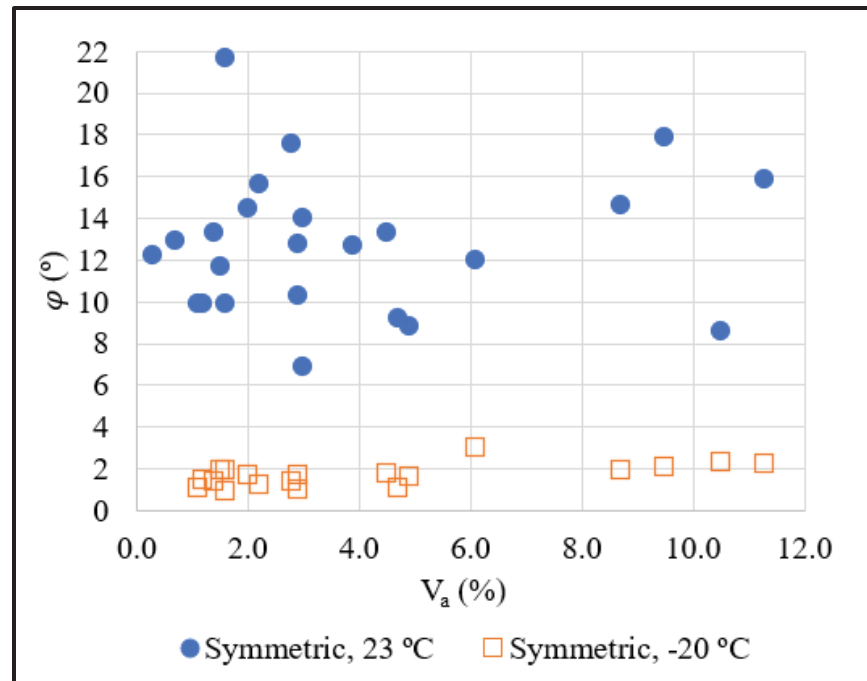


Figure 4.17 Air void content vs. phase angle

CONCLUSION AND RECOMENDATION

This dissertation aimed to evaluate the quality control of bituminous mixtures by examining the complex modulus and phase angle using the impact resonance test (IRT) in relation to air void content (a key volumetric parameter) in quality control. Therefore, ensuring the reliability of the recorded signal is essential for accurately calculating the complex modulus and phase angle from IRT results. Additionally, determining the most suitable specimen geometry is beneficial for obtaining reliable mixture properties. The dissertation is divided into two main sections: experimental and numerical studies. The experimental study involved 20 shear gyratory compacted (SGC) specimens, 26 disc specimens, and 2 cylinder specimens, while the numerical study focused on 1 SGC specimen, 2 cylinders, and 2 discs. The findings are summarized as follows:

- The outlier impact rate on ESG-10 and EG-10 specimens varies with surface conditions. ESG-10 shows a 40% outlier impact rate on the original surface, reduced to 7% with a sawn surface. EG-10 shows 37% of outliers on the original surface and 5% with a sawn surface and aluminum stickers. Therefore, aluminum stickers have a minimal effect, reducing the outlier impact rate by 2%. In other words, for the sawn surface with aluminum stickers, all outlier impacts were damp, whereas outlier impacts without stickers were irregular, likely due to side hits from the hammer. Therefore, it is recommended to saw the surface before testing to achieve better IRT results.
- To avoid damp impacts it is recommended to apply impact force higher than 60 N.
- Disc specimens are the most suitable geometry for IRT experiments at 23 °C. However, at -20 °C, both cylinders and discs are recommended. Nevertheless, cutting SGC specimens to create discs is easier than preparing cylinders from cores.
- To minimize the risk of misinterpretation in both numerical and experimental studies, it is highly recommended to conduct IRT testing using disc geometry in symmetric mode. Using other geometries or antisymmetric modes for disc geometry may result in multiple peaks on the frequency response function (FRF) curves. When these peaks are

closely spaced, the likelihood of misinterpretation increases, which could lead to the selection of incorrect resonance frequencies.

- At 23 °C, the correlation between air void content and resonant frequency is weak, with a low $R^2 = 0.5216$ in the symmetric mode. In contrast, at -20 °C, the correlation strengthens significantly (symmetric $R^2 = 0.7609$), indicating that lower temperatures stabilize the effect of air voids on frequency, improving prediction reliability.
- The complex modulus decreases as air void content increases, with a stronger correlation at -20 °C (symmetric $R^2 = 0.8812$). This suggests that lower temperatures make the material more sensitive to air voids, leading to a greater reduction in stiffness due to increased brittleness.
- At 23 °C, the phase angle shows a scattered pattern indicating more viscoelastic behavior, while at -20 °C, it remains consistently low, reflecting elastic behavior; hence, the phase angle is minimally influenced by air void content due to the consistent binder type and dosage across all specimens.

The following suggestions are made for future studies:

- To investigate how bitumen content and bitumen binder type affect the fundamental resonance frequency.
- Investigating the Link Between Result Variability and Quality Control Practices.
- To investigate how gradation affects the fundamental resonance frequency.
- To evaluate the bituminous mixture properties of different percentages of reclaimed asphalt concrete (RAP) in the mixture.
- To investigate how induced cracks affect fundamental resonance frequency measurement.

APPENDIX I

IMPACT RESONANCE TEST PROTOCOL

The following steps should be followed as the test protocol for performing the Impact Resonance Test (IRT) on bituminous mixtures, aimed at quality control through the identification of the fundamental resonance frequency. To ensure reliable and interpretable results, the following parameters should be considered as part of the test protocol:

1. Geometry selection and surface condition

- Since at 23 °C or higher the specimens behave more viscously, the disc geometry is recommended, as it provided a clearer measurement of the fundamental resonance frequency compared to the SGC and cylinder geometries.
- Since at -20 °C or lower temperatures the specimens behave more elastically, in addition to the disc geometry, the cylinder geometry is also suitable. However, preparing a cylinder requires first sawing the SGC specimen and then coring it to achieve the desired shape, whereas preparing a disc is easier, as it only involves cutting the specimen in half.

2. Accelerometer installation

- Attach the mounting base (plastic mounting base, as shown in Figure A-I-1) to the specimen surface using adhesive glue (instant liquid glue) to ensure a reliable connection between the accelerometer and the specimen. This stable setup ensures consistent signal acquisition and minimizes measurement variability across different temperatures.

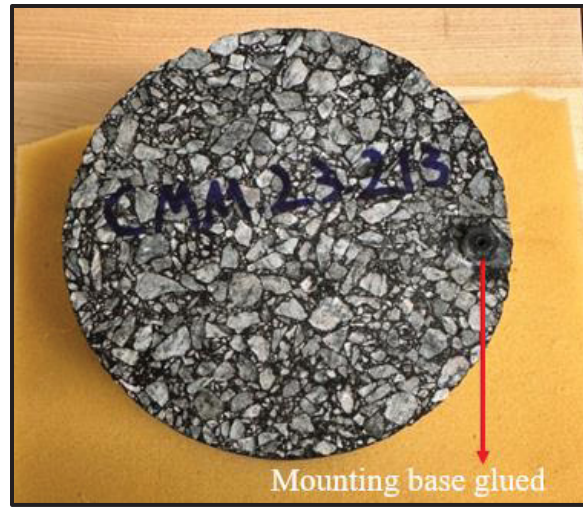


Figure-A I-1 Mounting base attached to the specimen

- After the base is secured, screw the accelerometer firmly onto the mounting base (Figure A-I-2).

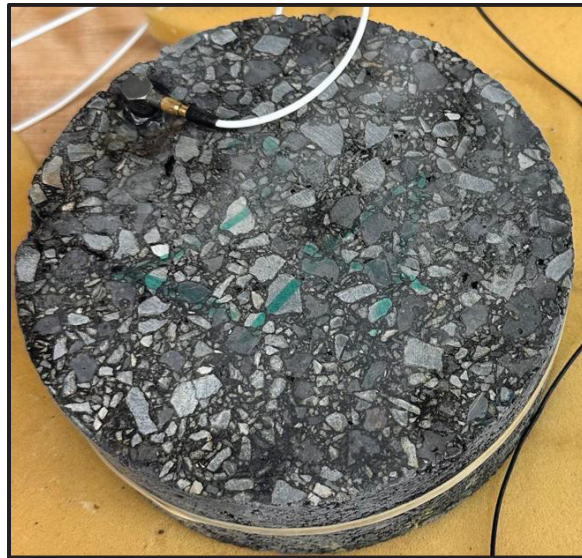


Figure-A I-2 Accelerometer screwed to the mounting base

3. Boundry condition

- Place the specimen on a soft foam or rubber pad, selected based on the specimen geometry. This support helps to reduce boundary reflections and isolate the specimen during impact.

4. Sensor and equipment check

- Place the temperature sensor on the specimen surface to monitor temperature during the test (Figure A-I-3).

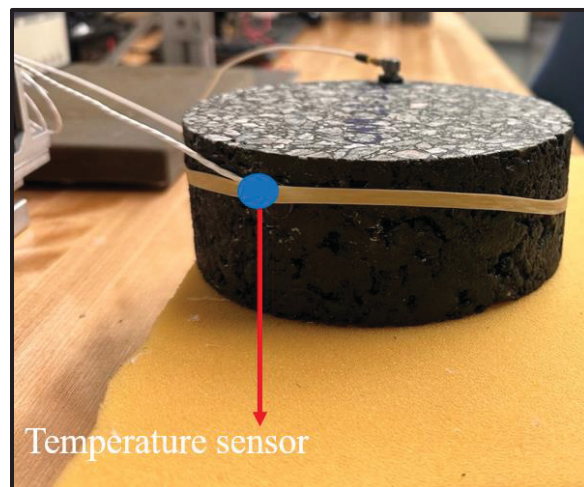


Figure-A I-3 Placement of the temperature sensor

- Confirm that the data acquisition system is properly configured. In this study, a sampling rate of 250,000 samples per second was used, with a measurement duration of 0.009 seconds.

5. -20 °C testing procedure

- At -20 °C, the specimen must be tested within one minute of removal from the thermal chamber to ensure accurate temperature conditions. If the test cannot be completed within

this time frame, the specimen must be returned to the thermal chamber and allowed to stabilize for 15 minutes before retesting.6. Impact verification

- To ensure accurate and valid results, double impacts must be avoided during testing. In other words, an acceptable impact is characterized by a Gaussian-shaped curve, as shown in Figure A-I-4. Otherwise, the impact should be discarded and another impact should be applied to the specimen in order to ensure repeatability of the test. Five acceptable impacts are required.

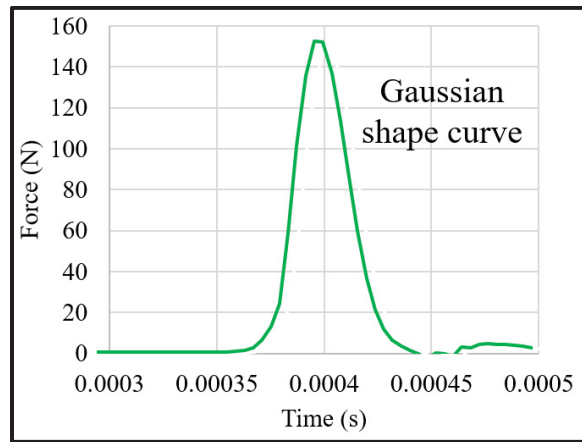


Figure-A I-4 Acceptable impact

- According to the recommendations of this dissertation, to avoid damped or irregular impacts, the applied force should be greater than 60 N. However, to prevent damage to the impact hammer, the force should remain below 200 N.

7. Signal quality verification through coherence function

- The coherence function value near the resonance frequency should be close to 1. If it falls below 0.8, the measurement may be affected by noise and should be repeated.

APPENDIX II

ESG-10 MATERIAL PROPERTIES

Table-A II-1 Description of aggregate distribution for the ESG-10 mixture (G1)

Cumulative weight						
Sieve size	Crushed sand (0-5 mm)	Manufactured crushed sand (0-5 mm)	Crushed stone (2,5-10 mm)	Crushed stone (5-10 mm)	Steel slag (5-10 mm)	Filler (0-80 µm)
10	0	0	6.1	38.7	124.4	0
5	25.8	17.2	454.7	580.6	1285.6	0
2.5	619.3	369.9	596	625.8	1340.9	0
1.25	1316	653.7	602.1	625.8	1354.7	0
0.63	1754.7	782.7	608.3	632.2	1354.7	0
0.315	2012.8	817.1	608.3	632.2	1354.7	0
0.16	2167.6	825.7	608.3	632.2	1354.7	0
0.08	2255.3	836.1	608.3	636.7	1367.2	6.1
0.01	2580.5	860.2	614.4	645.1	1382.4	61.4

Table-A II-2 Description of aggregate distribution for the ESG-10 mixture (G2)

Cumulative weight						
Sieve size	Crushed sand (0-5 mm)	Manufactured crushed sand (0-5 mm)	Crushed stone (2,5-10 mm)	Crushed stone (5-10 mm)	Steel slag (5-10 mm)	Filler (0-80 µm)
10	0	0	6.1	38.7	124.4	0
5	31.9	4.9	454.7	580.6	1285.6	0
2.5	766.7	105.7	596	625.8	1340.9	0
1.25	1629.3	186.8	602.1	625.8	1354.7	0
0.63	2172.4	223.6	608.3	632.2	1354.7	0
0.315	2491.9	233.5	608.3	632.2	1354.7	0
0.16	2683.6	235.9	608.3	632.2	1354.7	0
0.08	2792.2	238.9	608.3	636.7	1367.2	6.1
Filler	3194.8	245.8	614.4	645.1	1382.4	61.4

Table-A II-3 Description of aggregate distribution for the ESG-10 mixture (G3)

Cumulative weight						
Sieve size	Crushed sand (0-5 mm)	Manufactured crushed sand (0-5 mm)	Crushed stone (2,5-10 mm)	Crushed stone (5-10 mm)	Steel slag (5-10 mm)	Filler (0-80 µm)
10	0	0	6.1	38.7	124.3	0
5	16	36.8	454.2	580	1284.3	0
2.5	383	791.8	595.4	625.1	1339.6	0
1.25	813.9	1399.4	601.5	625.1	1353.4	0
0.63	1085.2	1675.6	607.6	631.6	1353.4	0
0.315	1244.8	1749.3	607.6	631.6	1353.4	0
0.16	1340.5	1767.7	607.6	631.6	1353.4	0
0.08	1394.8	1789.8	607.6	636.1	1365.8	6.1
Filler	1595.8	1841.4	613.8	644.5	1381	61.4


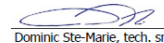
		Les Industries McAsphalt Itée MCA - VALLEYFIELD 950 BOUL. GERARD CADIEUX VALLEYFIELD, QC J6T 6L4 Téléphone: 450-377-8420 Télécopieur: 450-377-8411	
		N° de l'attestation de conformité 224-1058289	
Bitumes - Attestation de conformité			
RENSEIGNEMENTS GÉNÉRAUX		RECOMMANDATION DES TEMPÉRATURES D'UTILISATION	
Distributeur lieu d'entreposage et d'expédition			
Les Industries McAsphalt Itée - VALLEYFIELD		Entreposage	Minimale 140 °C Maximale 175 °C
Fabricant et lieu de fabrication			
Les Industries McAsphalt Itée - VALLEYFIELD		Malaxage (à chaud)	156 °C 170 °C
Classe de performance			
PG 64H-28			
N° de lot	Date de fabrication	RÉSULTATS DES ESSAIS DE CONTRÔLE	
LOT169054	27/09/2022		
RÉSULTATS DES ESSAIS DE CARACTÉRISATION		Date des essais de contrôle 27/09/2022	
Date de la caractérisation	27/09/2022	G' / sinδ (bitume d'origine) (kPa)	1.899
G' / sinδ Orig (kPa)	1.899	Module de rigidité S contrôlé (80) (MPa)	107
Temp. élevée de caractérisation (Te) (°C)	69.8	Pente m origine (80)	0.464
Viscosité Brookfield à 135°C (Pa.s)	0.848	Jnr3,2 (kPa ⁻¹)	0.93
Viscosité Brookfield à 165°C (Pa.s)	0.244	Jnr diff (%)	57.81
Point d'éclair (°C)	316	R3-2 (%)	48.14
Stabilité au stockage (°C)	0.8	Niveau de sollicitation Selon Jnr 3.2 selon Jnr 3.2	"V"
TBA Moyenne (°C)	53.2	EXPÉDITION	
Teneur en cendre (%)	0.133	Numéro et nom de la centrale d'enrobage	
Masse volumique à 25°C (g/cm³)	1.026	PAVAGES VARENNES	
Masse volumique à 15°C (g/cm³)	1.031	Transporteur	
Enrobage Résiduel (%)		N° de la citerne	Date du chargement
Module de rigidité (80) (Mpa)	107	190/B708/21 CARON	05/10/2022
Pente m origine (80)	0.464	Quantité livrée (Kg) 38610	
Variation de masse au RTFO (%)	-0.451	Notes	
Température de l'essai MSCR (°C)	64		
Comp. non-rec. Jnr, 3.2 kPa (1/kPa)	0.93		
Comp. non-rec. diff. Jnr-diff (%)	57.81		
Recouvrance d'élasticité, 3.2kPa (%)	48.14		
Niveau de sollicitation Selon Jnr 3.2	"V"		
Température base de caractérisation Tb (°C)	-30.5		
Delta Tc après RTFOT et PAV 40 h			
REMARQUES			
Préparé par	Date	Approuvé par	Date
Valerie Plourde Lab Supervisor	29/09/2022	Valerie Plourde Lab Supervisor	29/09/2022
ESPACE RÉSERVÉ AU MINISTÈRE DES TRANSPORTS			
N° du contrat	Soumis par (organisme de contrôle)		
Prélevé par	Date	A l'usage du laboratoire	
N° du réservoir à la centrale d'enrobage	Température	Date de réception	
	°C		

Figure-A II-1 PG 64H-28 properties

APPENDIX III

EG-10 MATERIAL PROPERTIES

Classe granulaire		Type	Provenance	28 mm	20 mm	14 mm	10 mm	5 mm	2.5 mm	1.25 mm	0.630 mm	0.315 mm	0.160 mm	0.080 mm	% utilisé	D. Brute	D. App.	% abs
5-10 mm	P	Sables LG, St-Hippolyte		100	100	100	90	10,0	4	3	2	2	2	1,3	60,5	2,721	2,756	0,48
0-5 mm Lavé	CL	Sables LG, St-Hippolyte		100	100	100	100	95,0	59	37	24	14	7	2,6	11,0	2,718	2,749	0,44
0-5 mm	CR	Sables LG, St-Hippolyte		100	100	100	100	93,0	64	45	34	25	17	10,8	26,7	2,718	2,746	0,43
Filler	F	Bauval CMM, Ville St-Laurent (085)		100	100	100	100	100,0	100	100	100	100	100	100,0	1,8	2,700	2,775	1,00
Combiné				100	100	100	94	43,1	28	20	15	11	8	5,8	100,0	2,720	2,753	0,47
Extract. non-lavée LC 26-350				100	100	100	94	43,1	28	20	15	11	8	5,5	Essai PCG			
Référence lavée LC 26-006				100	100	100	94	43,1	28	20	15	11	8	5,8				
Fuséau du mélange						100	90	40,0						4,0	Girations :	10	80	200
Fuséau de restriction suggéré du mélange							100	48,0						10,0	% vide :	14,9	5,9	3,0
								46	31	23	18				Exigence :	≥11,0	4,0	≥2,0
								46	37	27	18							
% de bitume de la formule :		5,27	FBE :		10,18		PBA :		0,22		Présenté à :		Pierre Lyonnais					
% de bitume vierge :		5,27	SST :		5,13		% VBE :		12,4		Fonction :		Directeur technique – Enrobés					
% de bitume dans le recyclé :			% VAM :				DGE :		2,736		Présenté par :		Maxim Cardinal					
Total granulométrique :		425	% VCB :				PBI estimé :		5,28		Fonction :		Chargé de projets – Laboratoire					
Densité brute :			Stab. :				Densité maximale au PBI estimé :		2,515		Vérifié par :							
Densité maximale :		2,515	Déformation :								Date :		Dominic Ste-Marie, tech. sr					
% de vide :			Bitume eff. :		5,06								2023-03-24					
Tenue à l'eau :			Comp. Ant. :															
Remarques																		

LE006 (R00 25-03-13)

Page 1 de 3

Figure-A III-1 EG-10 bituminous mixtures mix design

INFORMATIONS GÉNÉRALES		RECOMMANDATIONS - TEMPÉRATURE D'UTILISATION	
Distributeur et lieu d'entreposage et d'expédition Bitumar Inc. 3000 Broadway, Montréal, QC, H1B 5B4		Entreposage	Minimale 138
Fabricant et lieu de fabrication Bitumar Inc. 3000 Broadway, Montréal, QC, H1B 5B4			Maximale 175
Classe de bitume PG 64E-28 THRD		Plage Malaxage	150
Nom commercial PG 64E-28 THRD			
N° de lot 2364E28THRD-04		Date de fabrication 29/05/2023	
ESSAIS DE CARACTÉRISATION		ESSAIS DE CONTRÔLE	
Date des essais de caractérisation	01/06/2023	Date des essais de contrôle	01/06/2023
Point d'éclair, °C, ASTM D92	304	G'/Sinδ, (origine) à 64 °C (kPa)	3.07
Masse volumique (g/cm³), à 25°C, AASHTO T228	1.019	Rigidité à -18°C, Sc (60) (MPa)	84.2
Masse volumique (g/cm³), à 15°C, AASHTO T228	1.025	Pente de mc (60)	0.453
Viscosité Brookfield (Pa·s), à 135°C, AASHTO T 316	1.132	JNR3.2 à 64 °C, (kPa-1)	0.26
Viscosité Brookfield (Pa·s), à 165°C, AASHTO T 316	0.319	JNRDIFF (%)	47
Stabilité au stockage (°C), LC 25-003	0.3	Niveau de sollicitation selon JNR3.2	E
TBA moyenne (°C)	60.1	R3.2 (%)	69.9
Teneur en cendres (%)	0.2	NOTES	
G'/Sinδ, bitume d'origine à 64°C (kPa)	3.07	Ce produit doit être entreposé dans un réservoir vide ou contenant le même grade fournis par Bitumar Inc. Si ce n'est pas le cas, il est de votre responsabilité de prendre les mesures nécessaires pour confirmer la caractérisation du produit.	
Température élevée de caractérisation Te(°C)	75.7		
Module de rigidité à -18°C, So (60) (MPa)	84.2	Peu importe les recommandations du fournisseur, L'entrepreneur doit respecter les documents contractuels.	
Pente à -18°C, mo (60)	0.453		
Enrobé résiduel (%) (LC25-009)	95		
Bitume vieilli au RTFO			
Variation de masse au RTFOT (%)	-0.542		
JNR3.2 à 64°C, (kPa-1)	0.26		
JNRDIFF (%)	47		
R3.2 (%)	69.9		
Niveau de sollicitation selon JNR3.2	E		
Bitume vieilli au RTFO et PAV			
Module de rigidité à -18°C, s (60), MPa	170		
Pente à -18°C, m(60)	0.333		
Température basse de caractérisation Tb(°C)	-31.1		
ΔTc après RTFOT et PAV 40 h (°C)	N.A.		
REMARQUES			
Signé par: Paula Marc		Date 01/06/2023	

F-PS-07.2 R3

Figure-A III-2 PG 64E-28 THRD properties

APPENDIX IV

FRF AND CF FOR OBJECTIVE 2

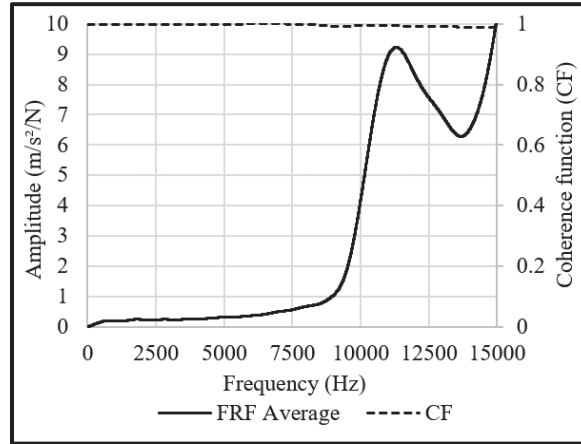


Figure-A IV-1 FRF and CF for EG-10-G4-S-200G-03 at 23 °C

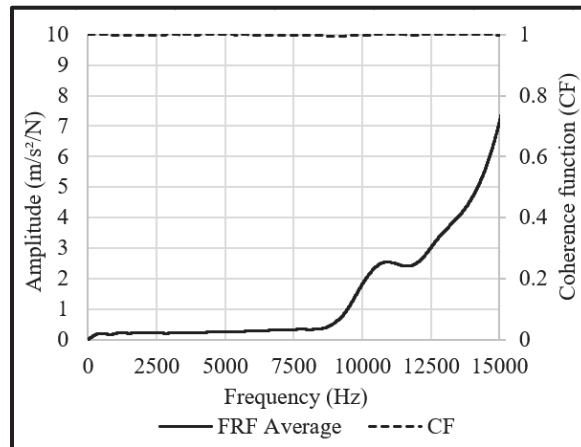


Figure-A IV-2 FRF and CF for EG-10-G4-S-200G-04 at 23 °C

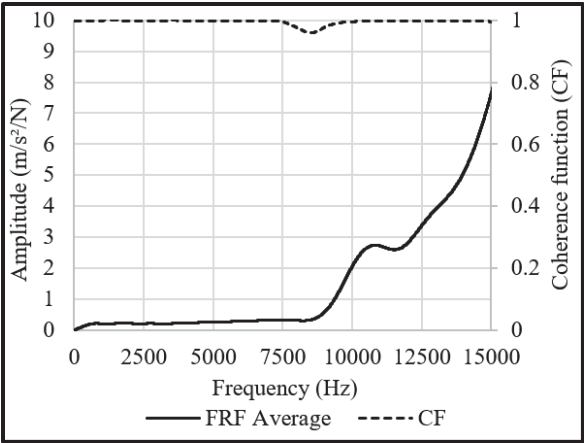


Figure-A IV-3 FRF and CF for EG-10-G4-S-200G-05 at 23 °C

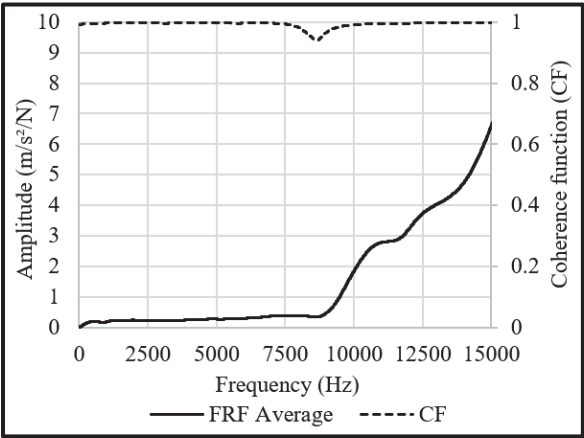


Figure-A IV-4 FRF and CF for EG-10-G4-S-200G-08 at 23 °C

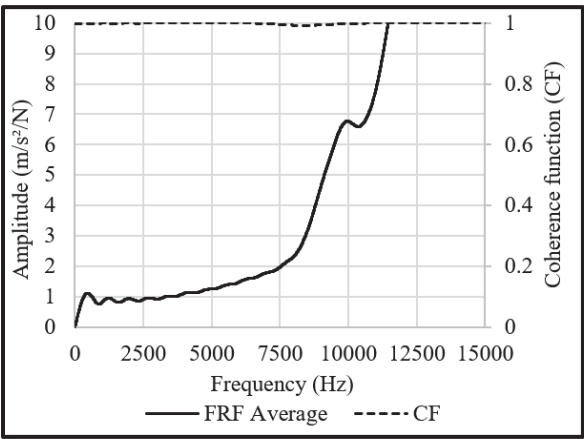


Figure-A IV-5 FRF and CF for EG-10-G4-C-200G-03 at 23 °C

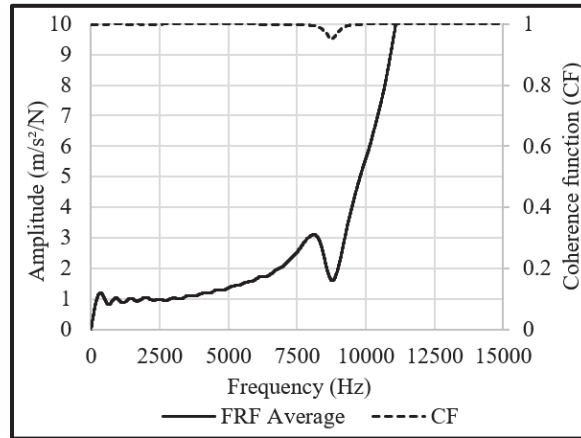


Figure-A IV-6 FRF and CF for EG-10-G4-C-200G-04 at 23 °C

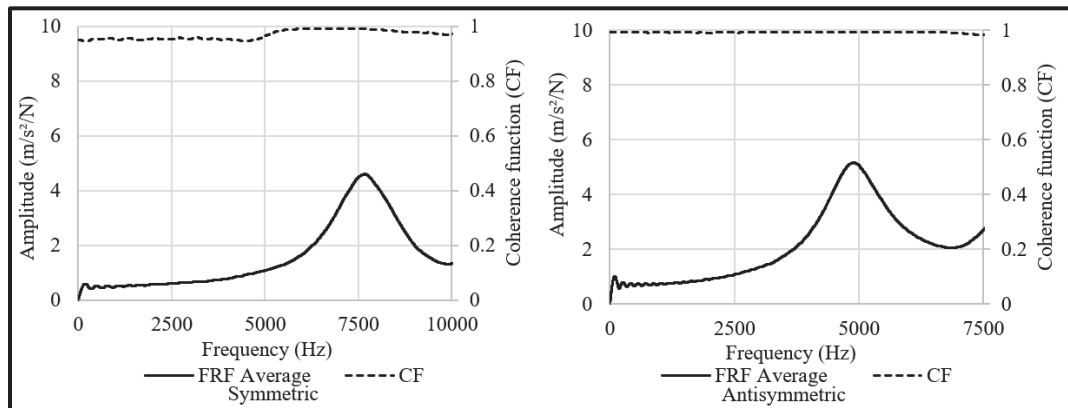


Figure-A IV-7 FRF and CF for EG-10-G4-D-200G-05-T at 23 °C

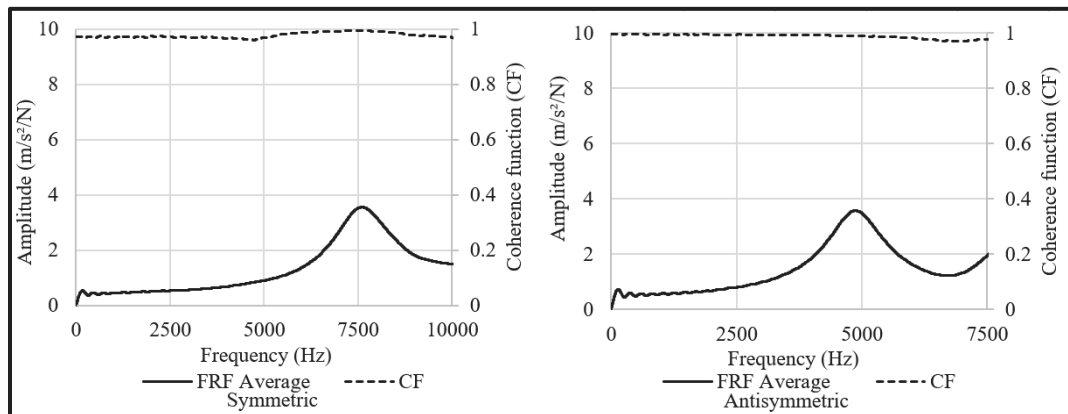


Figure-A IV-8 FRF and CF for EG-10-G4-D-200G-05-B at 23 °C

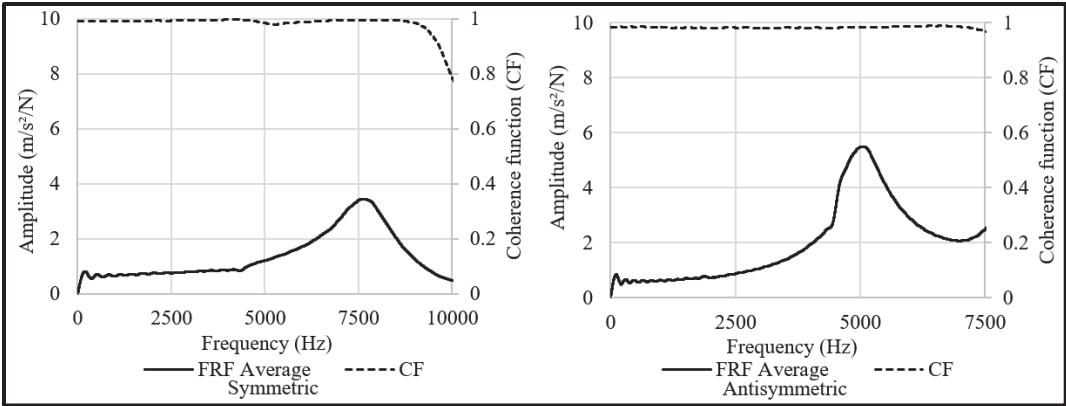


Figure-A IV-9 FRF and CF for EG-10-G4-D-200G-08-T at 23 °C

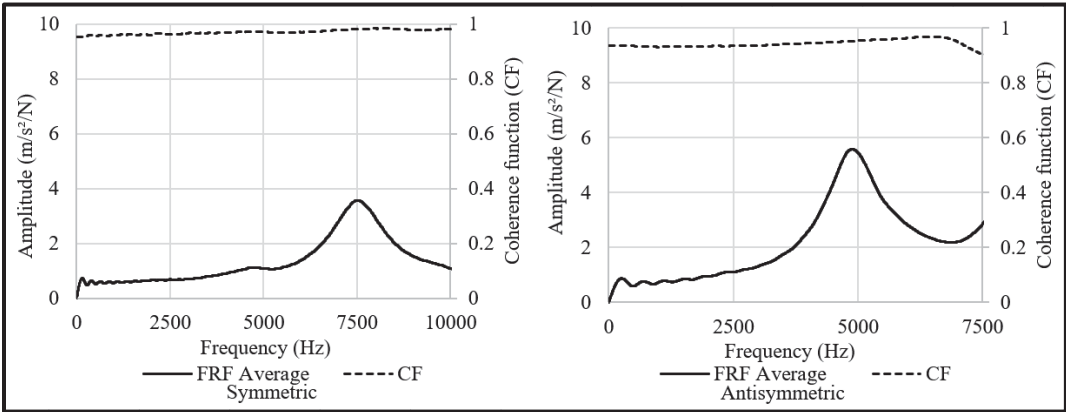


Figure-A IV-10 FRF and CF for EG-10-G4-D-200G-08-B at 23 °C

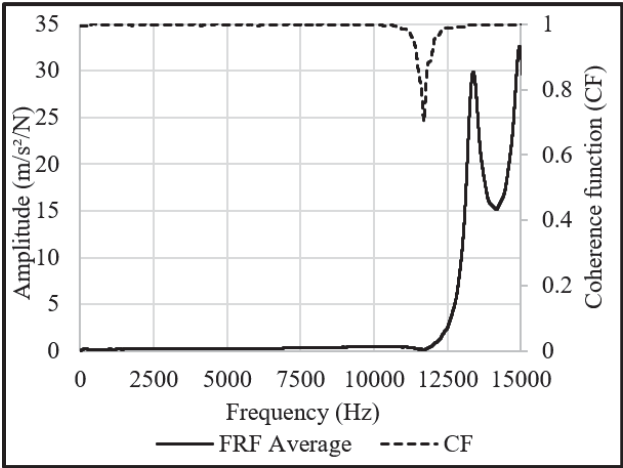


Figure-A IV-11 FRF and CF for EG-10-G4-S-200G-03 at -20 °C

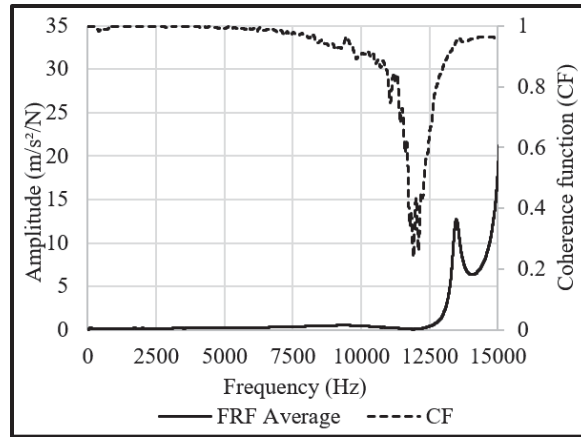


Figure-A IV-12 FRF and CF for EG-10-G4-S-200G-04 at -20 °C

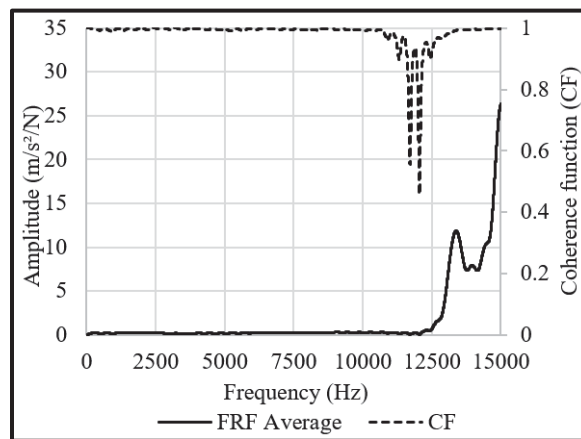


Figure-A IV-13 FRF and CF for EG-10-G4-S-200G-05 at -20 °C

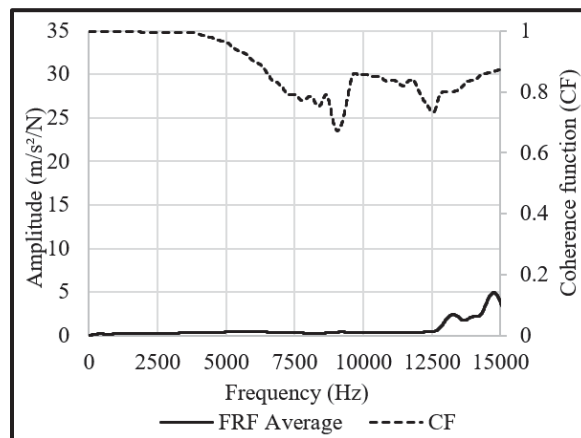


Figure-A IV-14 FRF and CF for EG-10-G4-S-200G-08 at -20 °C

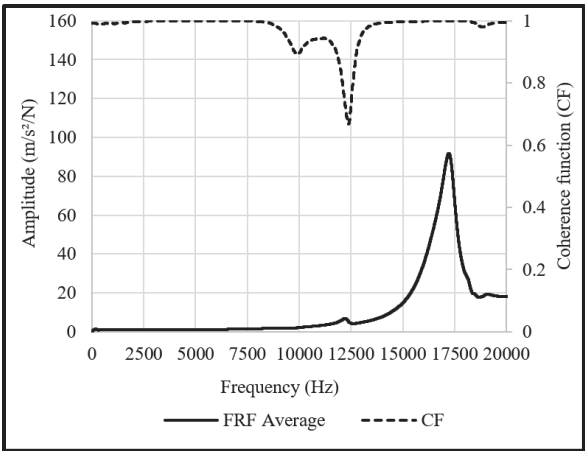


Figure-A IV-15 FRF and CF for EG-10-G4-C-200G-03 at -20 °C

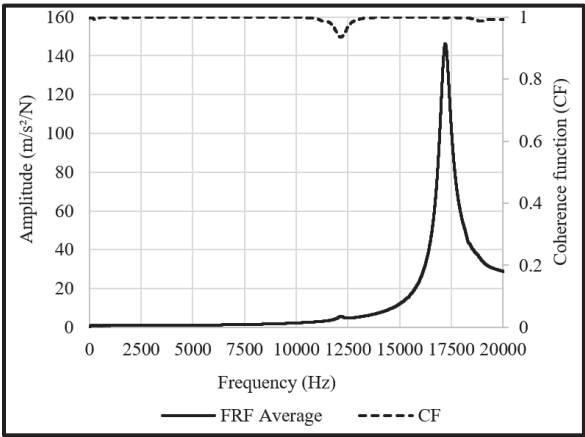


Figure-A IV-16 FRF and CF for EG-10-G4-C-200G-04 at -20 °C

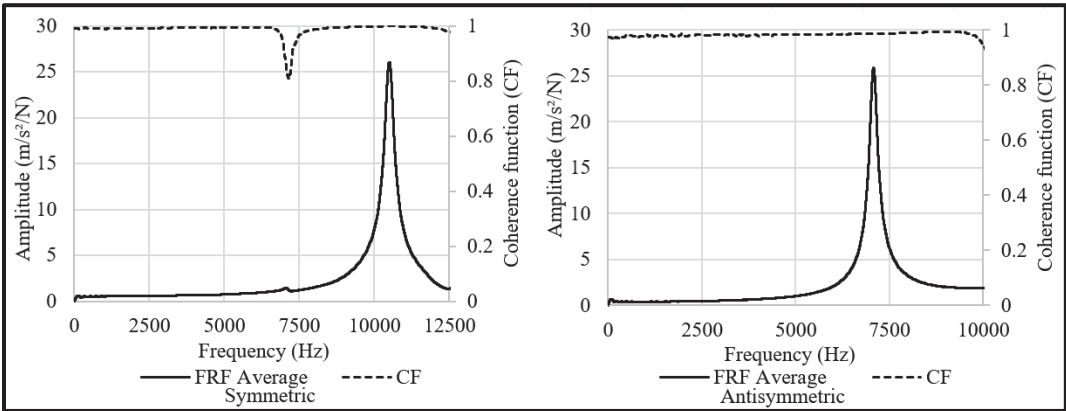


Figure-A IV-17 FRF and CF for EG-10-G4-D-200G-05-T at -20 °C

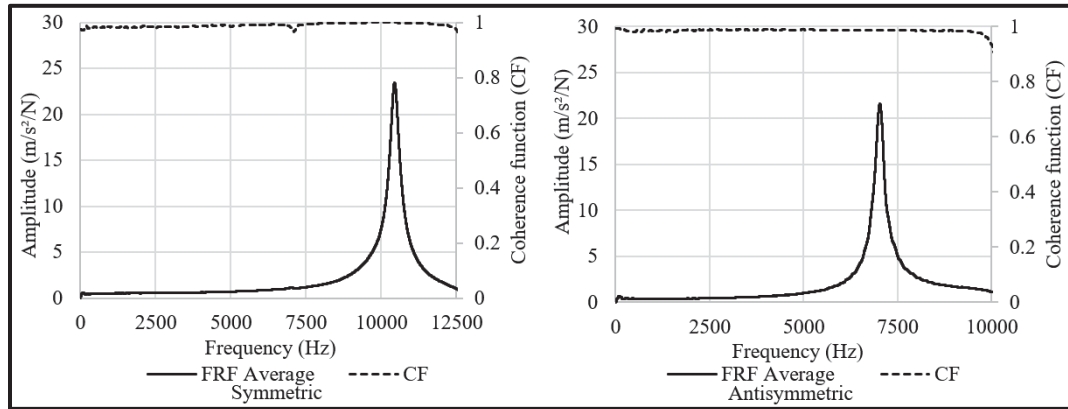


Figure-A IV-18 FRF and CF for EG-10-G4-D-200G-05-B at -20 °C

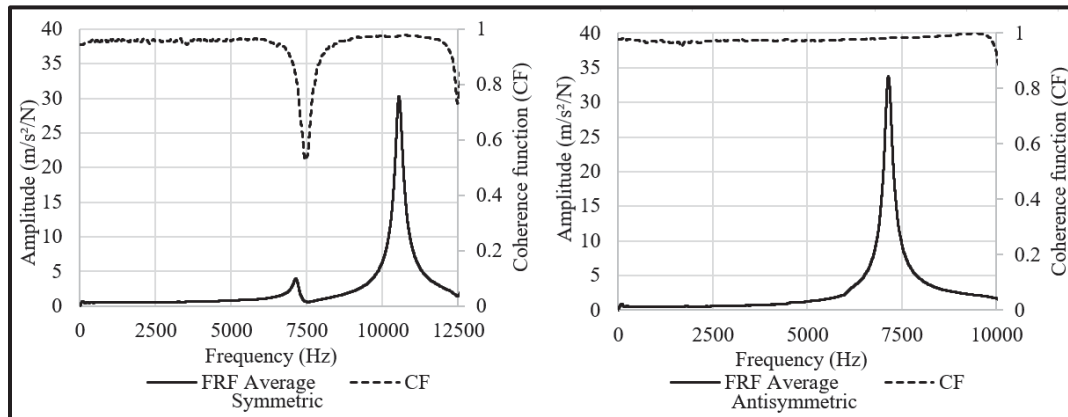


Figure-A IV-19 FRF and CF for EG-10-G4-D-200G-08-T at -20 °C

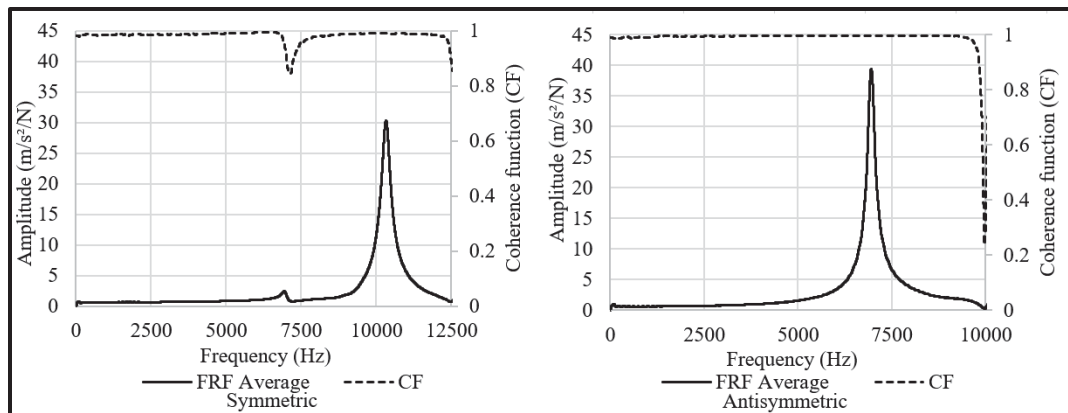


Figure-A IV-20 FRF and CF for EG-10-G4-D-200G-08-B at -20 °C

APPENDIX V

FRF AND CF FOR OBJECTIVE 3

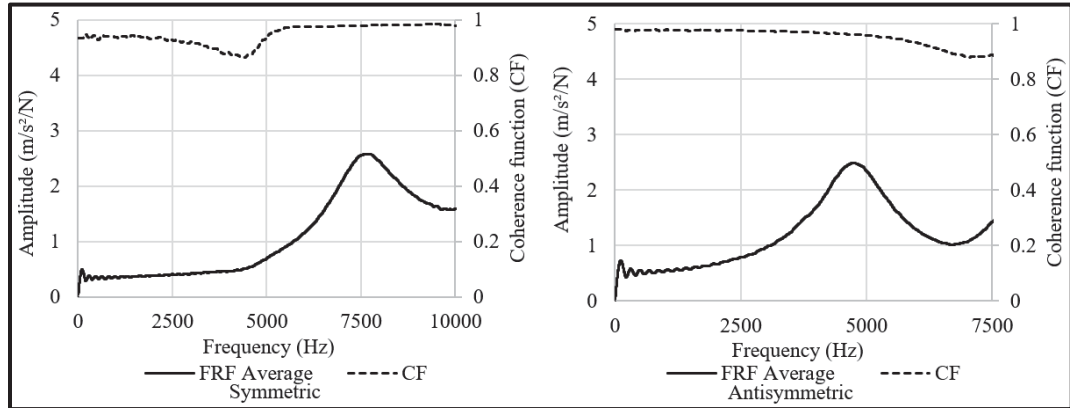


Figure-A V-1 FRF and CF for ESG-10-G1-D-200G-T at 23 °C

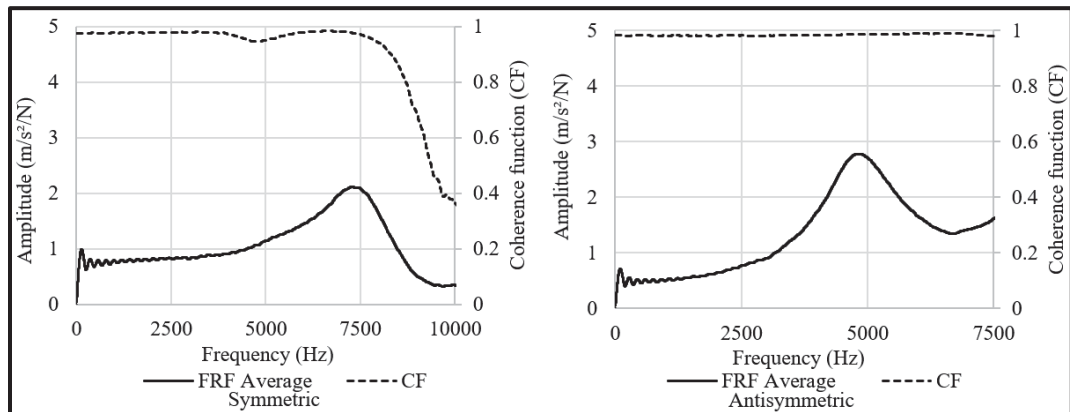


Figure-A V-2 FRF and CF for ESG-10-G1-D-200G-B at 23 °C

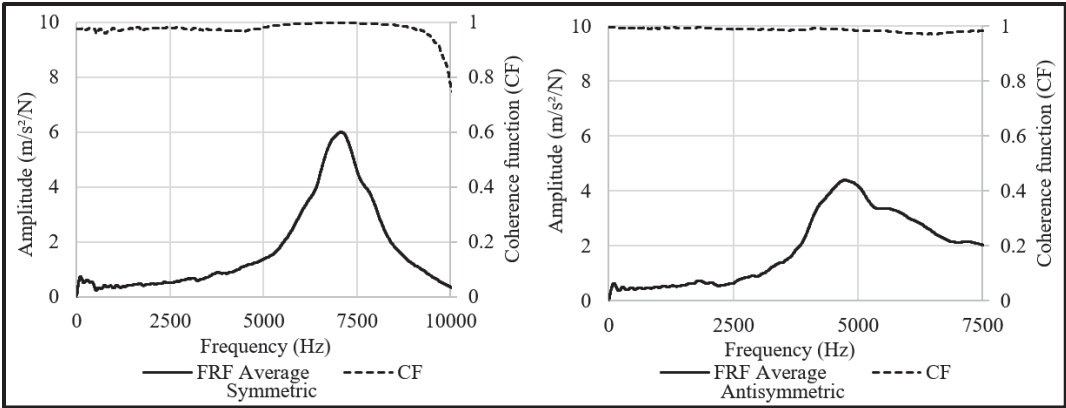


Figure-A V-3 FRF and CF for ESG-10-G1-D-80G-01-T at 23 °C

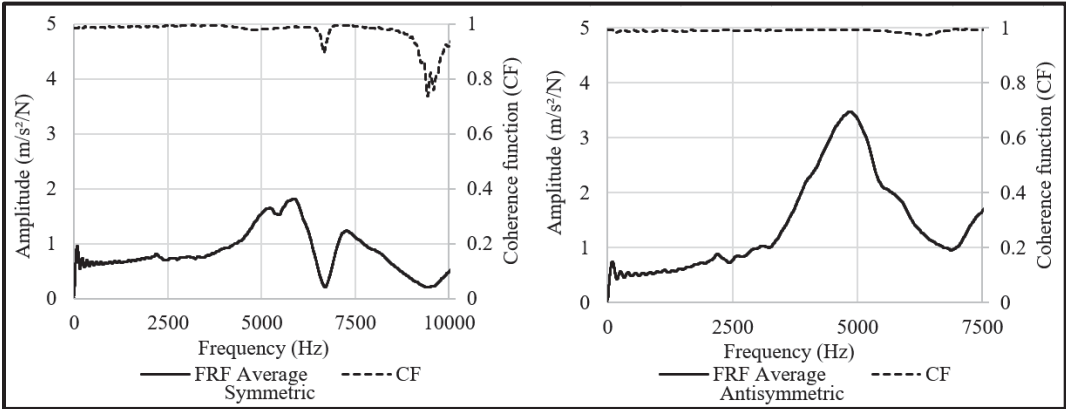


Figure-A V-4 FRF and CF for ESG-10-G1-D-80G-01-B at 23 °C

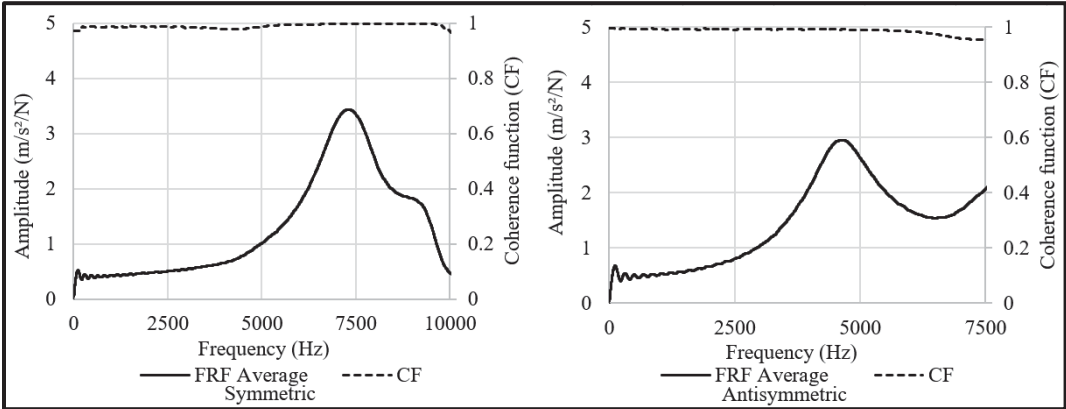


Figure-A V-5 FRF and CF for ESG-10-G1-D-80G-02-T at 23 °C

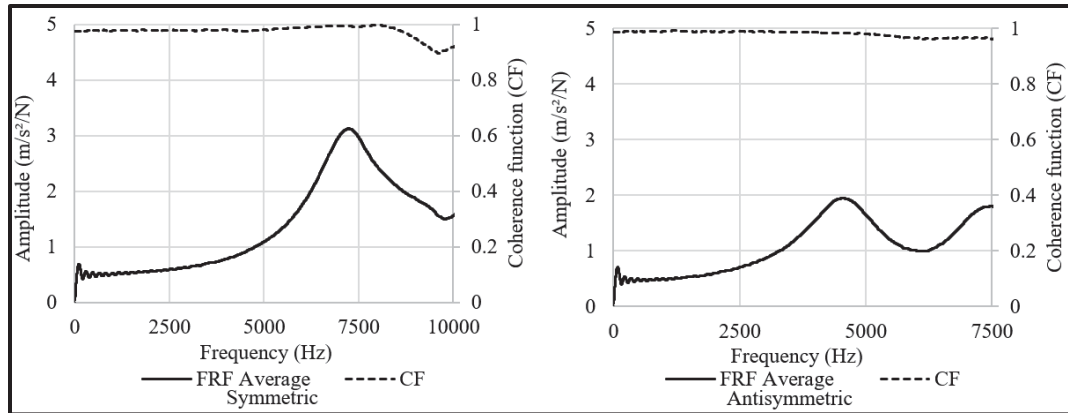


Figure-A V-6 FRF and CF for ESG-10-G1-D-80G-02-B at 23 °C

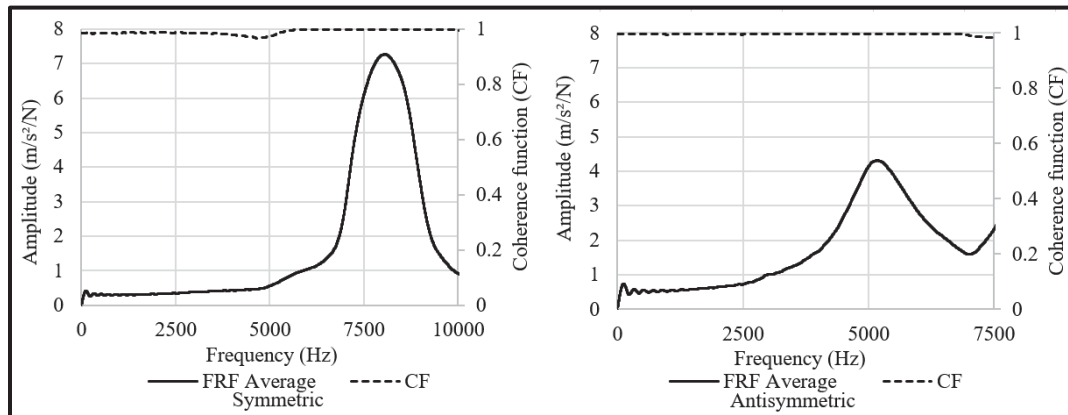


Figure-A V-7 FRF and CF for ESG-10-G1-D-80G-03-T at 23 °C

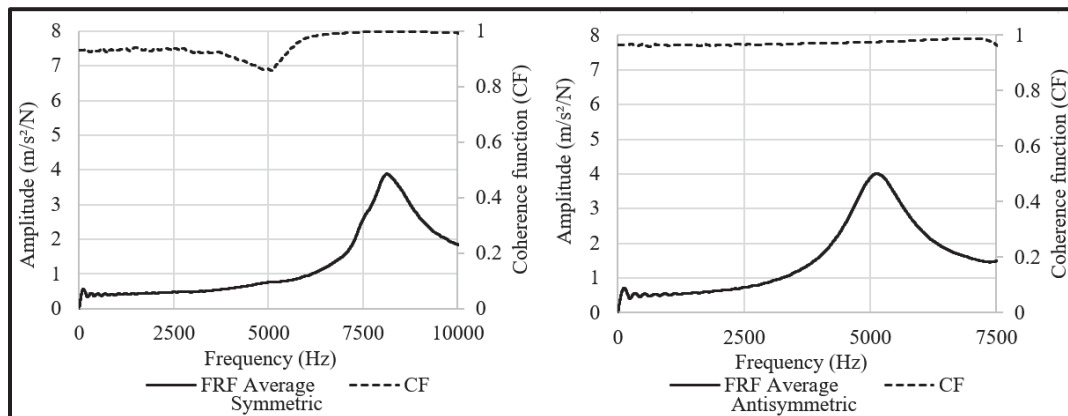


Figure-A V-8 FRF and CF for ESG-10-G1-D-80G-03-B at 23 °C

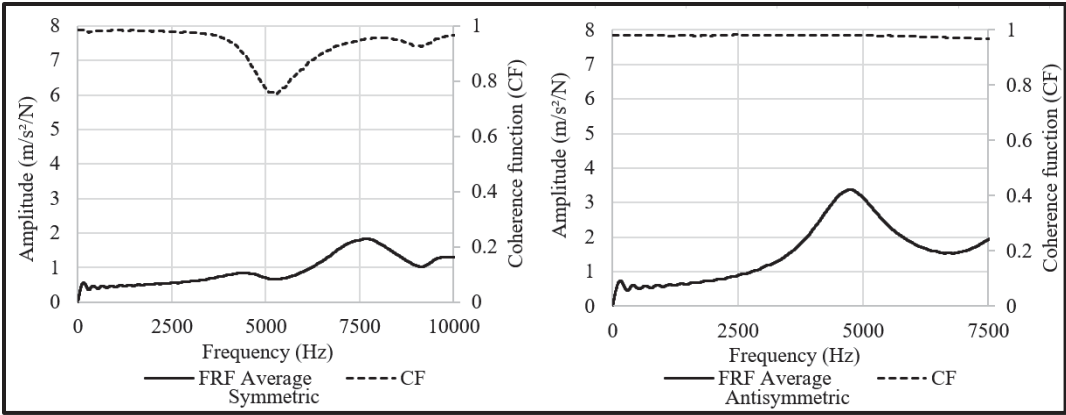


Figure-A V-9 FRF and CF for ESG-10-G2-D-80G-01-T at 23 °C

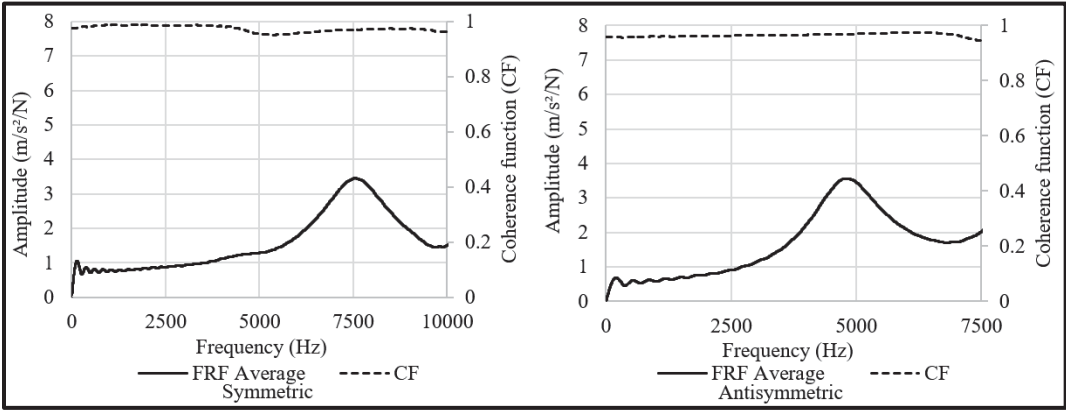


Figure-A V-10 FRF and CF for ESG-10-G2-D-80G-01-B at 23 °C

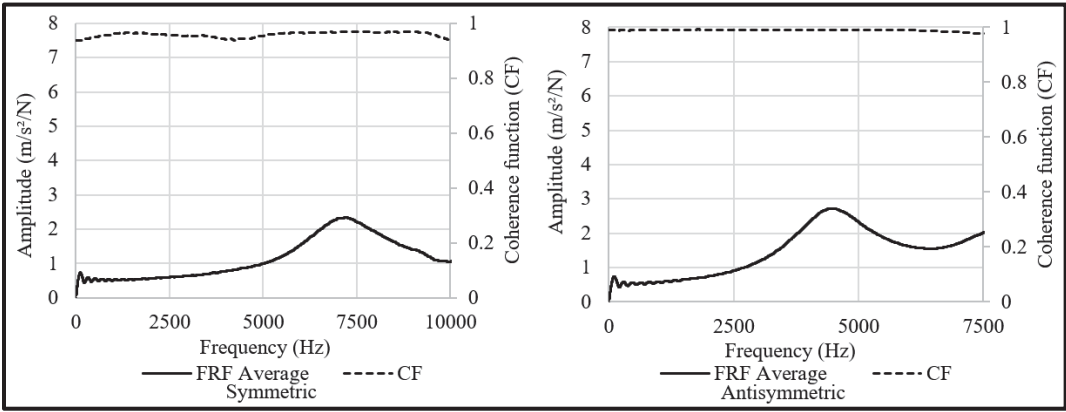


Figure-A V-11 FRF and CF for ESG-10-G2-D-80G-02-T at 23 °C

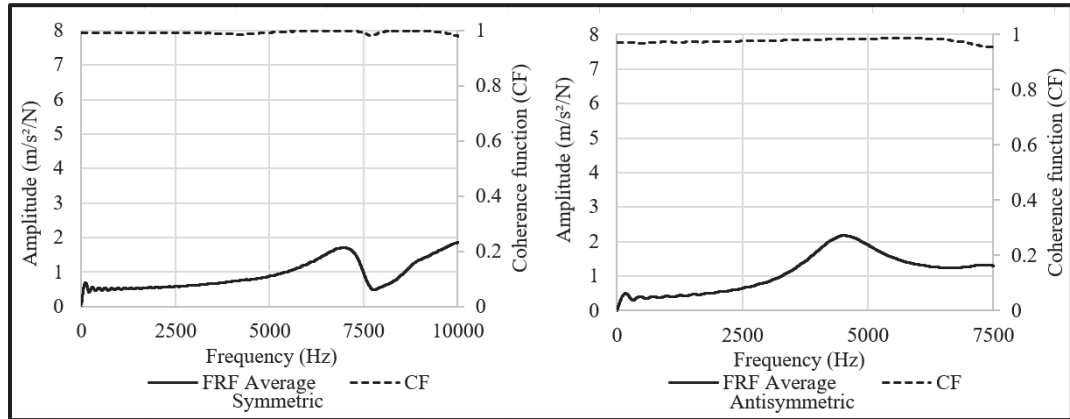


Figure-A V-12 FRF and CF for ESG-10-G2-D-80G-02-B at 23 °C

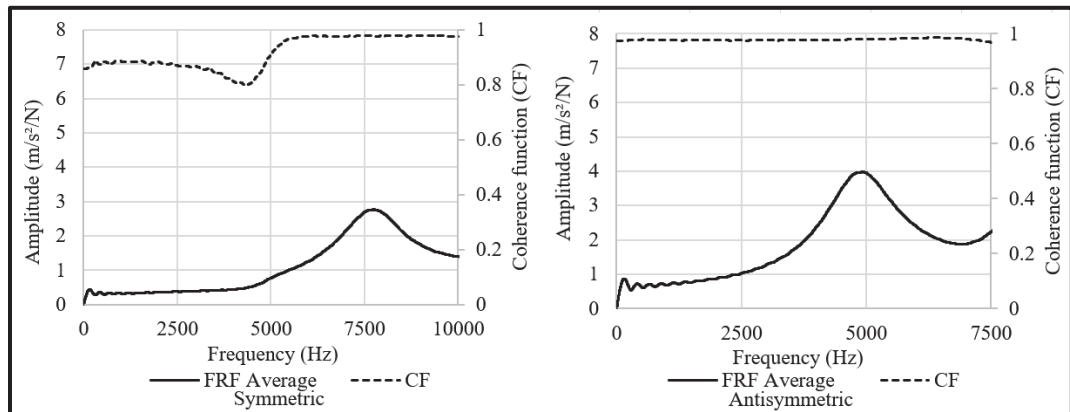


Figure-A V-13 FRF and CF for ESG-10-G2-D-80G-03-T at 23 °C

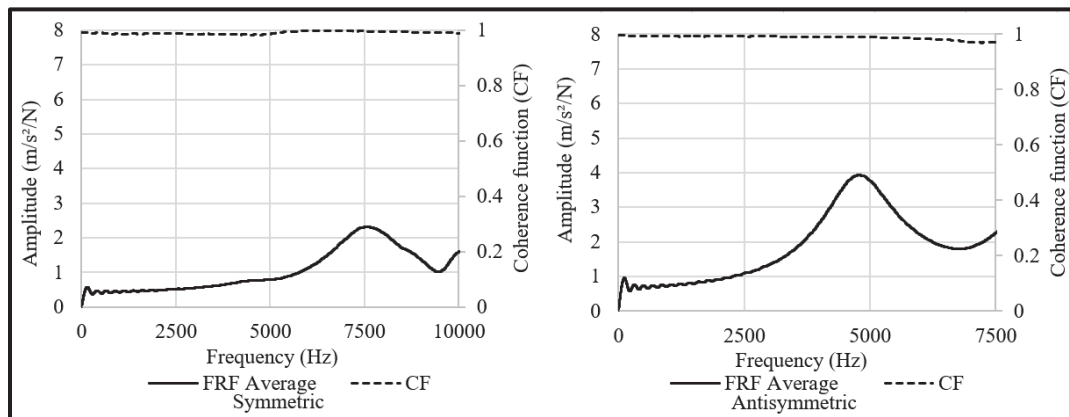


Figure-A V-14 FRF and CF for ESG-10-G2-D-80G-03-B at 23 °C

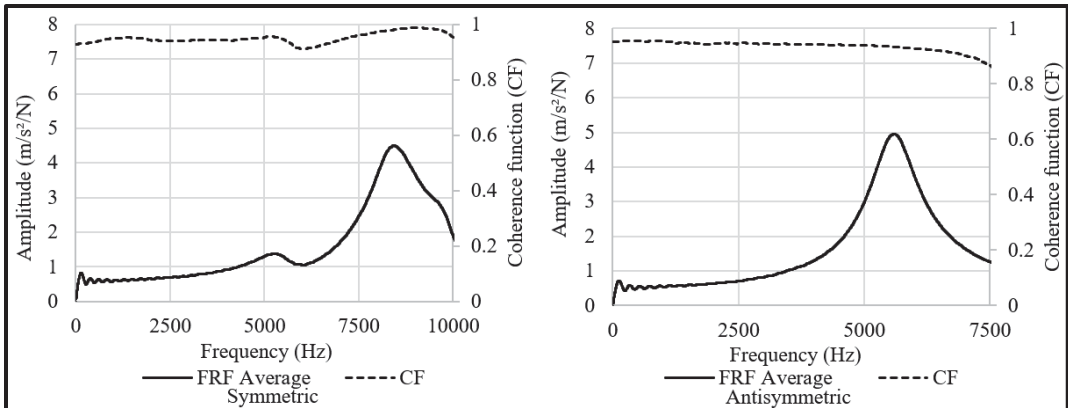


Figure-A V-15 FRF and CF for ESG-10-G2-D-200G-T at 23 °C

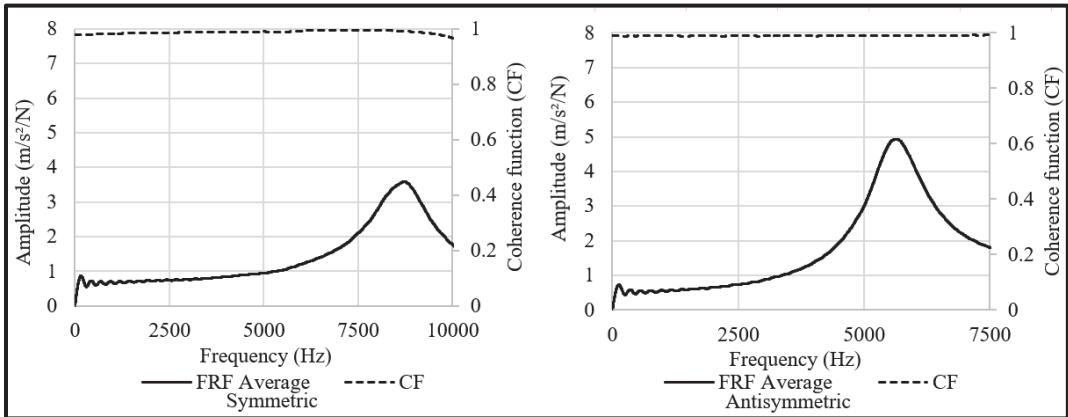


Figure-A V-16 FRF and CF for ESG-10-G2-D-200G-B at 23 °C

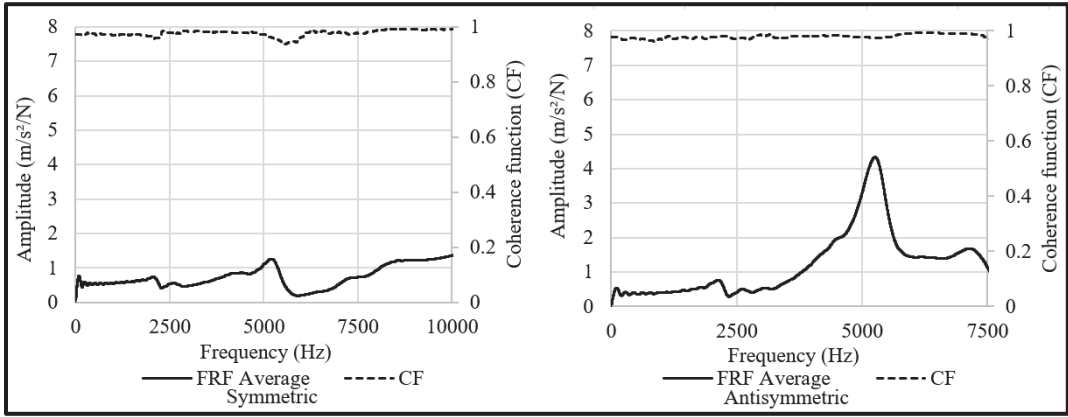


Figure-A V-17 FRF and CF for ESG-10-G3-D-200G-T at 23 °C

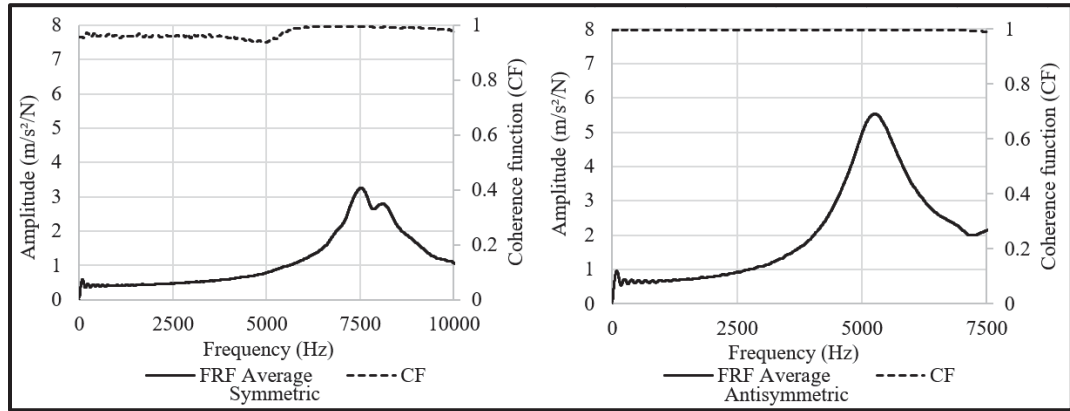


Figure-A V-18 FRF and CF for ESG-10-G3-D-200G-B at 23 °C

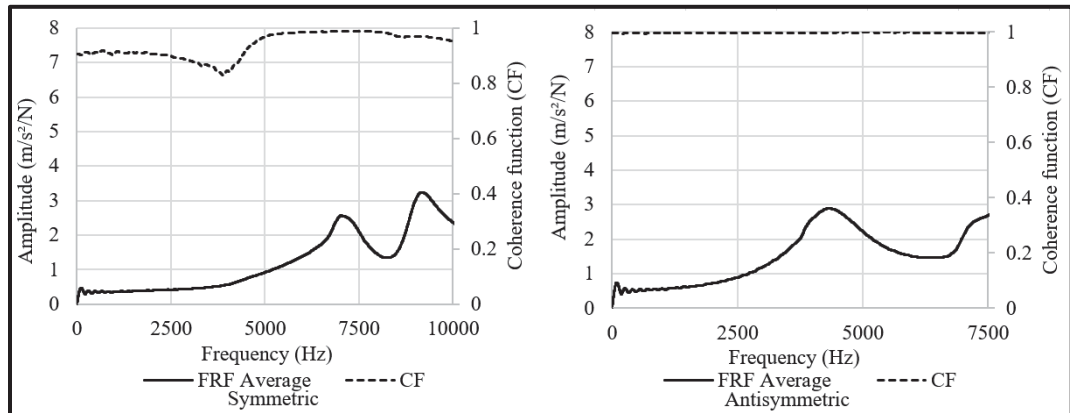


Figure-A V-19 FRF and CF for ESG-10-G3-D-80G-01-T at 23 °C

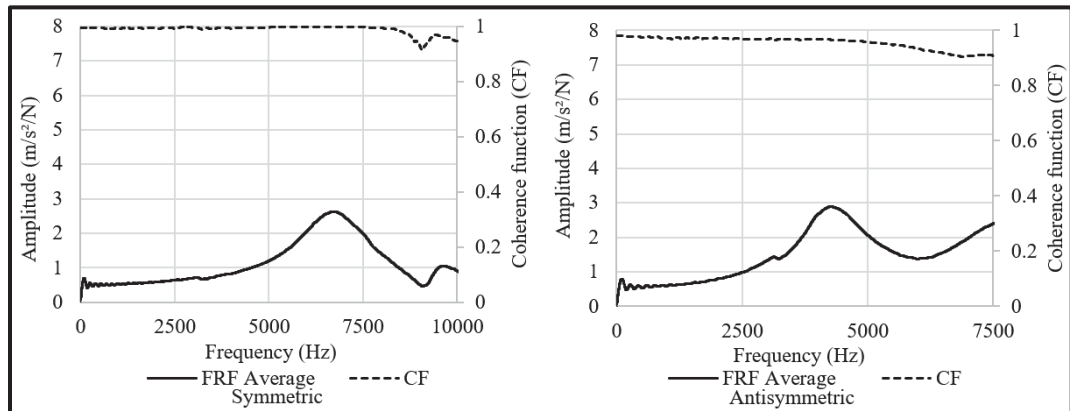


Figure-A V-20 FRF and CF for ESG-10-G3-D-80G-01-B at 23 °C

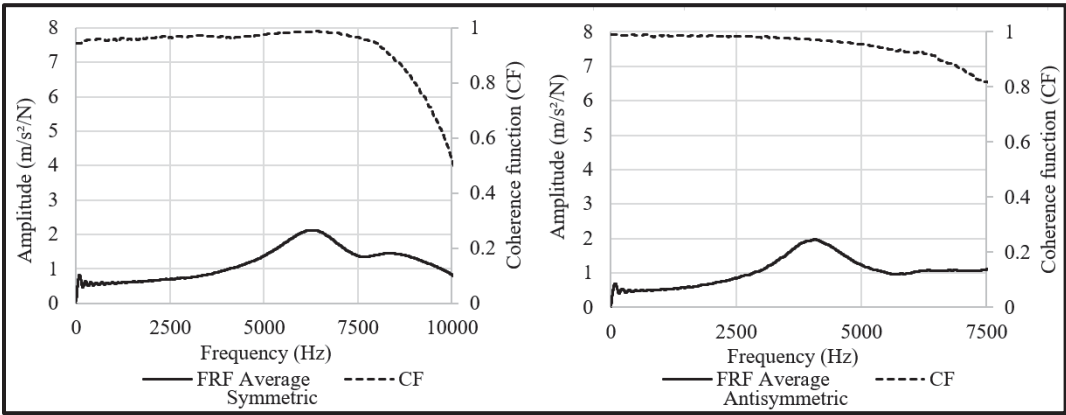


Figure-A V-21 FRF and CF for ESG-10-G3-D-80G-02-T at 23 °C

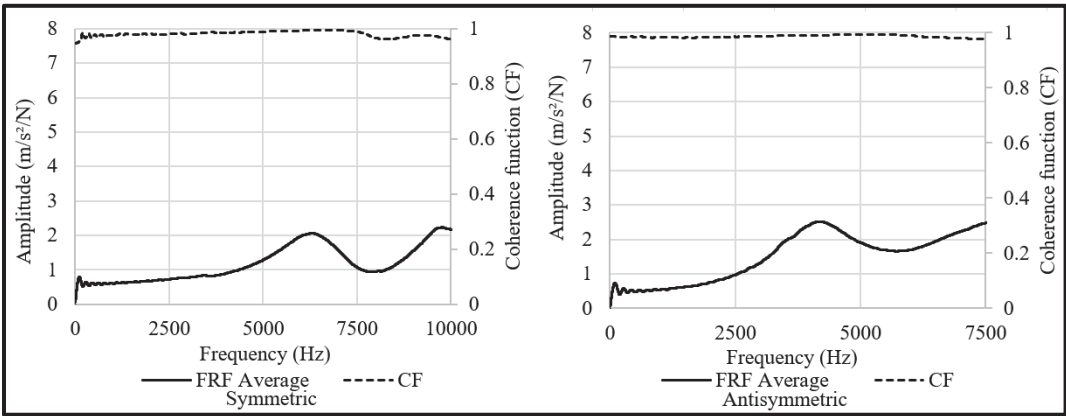


Figure-A V-22 FRF and CF for ESG-10-G3-D-80G-02-B at 23 °C

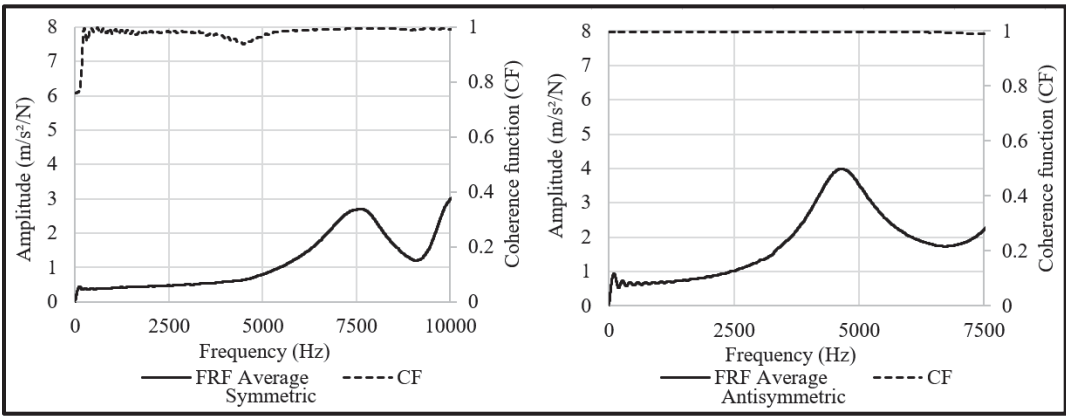


Figure-A V-23 FRF and CF for ESG-10-G3-D-80G-03-T at 23 °C

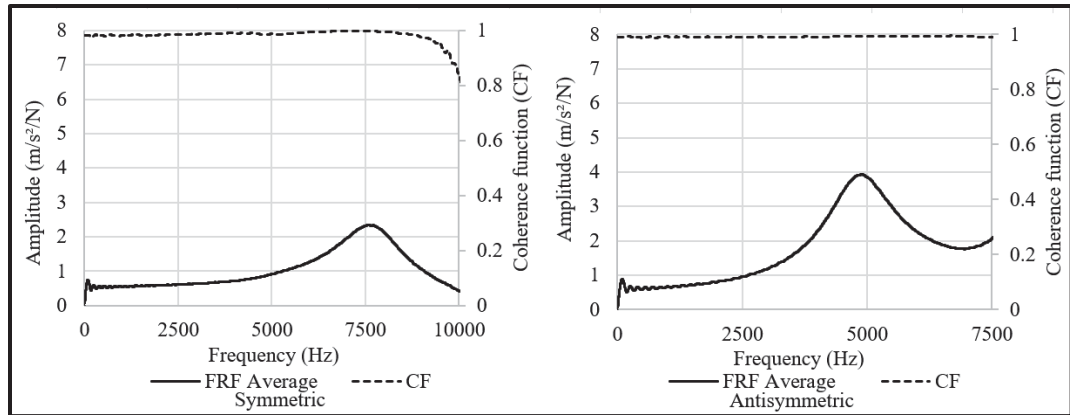


Figure-A V-24 FRF and CF for ESG-10-G3-D-80G-03-B at 23 °C

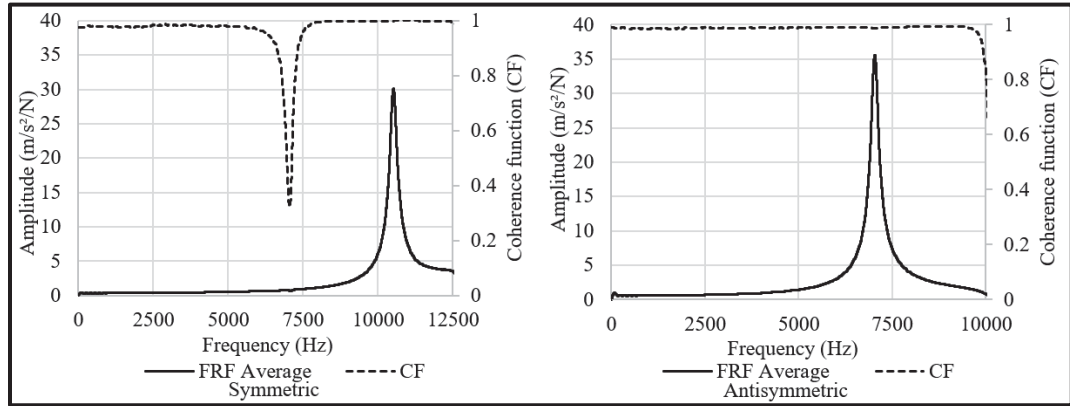


Figure-A V-25 FRF and CF for ESG-10-G1-D-200G-T at -20 °C

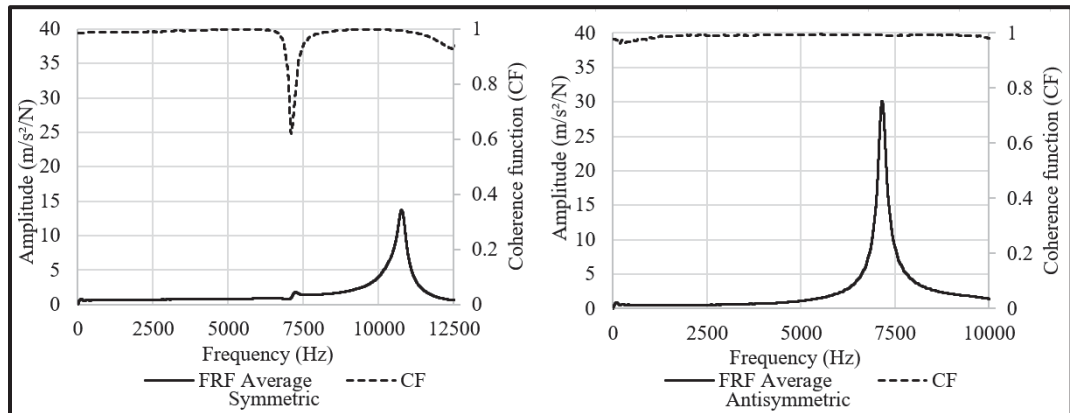


Figure-A V-26 FRF and CF for ESG-10-G1-D-200G-B at -20 °C

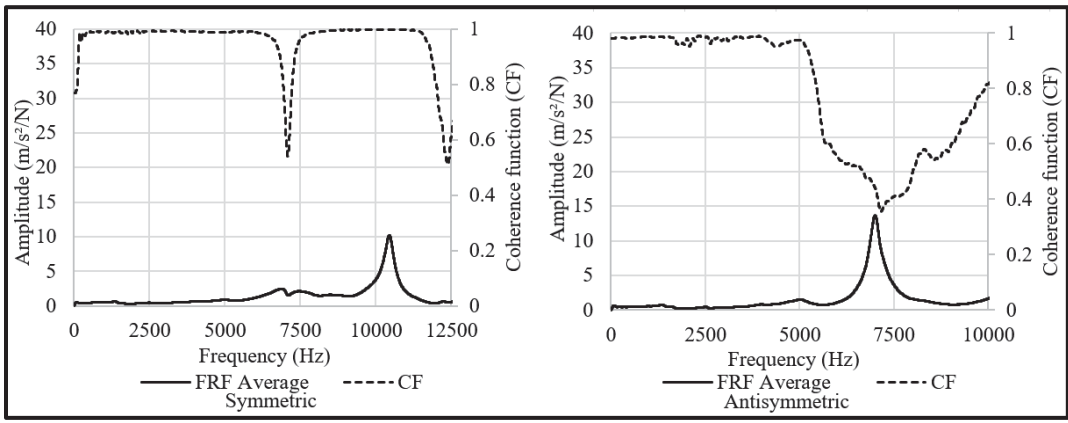


Figure-A V-27 FRF and CF for ESG-10-G1-D-80G-01-T at -20 °C

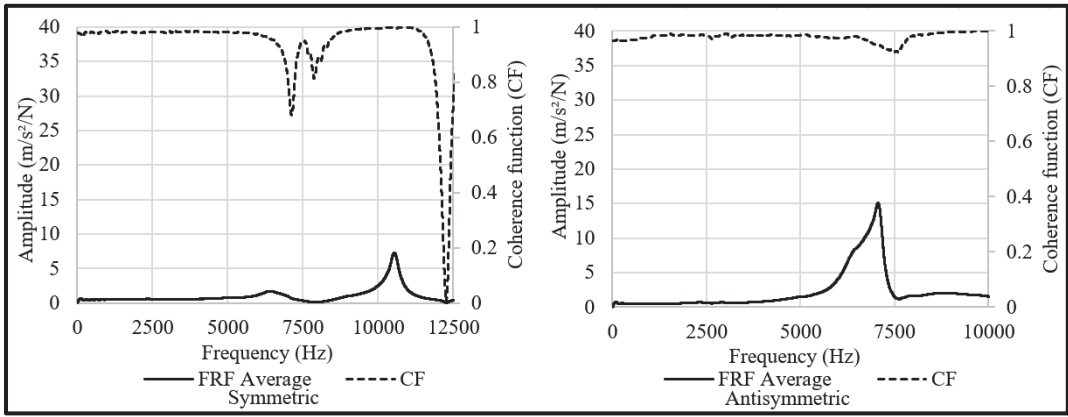


Figure-A V-28 FRF and CF for ESG-10-G1-D-80G-01-B at -20 °C

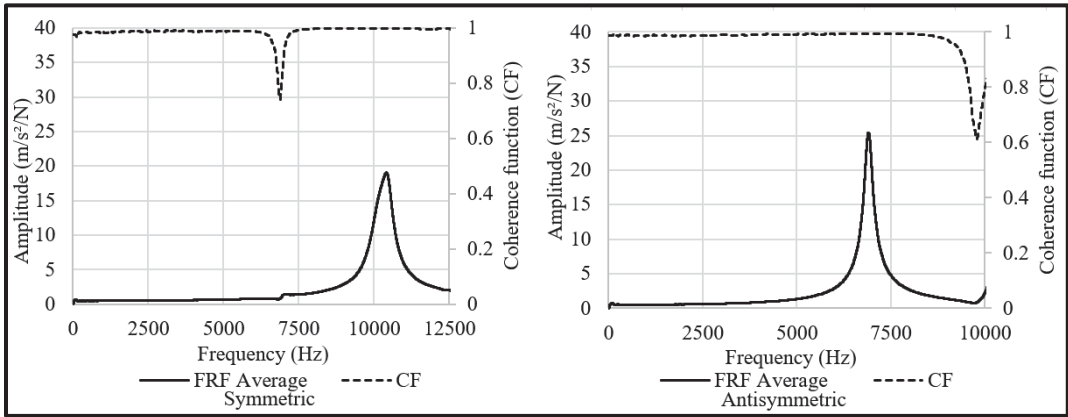
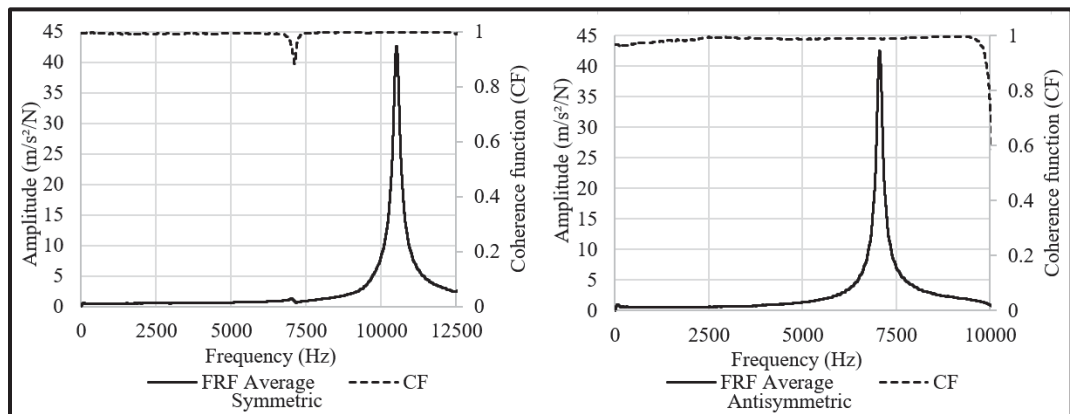
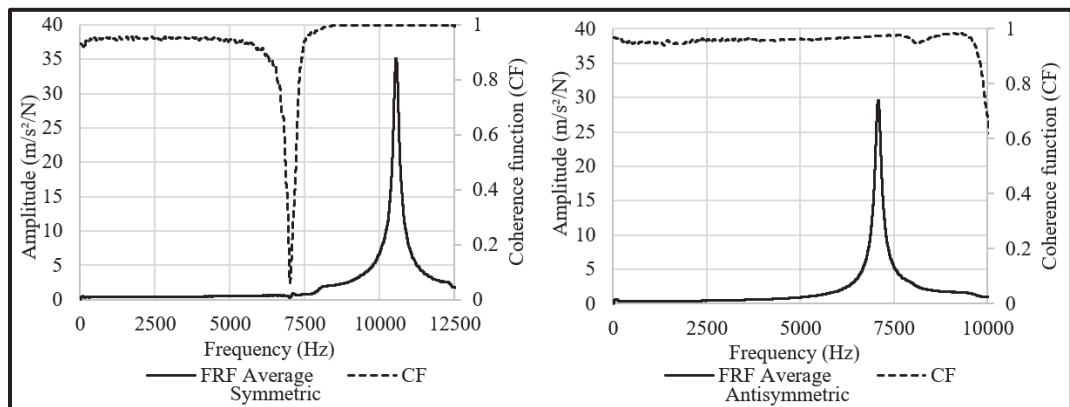
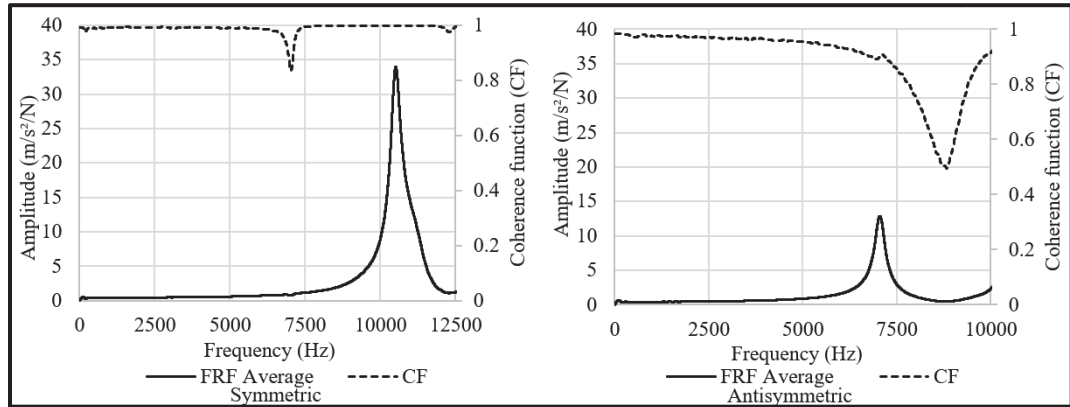


Figure-A V-29 FRF and CF for ESG-10-G1-D-80G-02-T at -20 °C



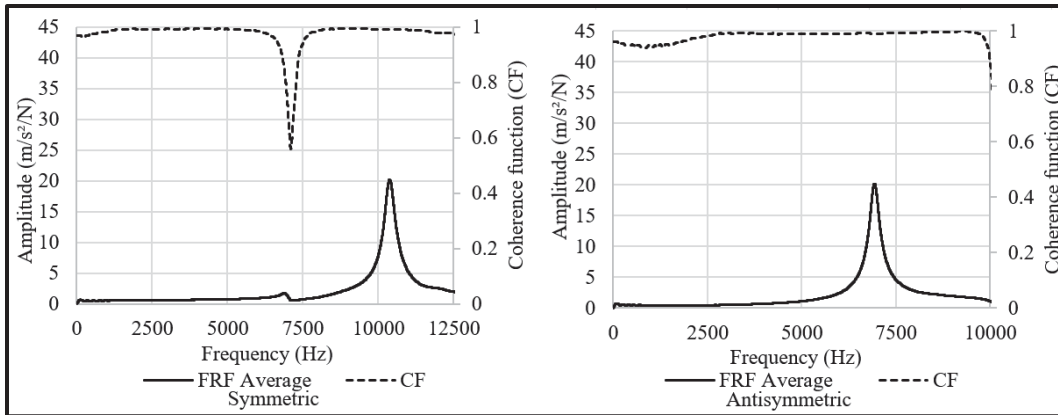


Figure-A V-33 FRF and CF for ESG-10-G2-D-80G-01-T at -20 °C

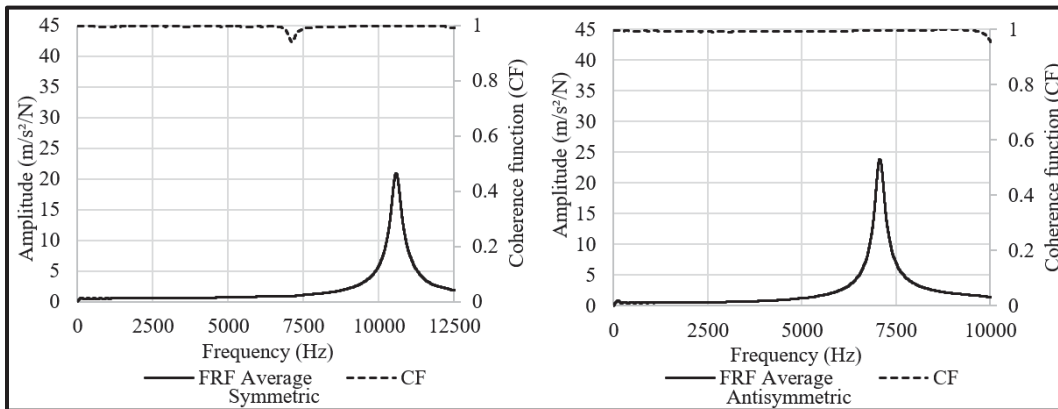


Figure-A V-34 FRF and CF for ESG-10-G2-D-80G-01-B at -20 °C

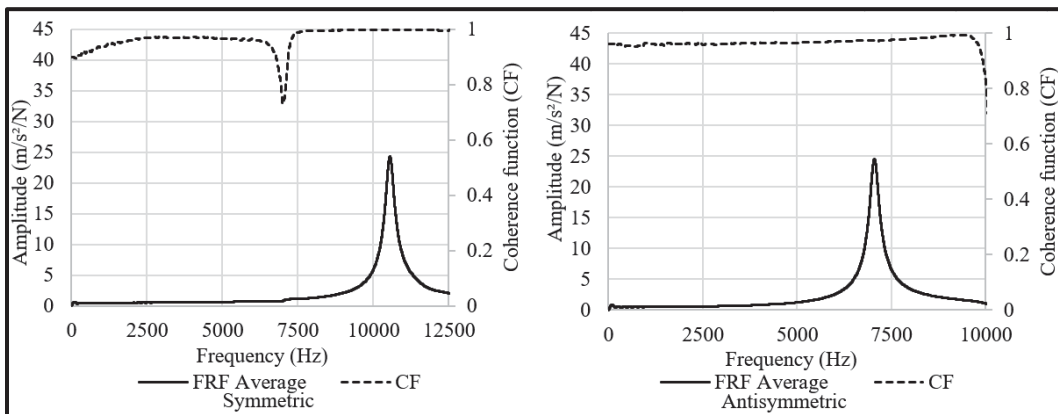


Figure-A V-35 FRF and CF for ESG-10-G2-D-80G-02-T at -20 °C

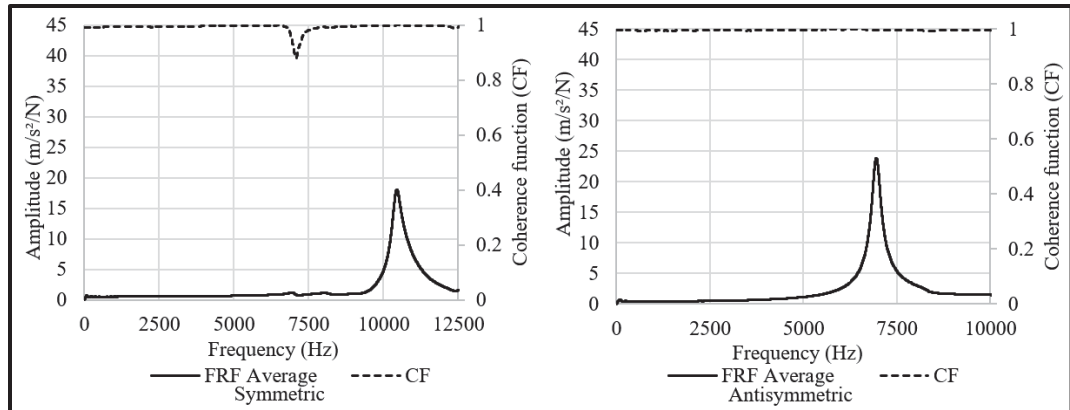


Figure-A V-36 FRF and CF for ESG-10-G2-D-80G-02-B at -20 °C

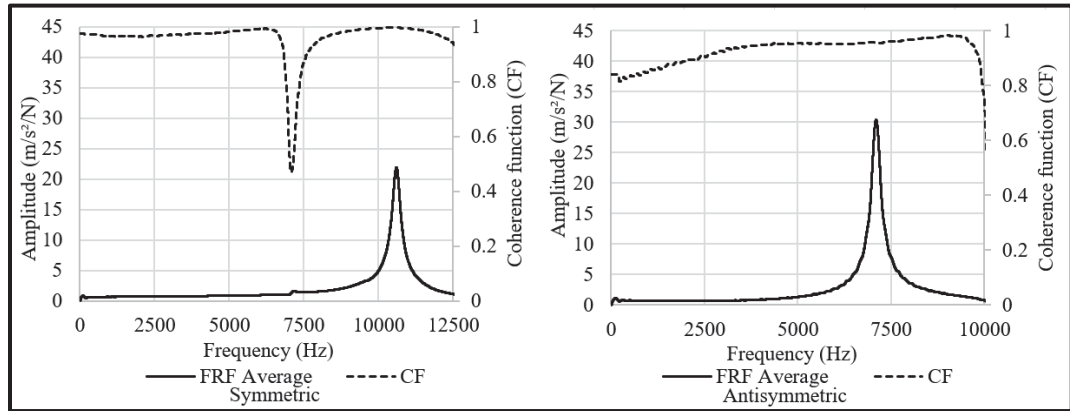


Figure-A V-37 FRF and CF for ESG-10-G2-D-80G-03-T at -20 °C

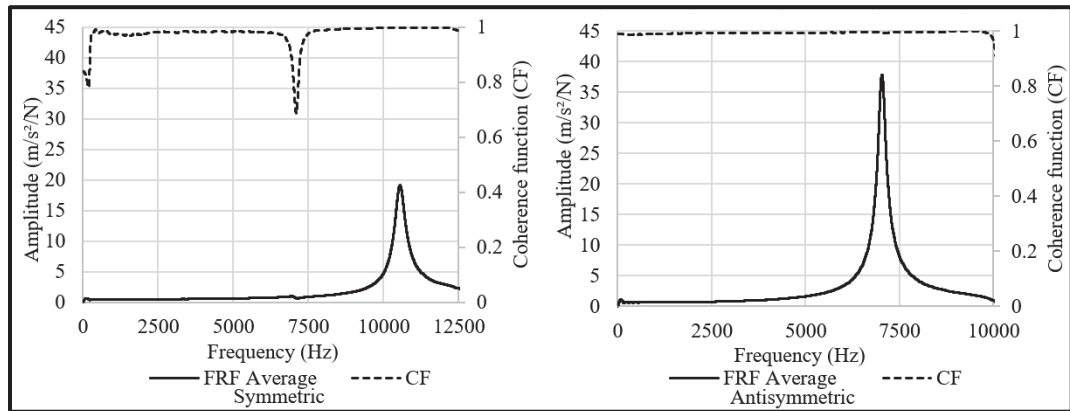


Figure-A V-38 FRF and CF for ESG-10-G2-D-80G-03-B at -20 °C

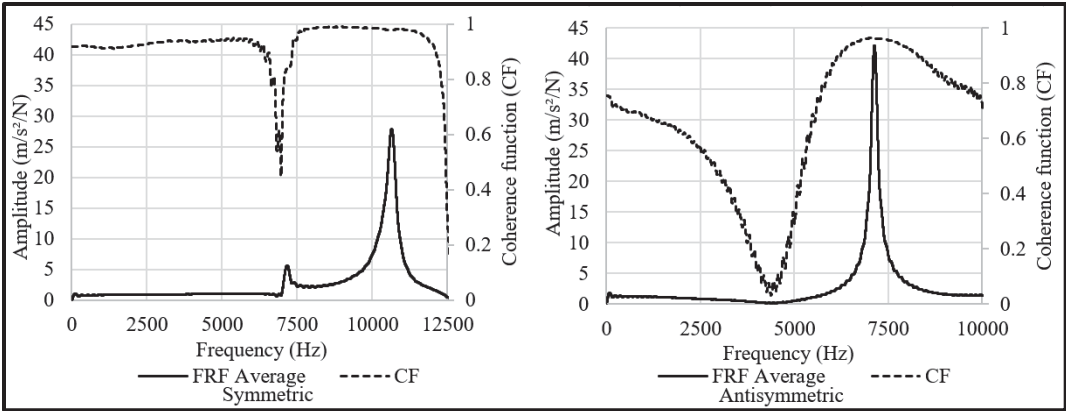


Figure-A V-39 FRF and CF for ESG-10-G2-D-200G-T at -20 °C

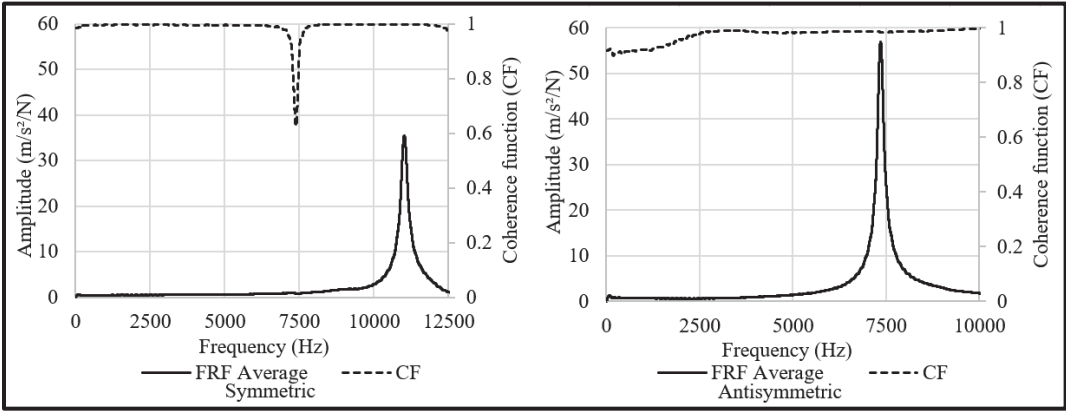


Figure-A V-40 FRF and CF for ESG-10-G2-D-200G-B at -20 °C

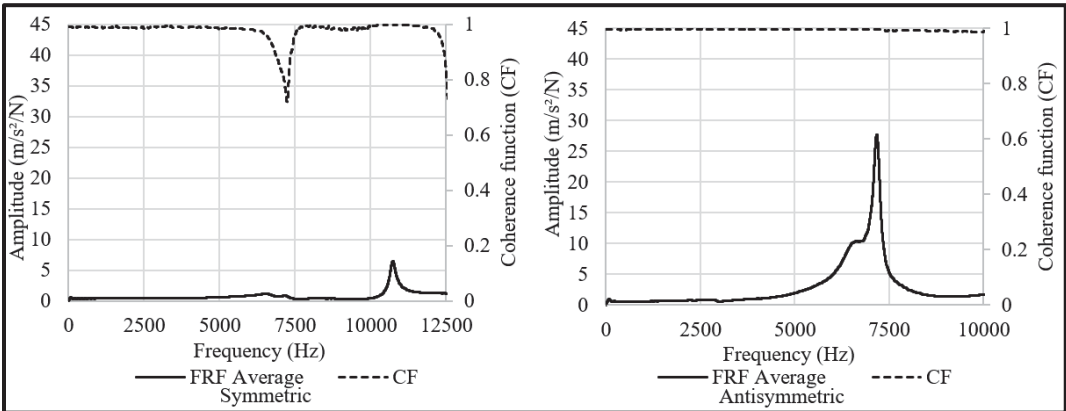


Figure-A V-41 FRF and CF for ESG-10-G3-D-200G-T at -20 °C

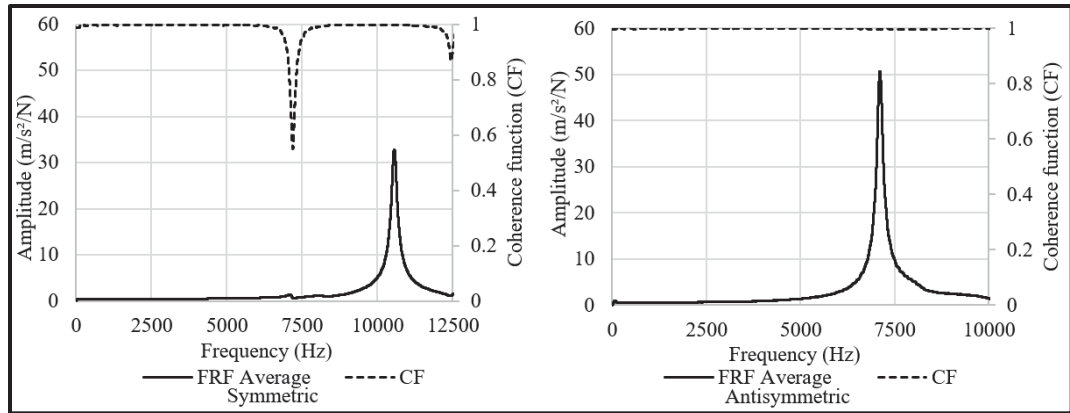


Figure-A V-42 FRF and CF for ESG-10-G3-D-200G-B at -20 °C

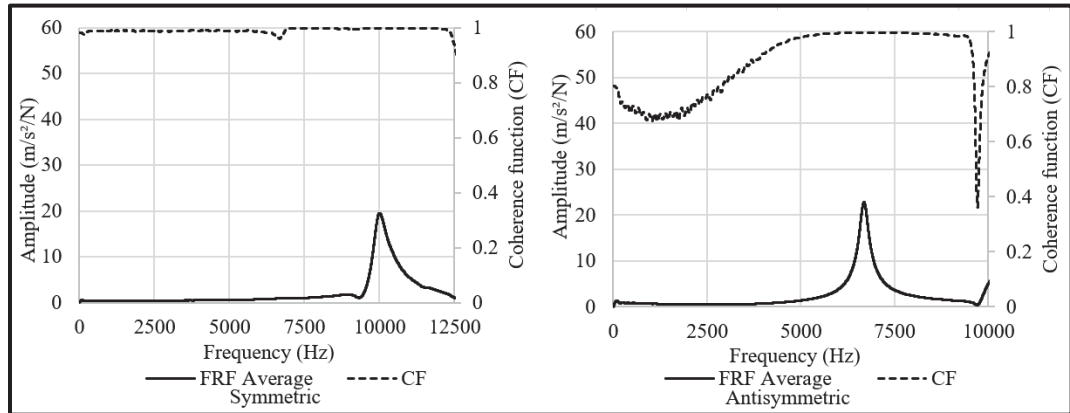


Figure-A V-43 FRF and CF for ESG-10-G3-D-80G-01-T at -20 °C

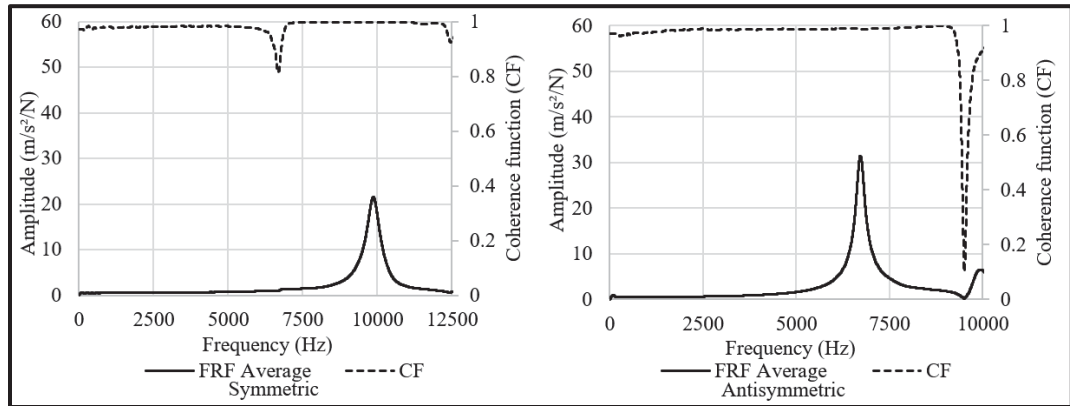
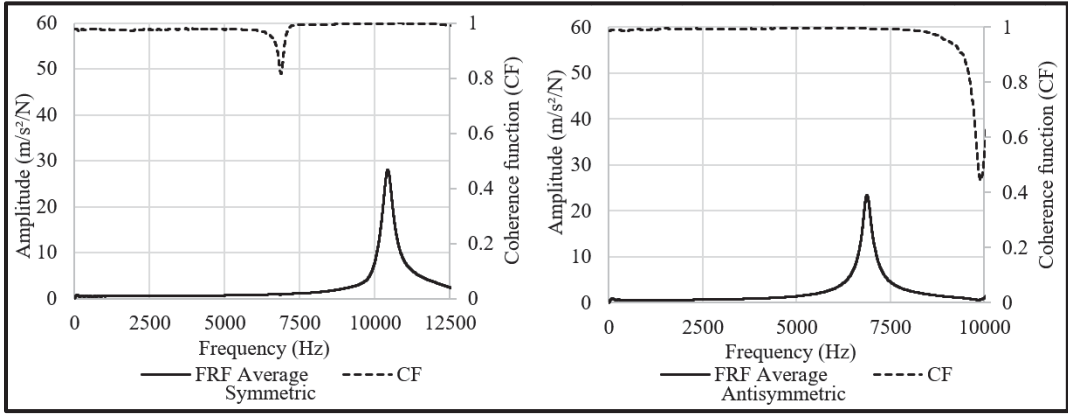
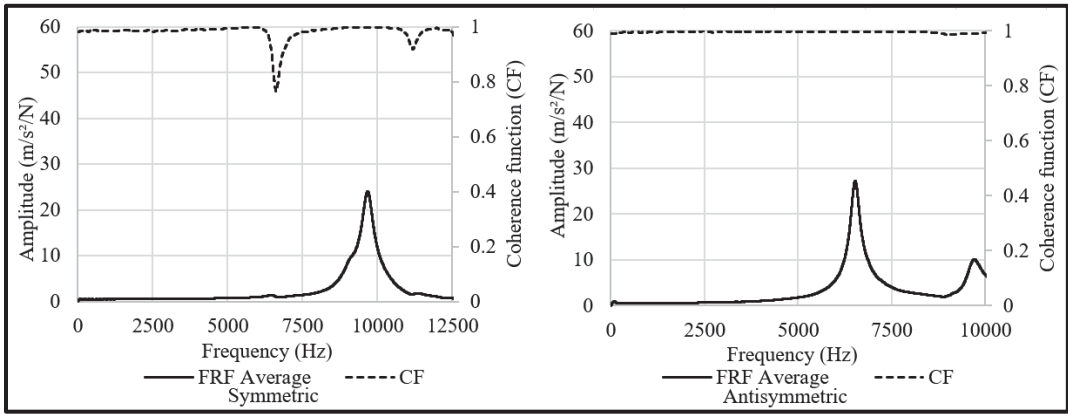
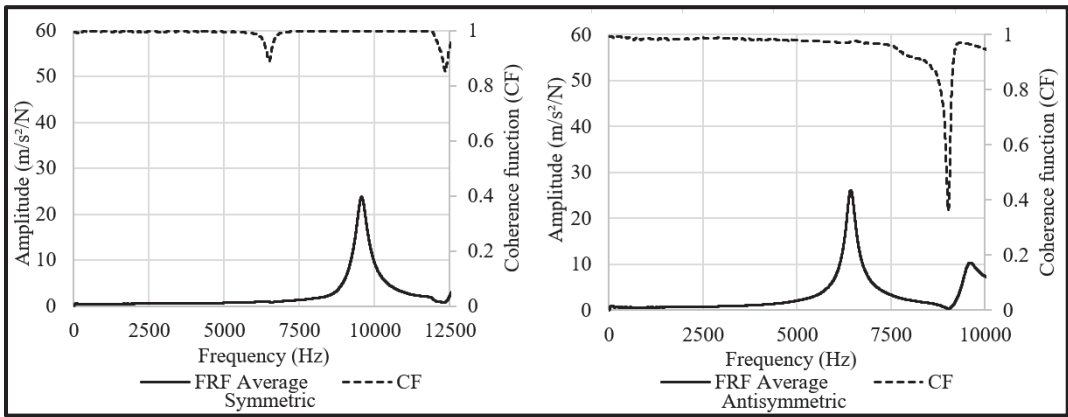


Figure-A V-44 FRF and CF for ESG-10-G3-D-80G-01-B at -20 °C



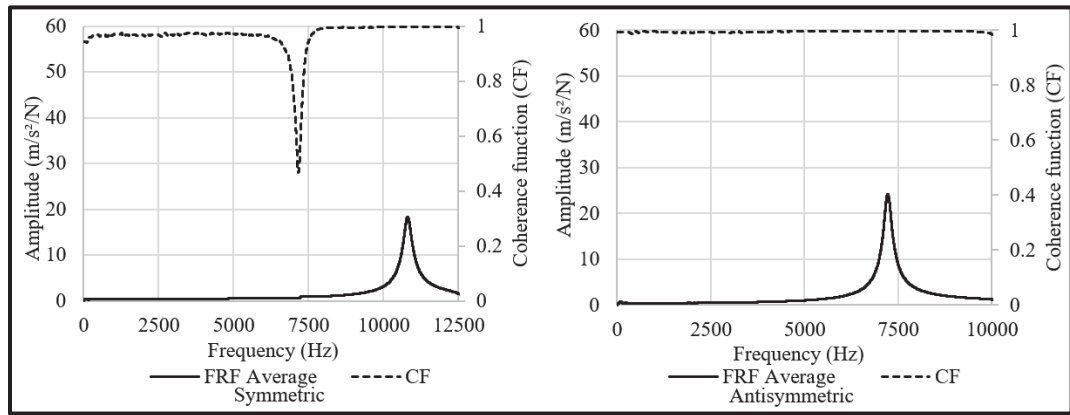


Figure-A V-48 FRF and CF for ESG-10-G3-D-80G-03-B at -20 °C

LIST OF BIBLIOGRAPHICAL REFERENCES

- Aakif Ishaq, M., & Giustozzi, F. (2022). Correlation between rheological tests on bitumen and asphalt low temperature cracking tests. *Construction and Building Materials*, 320, 126109. <https://doi.org/10.1016/j.conbuildmat.2021.126109>
- Al-Khateeb, G. G., Ghuzlan, K. A., & Al-Barqawi, M. O. (2017). Effect of Superpave restricted zone on volumetric and compaction properties of asphalt mixtures. *International Journal of Pavement Research and Technology*, 10(6), 488–496. <https://doi.org/10.1016/j.ijprt.2017.03.004>
- Arambula, E., Masad, E., & Martin, A. E. (2007). Influence of Air Void Distribution on the Moisture Susceptibility of Asphalt Mixes. *Journal of Materials in Civil Engineering*, 19(8), 655–664. [https://doi.org/10.1061/\(ASCE\)0899-1561\(2007\)19:8\(655\)](https://doi.org/10.1061/(ASCE)0899-1561(2007)19:8(655))
- Babadopulos, L. F. A. L., Le Guern, M., Chailleux, E., & Dreessen, S. (2011). Low temperature specifications for asphalt binders: Tests and simulation. *TRANSPORTES*, 19(2), 7. <https://doi.org/10.14295/transportes.v19i2.506>
- Basueny, A., Perraton, D., & Carter, A. (2014). Laboratory study of the effect of RAP conditioning on the mechanical properties of hot mix asphalt containing RAP. *Materials and Structures*, 47(9), 1425–1450. <https://doi.org/10.1617/s11527-013-0127-0>
- Bérubé, M.-A., Lamothe, S., Bilodeau, K., & Carter, A. (2023). Laboratory Study of the Effects of the Mixer Type and Mixing Time on the Volumetric Properties and Performance of

a HMA with 30 Percent Reclaimed Asphalt Pavement. *Materials*, 16(3), 1300.

<https://doi.org/10.3390/ma16031300>

Birgisson, B., Roque, R., & Page, G. C. (2003). Ultrasonic Pulse Wave Velocity Test for Monitoring Changes in Hot-Mix Asphalt Mixture Integrity from Exposure to Moisture. *Transportation Research Record: Journal of the Transportation Research Board*, 1832(1), 173–181. <https://doi.org/10.3141/1832-21>

Boussabnia, M. M., Perraton, D., Di Benedetto, H., Lamothe, S., & Proteau, M. (2023).

Validation of time temperature superposition principle for high modulus asphalt concrete in the linear viscoelastic and fatigue domains. *Fatigue & Fracture of Engineering Materials & Structures*, 46(1), 80–95. <https://doi.org/10.1111/ffe.13849>

Boz, I. (n.d.). *CHARACTERIZATION OF ASPHALT MIXTURES AND RAP BINDER PROPERTIES THROUGH IMPACT RESONANCE TEST*.

Boz, I., Bekiroglu, K., Solaimanian, M., Tavassoti-Kheiry, P., & Lagoa, C. (2017). Validation of Model Order Assumption and Noise Reduction Method for the Impact Resonance Testing of Asphalt Concrete. *Journal of Nondestructive Evaluation*, 36(3), 58. <https://doi.org/10.1007/s10921-017-0436-2>

Boz, I., & Solaimanian, M. (2014). *The Impact of Specimen Size and Void Content on the Impact Resonance Testing of Asphalt Concrete* (14–5176). Article 14–5176. Transportation Research Board 93rd Annual Meeting Transportation Research Board. <https://trid.trb.org/View/1289800>

- Boz, I., & Solaimanian, M. (2018). Investigating the effect of rejuvenators on low-temperature properties of recycled asphalt using impact resonance test. *International Journal of Pavement Engineering*, 19(11), 1007–1016. <https://doi.org/10.1080/10298436.2016.1233003>
- Boz, I., Tavassoti-Kheiry, P., & Solaimanian, M. (2017). The advantages of using impact resonance test in dynamic modulus master curve construction through the abbreviated test protocol. *Materials and Structures*, 50(3), 176. <https://doi.org/10.1617/s11527-017-1045-3>
- Brown, D. L., Allemang, R. J., & Halvorsen, W. G. (1978). Impulse technique for structural frequency response testing. *The Journal of the Acoustical Society of America*, 63(S1), S81–S81. <https://doi.org/10.1121/1.2016847>
- Bustillo Revuelta, M. (2021). *Construction Materials: Geology, Production and Applications*. Springer International Publishing. <https://doi.org/10.1007/978-3-030-65207-4>
- Carret, J., Di Benedetto, H., & Sauzeat, C. (2020). Linear viscoelastic behavior of asphalt mixes from dynamic frequency response functions. *International Journal for Numerical and Analytical Methods in Geomechanics*, 44(7), 1019–1031. <https://doi.org/10.1002/nag.3045>
- Carret, J.-C. (n.d.). *Linear viscoelastic characterization of bituminous mixtures from dynamic tests back analysis*.
- Carret, J.-C., Di Benedetto, H., & Sauzéat, C. (2018a). *Back analysis of impact loadings on viscoelastic specimen* [Communication]. 10th International Conference on Road and Airfield Pavement Technology (ICPT 2017). <https://espace2.etsmtl.ca/id/eprint/23375/>

- Carret, J.-C., Di Benedetto, H., & Sauzéat, C. (2018b). Characterization of Asphalt Mixes Behaviour from Dynamic Tests and Comparison with Conventional Cyclic Tension–Compression Tests. *Applied Sciences*, 8(11), 2117.
<https://doi.org/10.3390/app8112117>
- Carret, J.-C., Di Benedetto, H., & Sauzeat, C. (2018). Multi Modal Dynamic Linear Viscoelastic Back Analysis for Asphalt Mixes. *Journal of Nondestructive Evaluation*, 37(2), 35. <https://doi.org/10.1007/s10921-018-0491-3>
- Carret, J.-C., Pedraza, A., Di Benedetto, H., & Sauzeat, C. (2018). Comparison of the 3-dim linear viscoelastic behavior of asphalt mixes determined with tension-compression and dynamic tests. *Construction and Building Materials*, 174, 529–536.
<https://doi.org/10.1016/j.conbuildmat.2018.04.156>
- De Oliveira, L. S., Lucas Júnior, J. L. O., Babadopulos, L. F. A. L., & Soares, J. B. (2022). Stiffness and fatigue evaluation in cyclic tests with rest periods for asphalt mixtures with or without fly ash. *Construction and Building Materials*, 322, 126426.
<https://doi.org/10.1016/j.conbuildmat.2022.126426>
- DeCarlo, C., Dave, E. V., Sias, J. E., Airey, G., & Mallick, R. (2020). Comparative Evaluation of Moisture Susceptibility Test Methods for Routine Usage in Asphalt Mixture Design. *Journal of Testing and Evaluation*, 48(1), 88–106.
<https://doi.org/10.1520/JTE20180908>
- Di Benedetto, H., de La Roche, C., Baaj, H., Pronk, A., & Lundström, R. (2004). Fatigue of bituminous mixtures. *Materials and Structures*, 37(3), 202–216.
<https://doi.org/10.1007/BF02481620>

- Di Benedetto, H., Mondher, N., Sauzéat, C., & Olard, F. (2007). Three-dimensional Thermo-viscoplastic Behaviour of Bituminous Materials: The DBN Model. *Road Materials and Pavement Design*, 8(2), 285–315. <https://doi.org/10.1080/14680629.2007.9690076>
- Di Benedetto, H., Olard, F., Sauzéat, C., & Delaporte, B. (2004). Linear viscoelastic behaviour of bituminous materials: From binders to mixes. *Road Materials and Pavement Design*, 5(sup1), 163–202. <https://doi.org/10.1080/14680629.2004.9689992>
- Di Benedetto, H., Partl, M. N., Francken, L., & De La Roche Saint André, C. (2001). Stiffness testing for bituminous mixtures. *Materials and Structures*, 34(2), 66–70. <https://doi.org/10.1007/BF02481553>
- Di Benedetto, H., Sauzéat, C., & Sohm, J. (2009). Stiffness of Bituminous Mixtures Using Ultrasonic Wave Propagation. *Road Materials and Pavement Design*, 10(4), 789–814. <https://doi.org/10.1080/14680629.2009.9690227>
- Essid, N., Eddhahak, A., & Neji, J. (2022). Experimental and numerical analysis of the energy efficiency of PCM concrete wallboards under different thermal scenarios. *Journal of Building Engineering*, 45, 103547. <https://doi.org/10.1016/j.jobbe.2021.103547>
- Goel, A., & Das, A. (2008). Nondestructive testing of asphalt pavements for structural condition evaluation: A state of the art. *Nondestructive Testing and Evaluation*, 23(2), 121–140. <https://doi.org/10.1080/10589750701848697>
- Gudmarsson, A., Ryden, N., & Birgisson, B. (2012). Characterizing the low strain complex modulus of asphalt concrete specimens through optimization of frequency response functions. *The Journal of the Acoustical Society of America*, 132(4), 2304–2312. <https://doi.org/10.1121/1.4747016>

- Gudmarsson, A., Ryden, N., Di Benedetto, H., & Sauzéat, C. (2015a). Complex modulus and complex Poisson's ratio from cyclic and dynamic modal testing of asphalt concrete. *Construction and Building Materials*, 88, 20–31.
<https://doi.org/10.1016/j.conbuildmat.2015.04.007>
- Gudmarsson, A., Ryden, N., Di Benedetto, H., & Sauzéat, C. (2015b). Complex modulus and complex Poisson's ratio from cyclic and dynamic modal testing of asphalt concrete. *Construction and Building Materials*, 88, 20–31.
<https://doi.org/10.1016/j.conbuildmat.2015.04.007>
- Gudmarsson, A., Ryden, N., Di Benedetto, H., Sauzéat, C., Tapsoba, N., & Birgisson, B. (2014). Comparing Linear Viscoelastic Properties of Asphalt Concrete Measured by Laboratory Seismic and Tension–Compression Tests. *Journal of Nondestructive Evaluation*, 33(4), 571–582. <https://doi.org/10.1007/s10921-014-0253-9>
- Han, B., Yin, D., & Gao, Y. (2024). The application of a novel variable-order fractional calculus on rheological model for viscoelastic materials. *Mechanics of Advanced Materials and Structures*, 31(28), 9951–9963.
<https://doi.org/10.1080/15376494.2023.2283126>
- Hohensinn, R. (2019). *Detection of Hazardous Ground Movements with Instantaneous Velocity Estimates by GNSS* [Doctoral Thesis, ETH Zurich].
<https://doi.org/10.3929/ethz-b-000348594>
- Imaninasab, R., Loria-Salazar, L., & Carter, A. (2024). Impact of aggregate structure restoration on rutting resistance of asphalt mixtures with very high percentages of RAP.

Road Materials and Pavement Design, 25(sup1), 28–44.

<https://doi.org/10.1080/14680629.2023.2191727>

Jiao, Y., Zhang, Y., Zhang, M., Fu, L., & Zhang, L. (2019). Investigation of fracture modes in pervious asphalt under splitting and compression based on acoustic emission monitoring. *Engineering Fracture Mechanics*, 211, 209–220.

<https://doi.org/10.1016/j.engfracmech.2019.02.025>

Kandhal, P. S., & Mallick, R. B. (2001). Effect of Mix Gradation on Rutting Potential of Dense-Graded Asphalt Mixtures. *Transportation Research Record: Journal of the Transportation Research Board*, 1767(1), 146–151. <https://doi.org/10.3141/1767-18>

Karoliny Lemos Bezerra, A., Carret, J.-C., Feitosa de Albuquerque Lima Babadopulos, L., & Barbosa Soares, J. (2023). Determination of the stiffness of ecological asphalt mixtures with non-destructive impact resonance tests. *Materials Today: Proceedings*.

<https://doi.org/10.1016/j.matpr.2023.07.153>

Khademzadeh, M., & Sarkar, A. (2024). Laboratory vibration testing and analysis of hot mix asphalt mixture under different loading patterns. *Construction and Building Materials*, 417, 135224. <https://doi.org/10.1016/j.conbuildmat.2024.135224>

Kou, X., Pei, C., & Chen, Z. (2021). Fully noncontact inspection of closed surface crack with nonlinear laser ultrasonic testing method. *Ultrasonics*, 114, 106426.

<https://doi.org/10.1016/j.ultras.2021.106426>

Krack, M. (2015). Nonlinear modal analysis of nonconservative systems: Extension of the periodic motion concept. *Computers & Structures*, 154, 59–71.

<https://doi.org/10.1016/j.compstruc.2015.03.008>

- Krishnan, J. M., & Rajagopal, K. R. (2005). On the mechanical behavior of asphalt. *Mechanics of Materials*, 37(11), 1085–1100. <https://doi.org/10.1016/j.mechmat.2004.09.005>
- Lachance-Tremblay, É., Vaillancourt, M., & Perraton, D. (2016). Evaluation of the impact of recycled glass on asphalt mixture performances. *Road Materials and Pavement Design*, 17(3), 600–618. <https://doi.org/10.1080/14680629.2015.1103778>
- Li, P., Su, J., Ma, S., & Dong, H. (2020). Effect of aggregate contact condition on skeleton stability in asphalt mixture. *International Journal of Pavement Engineering*, 21(2), 196–202. <https://doi.org/10.1080/10298436.2018.1450503>
- Lu, D. X., Nguyen, N. H. T., Saleh, M., & Bui, H. H. (2021). Experimental and numerical investigations of non-standardised semi-circular bending test for asphalt concrete mixtures. *International Journal of Pavement Engineering*, 22(8), 960–972. <https://doi.org/10.1080/10298436.2019.1654608>
- Ma, L., Wang, H., & Ma, Y. (2024). Viscoelasticity of Asphalt Mixture Based on the Dynamic Modulus Test. *Journal of Materials in Civil Engineering*, 36(3), 04023624. <https://doi.org/10.1061/JMCEE7.MTENG-17124>
- Martinček, G. (1965). The determination of poisson's ratio and the dynamic modulus of elasticity from the frequencies of natural vibration in thick circular plates. *Journal of Sound and Vibration*, 2(2), 116–127. [https://doi.org/10.1016/0022-460X\(65\)90089-1](https://doi.org/10.1016/0022-460X(65)90089-1)
- Mazurek, G., & Iwański, M. (2017). Modelling of Asphalt Concrete Stiffness in the Linear Viscoelastic Region. *IOP Conference Series: Materials Science and Engineering*, 245, 032029. <https://doi.org/10.1088/1757-899X/245/3/032029>

- Meng, A., Xu, H., Feng, X., & Tan, Y. (2020). Feasibility of freeze-thaw damage analysis for asphalt mixtures through dynamic nondestructive testing. *Construction and Building Materials*, 233, 117220. <https://doi.org/10.1016/j.conbuildmat.2019.117220>
- Mounier, D., Di Benedetto, H., & Sauzéat, C. (2012). Determination of bituminous mixtures linear properties using ultrasonic wave propagation. *Construction and Building Materials*, 36, 638–647. <https://doi.org/10.1016/j.conbuildmat.2012.04.136>
- Nemati, R., & Dave, E. V. (2018). Nominal property based predictive models for asphalt mixture complex modulus (dynamic modulus and phase angle). *Construction and Building Materials*, 158, 308–319. <https://doi.org/10.1016/j.conbuildmat.2017.09.144>
- Nemati, R., Dave, E. V., & Sias, J. E. (2020). Development of Complex Modulus-Based Rutting Index Parameter for Asphalt Mixtures. *Journal of Transportation Engineering, Part B: Pavements*, 146(2), 04020026. <https://doi.org/10.1061/JPEODX.0000171>
- Olard, F., & Di Benedetto, H. (2003). General “2S2P1D” Model and Relation Between the Linear Viscoelastic Behaviours of Bituminous Binders and Mixes. *Road Materials and Pavement Design*, 4(2), 185–224. <https://doi.org/10.1080/14680629.2003.9689946>
- Olard, F., Di Benedetto, H., Eckmann, B., & Triquigneaux, J.-P. (2003). Linear Viscoelastic Properties of Bituminous Binders and Mixtures at Low and Intermediate Temperatures. *Road Materials and Pavement Design*, 4(1), 77–107. <https://doi.org/10.1080/14680629.2003.9689941>
- Orosa, P., Orozco, G., Carret, J. C., Carter, A., Pérez, I., & Pasandín, A. R. (2022). Compactability and mechanical properties of cold recycled mixes prepared with

different nominal maximum sizes of RAP. *Construction and Building Materials*, 339, 127689. <https://doi.org/10.1016/j.conbuildmat.2022.127689>

Phan, C. V., Di Benedetto, H., Sauzéat, C., Lesueur, D., Pouget, S., Olard, F., & Dupriet, S. (2017). Complex modulus and fatigue resistance of bituminous mixtures containing hydrated lime. *Construction and Building Materials*, 139, 24–33. <https://doi.org/10.1016/j.conbuildmat.2017.02.042>

Pouget, S., Sauzéat, C., Di Benedetto, H., & Olard, F. (2010). Numerical simulation of the five-point bending test designed to study bituminous wearing courses on orthotropic steel bridge. *Materials and Structures*, 43(3), 319–330. <https://doi.org/10.1617/s11527-009-9491-1>

Poulikakos, L. D., Pittet, M., Dumont, A.-G., & Partl, M. N. (2015). Comparison of the two point bending and four point bending test methods for aged asphalt concrete field samples. *Materials and Structures*, 48(9), 2901–2913. <https://doi.org/10.1617/s11527-014-0366-8>

Rashetnia, R., Kusam, A., Yadav, S., Pour-Ghaz, M., & Tayebali, A. (2022). Quantifying moisture damage in asphalt concrete using axisymmetric flexural vibration technique. *International Journal of Pavement Engineering*, 23(3), 523–535. <https://doi.org/10.1080/10298436.2020.1757671>

Rezazad Gohari, A., Lamothe, S., Bilodeau, J.-P., Mansourian, A., & Carter, A. (2023). Laboratory Study on Influence of Blending Conditions on Chemo-Thermal Characteristics of Lignin-Modified Bitumen. *Applied Sciences*, 13(13), 7766. <https://doi.org/10.3390/app13137766>

- Sadeghi, P., Karimi, A., Torbatifard, S., & Goli, A. (2024). A comprehensive evaluation of damping, vibration, and dynamic modulus in reclaimed asphalt pavement: The role of rejuvenators, polymer, temperature, and aging. *Case Studies in Construction Materials*, 21, e03366. <https://doi.org/10.1016/j.cscm.2024.e03366>
- Saxena, S., & Patel, M. (2023). Evaluating dynamic behaviour of a concrete dam using modal analysis. *Materials Today: Proceedings*, 93, 296–301. <https://doi.org/10.1016/j.matpr.2023.07.259>
- Tigdemir, M., Kalyoncuoglu, S. F., & Kalyoncuoglu, U. Y. (2004). Application of ultrasonic method in asphalt concrete testing for fatigue life estimation. *NDT & E International*, 37(8), 597–602. <https://doi.org/10.1016/j.ndteint.2004.03.006>
- Tosin, M. C., & Balbinot, A. (2022). Identification and removal of contaminants in sEMG recordings through a methodology based on Fuzzy Inference and Actor-Critic Reinforcement learning. *Expert Systems with Applications*, 206, 117772. <https://doi.org/10.1016/j.eswa.2022.117772>
- Tsangouri, E., Remy, O., Boulpaep, F., Verbruggen, S., Livitsanos, G., & Aggelis, D. G. (2019). Structural health assessment of prefabricated concrete elements using Acoustic Emission: Towards an optimized damage sensing tool. *Construction and Building Materials*, 206, 261–269. <https://doi.org/10.1016/j.conbuildmat.2019.02.035>
- Tweten, D. J., Ballard, Z., & Mann, B. P. (2014). Minimizing error in the logarithmic decrement method through uncertainty propagation. *Journal of Sound and Vibration*, 333(13), 2804–2811. <https://doi.org/10.1016/j.jsv.2014.02.024>

- Wei, H., Li, J., Wang, F., Zheng, J., Tao, Y., & Zhang, Y. (2022). Numerical investigation on fracture evolution of asphalt mixture compared with acoustic emission. *International Journal of Pavement Engineering*, 23(10), 3481–3491.
<https://doi.org/10.1080/10298436.2021.1902524>
- Whitmoyer, S., & Kim, Y. (1994). Determining Asphalt Concrete Properties via the Impact Resonant Method. *Journal of Testing and Evaluation*, 22(2), 139–148.
<https://doi.org/10.1520/JTE12648J>
- Wolf, J., Pirskawetz, S., & Zang, A. (2015). Detection of crack propagation in concrete with embedded ultrasonic sensors. *Engineering Fracture Mechanics*, 146, 161–171.
<https://doi.org/10.1016/j.engfracmech.2015.07.058>
- Yadav, S., Kusam, A., & Tayebali, A. A. (2021). Evaluating Moisture Damage Using Impact Resonance Test. *Journal of Testing and Evaluation*, 49(6), 4118–4134.
<https://doi.org/10.1520/JTE20200372>
- Yassine, R., & Mustapha, S. (2024). The effect of moisture content and temperature on the propagation characteristics of guided waves in timber utility poles-numerical and experimental validation. *Wood Science and Technology*, 58(2), 533–573.
<https://doi.org/10.1007/s00226-023-01528-9>
- Zhang, G. (2014). Simultaneous confidence intervals for several inverse Gaussian populations. *Statistics & Probability Letters*, 92, 125–131. <https://doi.org/10.1016/j.spl.2014.05.013>
- Zhang, L., Li, T., & Tan, Y. (2016). The potential of using impact resonance test method evaluating the anti-freeze-thaw performance of asphalt mixture. *Construction and Building Materials*, 115, 54–61. <https://doi.org/10.1016/j.conbuildmat.2016.04.026>

- Zhang, M., Qian, Z., & Huang, Q. (2019). Test and Evaluation for Effects of Freeze-Thaw Cycles on Fracture Performance of Epoxy Asphalt Concrete Composite Structure. *Journal of Testing and Evaluation*, 47(1), 556–572.
<https://doi.org/10.1520/JTE20170093>
- Zhao, G., Wang, B., Wang, T., Hao, W., & Luo, Y. (2019). Detection and monitoring of delamination in composite laminates using ultrasonic guided wave. *Composite Structures*, 225, 111161. <https://doi.org/10.1016/j.compstruct.2019.111161>
- Zhao, Y., Liu, H., Bai, L., & Tan, Y. (2013). Characterization of Linear Viscoelastic Behavior of Asphalt Concrete Using Complex Modulus Model. *Journal of Materials in Civil Engineering*, 25(10), 1543–1548. [https://doi.org/10.1061/\(ASCE\)MT.1943-5533.0000688](https://doi.org/10.1061/(ASCE)MT.1943-5533.0000688)
- Zhu, Y., Li, F., & Bao, W. (2021). Fatigue crack detection under the vibration condition based on ultrasonic guided waves. *Structural Health Monitoring*, 20(3), 931–941.
<https://doi.org/10.1177/1475921719860772>